Concepts for Rapid-refresh, Global Ocean Surface Wind Measurement Evaluated Using Full-system Parametric Extrema Modeling

Patrick Walton

A thesis submitted to the faculty of
Brigham Young University
in partial fulfillment of the requirements for the degree of

Master of Science

David Long, Chair
Brian Iverson
Phil Lundrigan

Department of Electrical and Computer Engineering

Brigham Young University

August 2021

ABSTRACT

Concepts for Rapid-refresh, Global Ocean Surface Wind Measurement Evaluated Using Full-system Parametric Extrema Modeling

Patrick Walton
Department of Electrical and Computer Engineering, BYU
Master of Science

Satellite wind vector data is integral to atmospheric models and forecasts. Currently, the limited refresh rate of global wind vector measurement systems makes it difficult to observe diurnal variation of mesoscale processes. Using advancements in the underlying subsystem technologies, new satellite wind scatterometers may be possible that increase temporal resolution, among other performance metrics. I propose a method for parametrically modeling the extreme performance range of a complex system. I use this method to develop a model of the space of possible satellite wind scatterometer designs. I validate the model using point designs of heritage scatterometers. Finally, I present two example concepts for constellations of cooperative satellite wind scatterometers capable of measuring global ocean surface vector winds every hour for the same total cost as a single heritage scatterometer.

Keywords: scatterometer, satellite constellations, CubeSat, ocean vector winds, remote sensing, parametric modeling, remote sensing

ACKNOWLEDGMENTS

This work was made possible through the financial support of the National Aeronautics and Space Administration (NASA) through the Future Investigators for Earth and Space Science Technology, grant number 80NSSC19K1369. Further support came through a collaborative agreement with NASA Marshall Space Flight Center (MSFC), contract number 80MSFC19M0047.

I am especially indebted to Dr. David G. Long, Principal Researcher of the BYU Center for Remote Sensing, who has been a great mentor and friend for many years. He adeptly toed the line between sharing wisdom on what's feasible while staying open to my wild ideas. He nurtured me into a better professional than I could have become without him.

I am grateful to the faculty and other students in the BYU satellite program and especially those who participated in the Passive Inspection CubeSats project. In particular, faculty advisors Dr. Brian Iverson and Dr. Wilde continued to mentor me as I adapted lessons from PICs to this work. I was uplifted by kind mentors in the ocean vector winds science community, including my collaborators at MSFC, Dr. Timothy Lang and Raymond Cutts, who believed in me and gave me confidence to develop professionally.

In the course of this work, I have made an effort to prepare it for commercialization. This has been a significant undertaking, which would be unimaginable without the support of Alex Laraway. He has been a better collaborator, team-mate, and friend than I could have asked for.

My family has always empowered and encouraged me to dream big and do good for others. I wouldn't have come this far without them. I thank my parents and grandparents, who nurtured a love of truth and creativity that was contagious. They inspired me to do what I find important, whether it is conventional or not. I thank my siblings, whose friendship and shared excitement keeps me going. I thank my son, David, who brings joy to the most

difficult days and gives me a reason to be my best self. Most of all, I am so grateful for my wife, Marquie. She has sacrificed for nearly ten years to support me in pursuing a career of conviction. I am amazed at her selflessness, which has given me wings to fly.

TABLE OF CONTENTS

LIST OF TABLES

LIST OF FIGURES

Chapter 1

Introduction

Satellite scatterometers produce microwave Earth-observation data well-suited for measurement of numerous geophysical properties [1]. Scatterometers are capable of measuring wind speed and direction (wind vectors) near the ocean surface, ice coverage, vegetation coverage, soil moisture, and average wind vectors over sand and snow [2]–[6].

Improvements in near-surface ocean vector wind measurements enable scientists to better observe and model weather and climate processes. These improved models enable more reliable forecasting, which provides value to various sectors dependent on accurate weather and climate information, including industry, agriculture, water management, transportation, and tourism [7].

Satellite scatterometer observations of near-surface ocean vector winds have many advantages over in-situ measurement systems, such as instrumented ships and buoys, thanks to their ability to produce global mappings. However, the current constellation of scatterometers is limited to spatial resolutions of tens of kilometers, revisit time of tens of hours, wind speed accuracies of multiple meters per second, and wind direction accuracies of tens of degrees. In Chapter 2, I discuss the fundamentals of scatterometry and improvements that led to the primary scatterometer architectures used in today's constellations.

Current scatterometer temporal resolutions are particularly limiting. In oceanography and atmospheric science planetary boundary layer processes occurring on timescales shorter than several days cannot be observed and modeled due to signal aliasing [8]. This blindness on short timescales limits the accuracy of models used for weather forecasting.

The lack of frequent data for initial conditions in numerical weather predictions also limits weather forecast accuracy. Numerical weather models that couple the ocean and atmosphere are more sensitive to satellite scatterometer measurements than any other type of satellite measurement, but unfortunately, scatterometer data is among the least plentiful [9]. This suggests that increasing scatterometer data is one of the greatest areas for potential improvement of weather forecast accuracy.

Limited-accuracy weather forecasts are responsible for loss of property, loss of human life, and sustained poverty. In the United States, hurricane warnings, the most certain cyclone advisory issued by the National Weather Service, are only issued 36 hours before landfall [10]. Early forecasts are uncertain, so a given region may fall in the cone of possible landfall many times each hurricane season. Only the affluent can afford to prepare and evacuate before the advisory is either upgraded to a hurricane warning or deemed a false alarm. Those of poor socioeconomic status, without the means to take off time to secure property and evacuate, are hit the hardest [11]. As a result, shortfalls in hurricane warnings, and other extreme weather advisories, result in millions more people entering poverty [12] and extreme weather continues to take thousands of lives per year [13]. Due to climate change, extreme weather is becoming increasingly intense and erratic [14], leading to a rapidly increasing annual cost of extreme weather [15].

1.1 Thesis Statement

Scatterometers can be miniaturized for use in a constellation capable of affordably measuring ocean vector winds with global, hourly refresh. Hourly ocean vector wind measurement enables advanced observation, modeling, and forecasting of the weather which can save property and lives. This thesis develops a new parametric extrema modeling technique for scatterometer system design to explore potential new architectures that can exploit technology advancements to inexpensively meet the need for hourly ocean wind measurements. In this thesis I present a taxonomy of scatterometer architectures, derive the model, compare the model results with previous scatterometer missions, and present two architectures for low-cost scatterometer systems capable of measuring global, hourly ocean vector winds.

1.2 Summary of Results

The primary result of this work is the full-system parametric extrema model of satellite wind scatterometers given in Chapter 5. A check of the validity of this model was performed using the actual design and performance parameters of existing scatterometers, as described in Chapter 6. As a secondary result, Chapter 7 provides designs for satellite wind scatterometers that are enabled by advances in scatterometer subsystem technologies. Finally, this work resulted in the taxonomy for modes of cooperation between scatterometer frontends and between scatterometers, described in Chapter 4, and a novel methodology for parametrically modeling complex systems, given in Chapter 3.

Chapter 2

Background

Scatterometry is an important application of radar remote sensing, most prominently applied in satellite wind vector measurement. Experimentation and development between 1970 and 2000 has established two primary design architectures for satellite scatterometry: fan beam and scanning-pencil beam [1]. More recently, a hybrid design, the rotating fan beam scatterometer, has been developed [16].

2.1 Ocean Surface Vector Wind Scatterometry

Scatterometers are active microwave radars used to measure surface properties by measuring the fraction of the surface-scattered signal returned to the radar receiver, known as the radar cross-section, σ. The normalized radar cross-section, σ_0, is the key characteristic of the response of a surface to radar reflections. It is defined as

$$\sigma_0 = \sigma / A_c \ , \tag{2.1}$$

where A_c is the area of the resolution cell [1].

The normalized radar cross-section obtained when observing the ocean surface can be used to determine the near-surface wind speed and direction over the ocean. Friction caused by air flow over the ocean surface produces turbulence. This turbulence results in capillary waves, or Bragg waves, across a wide spectrum of wavelengths. As these waves

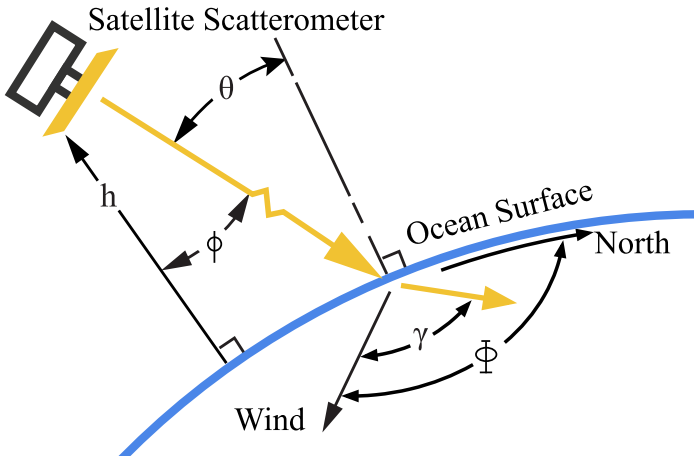

Figure 2.1: Wind vector measurement geometry. Incidence angle, θ, is measured from the surface normal to the look direction. azimuth angle, γ, is measured from the surface projection of the look direction to the wind direction. Φ is the wind direction measured from North, and U is the wind speed. Orbital altitude, h, is measured from the nadir point to the spacecraft, and look elevation angle, ϕ, is measured from the altitude line to the look direction.

dissipate energy through viscosity, they come into equilibrium with the wind. As a result, the process by which they scatter electromagnetic signals, called Bragg scattering, can be used to find the wind over the surface. This scattering increases with higher wind speeds and varies sinusoidally with the angle between the look direction and the wind direction (see Fig. 2.1) [1], [3].

The relationship between σ_0 and wind vector is described by the geophysical model function (GMF), expressed as $\sigma_0 = f(|U|, \chi, \theta, \lambda, pol, \ldots)$, where $|U|$ is the wind speed, θ is the observation incidence angle (Fig. 2.1), λ is the radar wavelength, pol is the radar polarization, and "..." represents neglected variables. The azimuth angle between the look direction and the wind direction is $\chi = \gamma - \Phi$, where γ is the azimuth angle (Fig. 2.1) and Φ is the wind direction, both measured clockwise from North. Typically, the GMF is empirically developed, and tabulated for use in the wind retrieval process [17], [18].

Wind cannot be determined from a single σ_0 measurement due to the sinusoidal variance of σ_0 with χ (see Fig. 2.2). Multiple, information-diverse measurements, called flavors, are required. Typically, information diversity is achieved by taking measurements from multiple viewpoints with varying azimuth angle, χ, but can also be achieved using

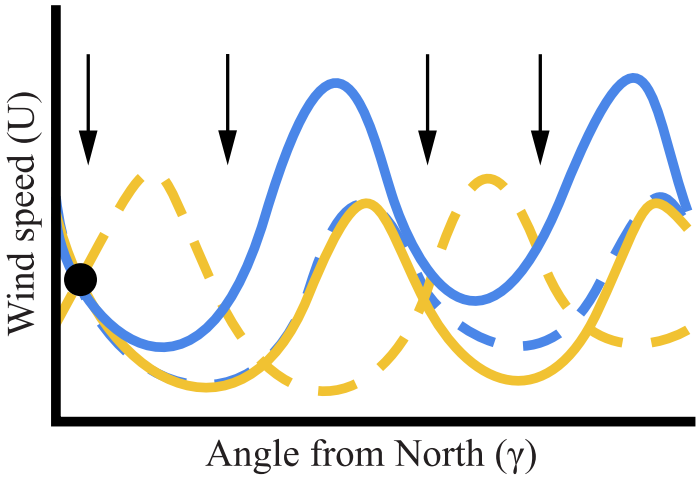

Figure 2.2: Possible wind vector solutions for a single, noise-free σ_0 measurement, obtained at the following azimuth angles and polarizations using the NSCAT-1 GMF. Blue/Solid: 0°, v-pol. Blue/Dashed: 25°, v-pol. Yellow/Solid: 25°, h-pol. Yellow/Dashed: 90°, v-pol. Black arrows mark the four solutions for the pair of 45° and 90° σ_0 measurements. The black dot at left indicates the true wind speed and direction, found using all four measurements. Reproduced from Naderi et al. [2].

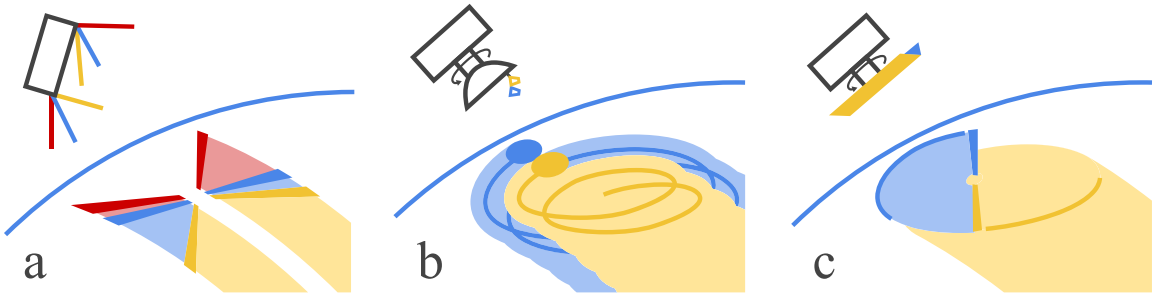

Figure 2.3: Illustration of the defining characteristics to the conventional architectures for satellite wind scatterometry including the antennas, scanning pattern, footprint, and ground swath of each. a) Fan-beam scatterometers (e.g., NSCAT) scan like angled push-brooms on the ground requiring long, rectangular antennas. b) Scanning pencil-beam scatterometers (e.g., SeaWinds) cover concentric helices on the ground using rotating, dish antennas. c) Rotating fan-beam scatterometers (e.g., RFSCAT) scan like a lawnmower on the ground, covering concentric helices with long, rotating, rectangular antennas.

varying incidence angles, polarizations, and/or frequencies. With two, collocated, near-simultaneous, azimuth-diverse measurements, the GMF has four solutions, indicated by the black arrows in Fig. 2.2. In practice, additional steps may be required to select a single direction due to noise and the near-symmetry of the GMF with respect to direction.

2.2 Current Scatterometer Architectures

The first satellite scatterometer, RADSCAT on Skylab, successfully detected variance in the physical structure of the ocean surface by measuring the scattered signal [19]. But RADSCAT was unable to resolve individual wind vector measurements with its single dish antenna, because it obtained only one flavor. RADSCAT's successor, the SASS instrument on the SeaSat satellite, measured wind vectors with a fan-beam architecture, which uses long-thin antennas to scan the surface in a push-broom-like pattern. RADSCAT only had two antennas for each side, so it only acquired two flavors for each wind vector cell. This required complicated post-processing to reduce ambiguity in wind retrieval [20].

Follow-on fan-beam scatterometers, including Europe's ESCAT scatterometer on the ERS-1 and ERS-2 satellites [21] and NASA's NSCAT scatterometer on the ADEOS-1 satellite [2], demonstrated unambiguous wind vector measurement using three fan-beam antennas per swath (Fig. 2.3a). They used on-board digital processing to subdivide the swath, and collocation of σ_0 measurements to form wind vector cells on the ground [2], [22].

Two additional architectures have since been demonstrated. In 1999, NASA launched the SeaWinds instrument on the QuikSCAT satellite to demonstrate the scanning pencil beam architecture, which measures wind vectors by circularly scanning two offset pencil beams [23] (Fig. 2.3b). In 2018, China and France launched the RFSCAT instrument on the CFOSAT satellite to demonstrate the rotating fan beam concept (Fig. 2.3c), which scans long, thin antennas circularly to produce a lawnmower-like pattern on the ground [16].

Subsequent scatterometers, flown by Europe (ASCAT), India (OSCAT), and China (HY-2a), have been patterned after and improved on these established approaches. For example, the ASCAT instruments, aboard Europe's MetOp satellites, improve on the ESCAT instruments with continuous operation, a doubled swath, greater sensitivity, and finer wind vector resolution [24]. A summary of current, past, and planned scatterometers is given in [3].

The defining characteristics of each architecture include the antenna beam shape and corresponding ground swath pattern. These characteristics are illustrated for each architecture in Fig. 2.3. Each approach has tradeoffs, especially in the antenna, wind retrieval, and

swath. Fan-beam antennas are difficult to stow, deploy, and calibrate, but they are more reliable after deployment since they have no moving parts. Scanning pencil-beam dish antennas are compact and stable, but they require rotary bearings, which are liable to fatigue and require momentum compensation. Scanning pencil beam scatterometers typically have greater signal-to-noise ratio than fan beam scatterometers, but have shorter dwell time due to scanning. Rotating fan beams generally combine the benefits and challenges of both.

While fan-beams illuminate the surface at a large range of incidence angles, scanning pencil beams observe at a couple of incidence angles only. A complete GMF must be developed for each incidence angle, so scanning pencil beams require less effort in model development. Scanning pencil-beam and rotating fan beam scatterometers provide valuable measurements in the nadir region, where fan-beam scatterometers have a gap with incidence angle less than the minimum allowable 18°. The rotating fan beam may provide greater wind direction accuracy, since it acquires more near-simultaneous, azimuth-diverse measurements [16].

Scatterometers typically measure the backscatter, the signal scattered back in the direction of the transmitter. Reflectometers measure the signal scattered in a direction away from the transmitter. Reflectometers require a transmitter and a separate receiver at a different location. The most common type of reflectometer is the global navigation satellite system (GNSS) reflectometer, or GNSS-R, which measures GNSS signals that have been scattered by the ocean surface. GNSS-reflectometers exploit the power and ubiquity of GNSS signals. As a result, they require much less power than scatterometers. However, reflectometers have historically been limited to narrow swath widths. Current reflectometers include NASA's CYGNSS train [25] and Spire Global's CubeSat constellation [26].

2.3 An Overview of Traditional System Design Methodologies

In recent decades, technologies used by satellite wind scatterometers have advanced much more rapidly than the scatterometers themselves, due in part to the complexity of satellite

Figure 2.4: Illustration of the flow of a typical system design process [27]. Design flows in sequence from stages on the left to stages on the right. Iteration typically occurs if a next-generation product is approved after production of the first, as illustrated by the yellow, negative-feedback arrow.

scatterometer systems. These advances can enable improved scatterometer designs that diverge from traditional classes of designs.

Typically, a system designer creates system requirements, generates system concepts, models them, selects the most promising concept, designs and models the subsystems, refines the system, and produces it [27]. This process flow is illustrated in Fig. 2.4.

Ideally the designer takes information gained at each step and goes back to prior steps to iterate, making design decisions with better foresight. Divergent concepts require this frequent iteration, because they often involve unforeseen factors. In practice, schedule and budget constraints often prevent this, because simulations are time-intensive to develop and run. As a result, iteration primarily takes place only if development of a next-generation system is approved after the first is completed. This is the "innovator's dilemma" [28]. The risks of developing divergent designs incentivize designers to largely repeat designs that worked in the past, potentially missing many optima in the design space that enable better scatterometer architecture designs.

Satellite scatterometry has a rich history of innovation that has enabled it to provide extensive value to Earth science, situational awareness at sea, and weather forecasting. However, better temporal and spatial resolution and better accuracy are required for many applications and prevented by the cost of scatterometers. Many recent improvements in small satellite rideshare, miniaturized electronics, deployable mechanisms, and materials have yet to be incorporated into scatterometry. Incorporating these advances using modern approaches to rapid, iterative technology development may yield powerful improvements to scatterometer performance, unlocking new capabilities in the fields dependent on scatterometer data. This is the goal of my thesis.

Chapter 3

Full-system Parametric Extrema Modeling

For complex hardware systems, engineers often innovate too slowly. To innovate faster, they need to iterate faster, but traditional build and test cycles are slow. To overcome this, they simulate, but they still have to manually transfer results from one lengthy, partial simulation to another. My parametric, full-system extrema modeling method, helps engineers quickly and easily make rough, early passes through the entire design cycle. This makes it possible to rapidly evaluate many more concepts, potentially finding much more promising ones early enough to implement them.

Parametric, full-system extrema modeling consists of design parameters, performance metrics, and relationships for calculating design performance (see Fig. 3.1). The relationships are exclusively closed-form, which allows the designer to automatically recalculate system-wide performance. This rapid approach enables engineers to iteratively explore the design space before selecting a single concept for refinement, as illustrated in Fig. 3.2. Parametric, full-system extrema modeling underlies the model of satellite scatterometry described in Chapter 5, which in turn, is used to evaluate the scatterometer concepts of Chapter 7.

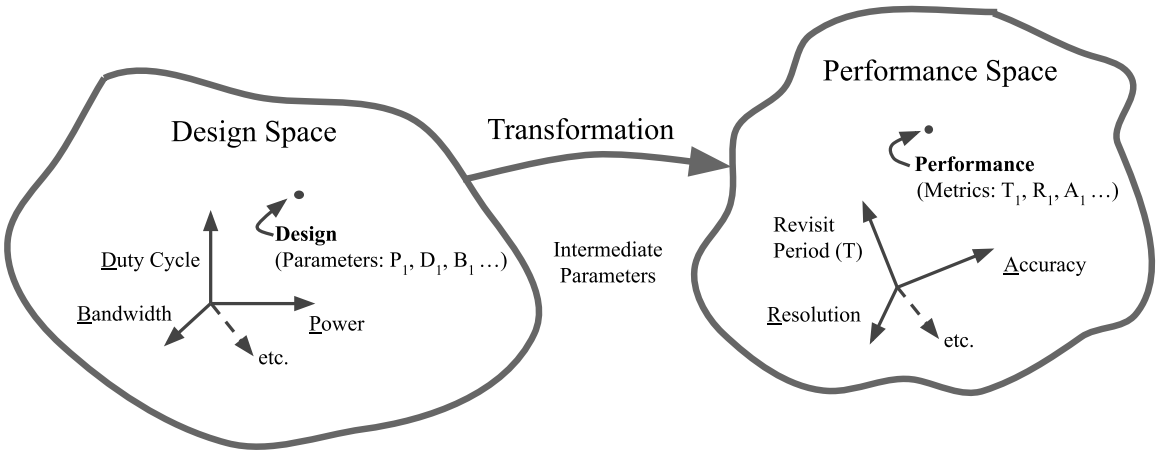

Figure 3.1: Conceptual illustration of the design and performance spaces that constitute the parametric methodology used in this work. Each space is spanned by a basis, a set of design parameters or performance metrics that independently defines the space. A design is located in the design space with a set of design values. These values can be "transformed" into a design performance, located in the performance space with a set of performance values.

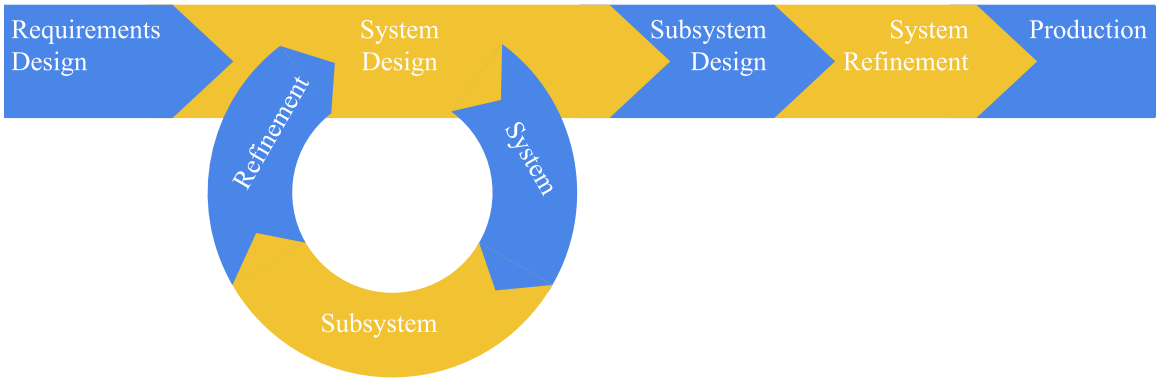

Figure 3.2: Conceptual fit of full-system parametric extrema modeling in the typical design flow described in Chapter 2. Compare to Fig 2.4. Full-system parametric extrema modeling enables the designer to iterate on the entire system early in the development process.

3.1 Organization of the Full-system Parametric Model

The performance space is spanned by a performance "basis", or set of performance metrics which fully characterize system performance. The choice of basis is up to the designer, since design bases are not unique. The performance metrics can be minimized by tracing requirements to the highest point in the hierarchy of need which can feasibly be modeled.

For example, "power generated" and "power consumed" are sometimes used as satellite performance metrics, but in Chapter 5, these are replaced with "net power supply", which expresses the higher need that the power budget close with margin.

The transformation is a set of equations that express the performance metrics as functions of the design metrics. This makes it feasible to broadly evaluate the design space and identify promising classes of designs as candidates for more detailed analysis. In this initial evaluation, closed form relations are preferable to simulations, even if approximate. For example, in scatterometry, normalized radar cross-section, σ_0, is a nonlinear function of several variables as described in Chapter 2. In the model of Chapter 5, the nonlinear σ_0 function is expressed as a polynomial fit of θ.

The design space is spanned by a design basis, or set of design parameters over which the designer has direct control. For example, in Chapter 5, the look angle of the satellite is used as a design parameter instead of the incidence angle of the signal on the ground, because look angle is more directly in the control of the designer.

The number of design parameters can be minimized by expressing interdependent parameters as functions of independent parameters. For example, pulse length, radar duty cycle, and pulse repetition interval are often used as radar design parameters, but they are not independent. In Chapter 5, pulse repetition interval is expressed as a function of design parameters pulse length and radar duty cycle. This reduces the total number of design parameters and ensures they are not dependent upon each other.

The transformation equations can express performance metrics purely as functions of design parameters, but this can be unwieldy. It helps to group some design parameters into intermediate parameters. This provides extra intuition into the system and simplifies the performance functions. For example, in Chapter 5, the performance metric "net power supply" is expressed as a function of the max powers and duty cycles of the different elements of the satellite system, similar to the power budgeting common in spacecraft systems engineering.

3.2 Implementation of the Extrema Model

The parametric, full-system extrema modeling approach is quick and approximate. It begins with a minimum and maximum (the extrema) for each design parameter and calculates a minimum and maximum for each intermediate parameter and performance parameter. For clarity, Chapter 5 only makes minimum and maximum parameters explicit where the minimum and maximum functions differ from the general case.

In implementation, maximum values are used for parameters that increase a function and minimum values for parameters that decrease a function. For example, if the function is

$$f = \frac{a \sin b}{c} + d \cos e \ , \tag{3.1}$$

then minimum values (denoted with the "-" superscript) are paired with maximum values (denoted with the "+" superscript) as follows

$$\begin{aligned} f^- &= \frac{a^- \sin b^-}{c^+} + d^- \cos e^+ \ , \\ f^+ &= \frac{a^+ \sin b^+}{c^-} + d^+ \cos e^- \ . \end{aligned} \tag{3.2}$$

If a given parameter both increases and decreases a function, like extrema should be paired. For example, in Chapter 5, the angular diameter of Earth from the perspective of the satellite is given as

$$\rho = 2 \sin^{-1} \left(\frac{R_E}{R_E + h} \right) \ , \tag{3.3}$$

where R_E is the radius of the Earth and h is the orbital altitude. The extrema implementation of ρ is

$$\begin{aligned} \rho^- &= 2 \sin^{-1} \left(\frac{R_E^-}{R_E^- + h^+} \right) \ , \\ \rho^+ &= 2 \sin^{-1} \left(\frac{R_E^+}{R_E^+ + h^-} \right) \ , \end{aligned} \tag{3.4}$$

where the range of R_E^- to R_E^+ results from the oblateness of the Earth and h^- and h^+ are equal for a circular orbit and different for an elliptical orbit.

Similarly, if a particular min/max pairing never occurs, like extrema should be paired. For example, in Chapter 5, slant range is given as

$$R_s = \sin\alpha \frac{R_E}{\sin\phi} \ , \tag{3.5}$$

where $\alpha = f(\phi)$ is the look Earth angle and ϕ is the look angle of the radar. α is dependent on ϕ, so α^- never corresponds with ϕ^+ and vice versa, so the extrema implementation of slant range is

$$\begin{aligned} R_s^- &= \sin\alpha^- \frac{R_E^-}{\sin\phi^-} \ , \\ R_s^+ &= \sin\alpha^+ \frac{R_E^+}{\sin\phi^+} \ . \end{aligned} \tag{3.6}$$

3.3 Summary

The full-system extrema modeling approach leads to bounds on the possible outcomes. By comparing bounds of performance for various concepts, it provides a fast method for evaluating new concepts and later downselecting to the most promising concepts that merit further analysis. To evaluate concepts using this method, I created a design dashboard in a spreadsheet that enables me to modify any parameter and immediately see the impact to the rest of the system.

The parametric, full-system, extrema modeling approach can be used to iterate through more concepts than there would normally be time to explore, increasing the possibility of finding new solutions. In Chapter 5, a full-system parametric extrema model is given for the satellite wind scatterometer system, and designs identified using this model are given in Chapter 7.

Chapter 4

Scatterometer Directionality and Cooperation

As described in Chapter 2, scatterometers have historically been launched as individual non-cooperative missions. Over time cooperative uses of their data have emerged. In recent years, small satellites have matured and taken an important role in satellite innovation. The low cost of small satellites enables new measurement architectures with multiple free-flying satellites that cooperate one with another [25], [29], [30].

The parametric model of Chapter 5 is intended to model the full scatterometer system and account for the entire space of solutions to scatterometer wind measurement, including solutions using cooperative scatterometer systems. Modeling this solution space parametrically requires an extended taxonomy of modes of scatterometer operation and cooperation. This chapter expands existing terminology of relevant scatterometer subsystems to develop that taxonomy.

4.1 Extant Terminology

The taxonomies of Section 4.2-4.3 build on the extant terminologies of multiple radar antennas, communication modes, and satellites. This section reviews these extant terminologies.

Radar Antennas

Radars transmit a signal and receive the return of the signal from a physical surface. Cooperative radar antenna terminology describes how one or more antennas divide up the tasks of signal transmission and reception. The basic antenna configurations of radar systems are monostatic and bistatic (see Section 1.5 of [31]). The IEEE gives the following definitions for radar configuration terms [32]:

- "**monostatic radar**: a radar system that transmits and receives through either a common antenna or through collocated antennas."
- "**bi-static radar**: a radar using antennas for transmission and reception at sufficiently different locations that the angles or ranges to the target are significantly different."
- "**multistatic radar**: a radar system having two or more transmitting or receiving antennas with all antennas separated by large distances when compared to the antenna sizes."

While IEEE classifies collocated antennas as monostatic radars, the term "pseudo-monostatic" is commonly used as well. Note also that bistatic radars are a subset of multistatic radars.

Communication Modes

Communications systems transfer information between terminals of a link. Communication modes terminology describes how the terminals of a communication link participate as either senders, receivers, or both. The Alliance for Telecommunications Industry Solutions gives the following definitions for several modes of operation of a communications link [33]:

- "**simplex operation**: operation in which transmission occurs in one and only one preassigned direction."
- "**half-duplex operation**: operation in which communication between two terminals occurs in either direction, but in only one direction at a time."

Table 4.1: An excerpt of the morphological taxonomy of distributed satellite systems given by Selva et al. [29]. For each factor a binary low or high rating is given to the type of distributed satellite system.

Group Type	**Homogeneity**	**Size**	**Spatial Separation**	**Functional interdependence**	**Operational independence**
Constellation	H	H	H	L	L
Chain	H	L	L	L	H
Train	L	L	L	L	H
Cluster	H	L	L	H	L
Faction	L	L	L	H	L
Network	H	H	H	H	L

- "**full-duplex operation**: operating method in which transmission is possible simultaneously, in both directions of a telecommunication channel."

Distributed Satellites

Selva et al. [29] give a taxonomy of distributed satellite systems including constellations, clusters, and swarms, among others. They classify these groups of satellites in terms of five morphological factors: homogeneity, size, spatial separation, functional interdependence, and operational independence (see Table [29] for definitions). An excerpt of their taxonomy is given in Table 4.1 with the following additions and modifications:

- Table 3 in Selva et al. [29] cites the Iridium satellite constellation as an example of a constellation, but the Iridium constellation is a communications network with high

functional interdependence. Table 4.1 applies the term "network" for a constellation with high functional interdependence.

- A term for moderate groups of homogeneous, independent satellites with low spatial separation, such as CYGNSS [25], is missing from Table 3 of Selva et al. [29]. The table includes "trains", citing NASA's A-train, but trains have low homogeneity. A term for train with high homogeneity is needed for a group like CYGNSS. Table 4.1 suggests the term flee"chains" for this type of configuration.
- Selva et al. [29] use the term fractionated for a small, distributed satellite system of different satellites that are close together, functionally interdependent, and operated primarily by the same organization. Table 4.1 substitutes the term "faction" to match the part of speech of the other terms.

4.2 Directionality

Historical scatterometers were not designed with multi-satellite cooperation in mind. As a result, they only measured backscatter, the signal returned back in the direction of the scatterometer transmitter. Signal scattered in other directions can also be used to measure the scattering properties of the surface. This section gives a taxonomy of potential scatterometer measurement architectures classed by the direction from which they measure signal scattered off the surface. An illustration of this taxonomy is given in Fig. 4.1.

Historical scatterometers can be more specifically termed "back-scatterometers" because they measure the backscatter of the transmitted signal. Back-scatterometers are by definition monostatic (or pseudo-monostatic) radars.

Cooperative scatterometers that measure the signal scattered in directions other than the backward direction are sometimes referred to as "bistatic scatterometers", but for the purpose of this directional taxonomy they can be termed cross-scatterometers. Cross-scatterometers can be further divided into side-scatterometers or forward-scatterometers. Cross-scatterometers are multistatic radars.

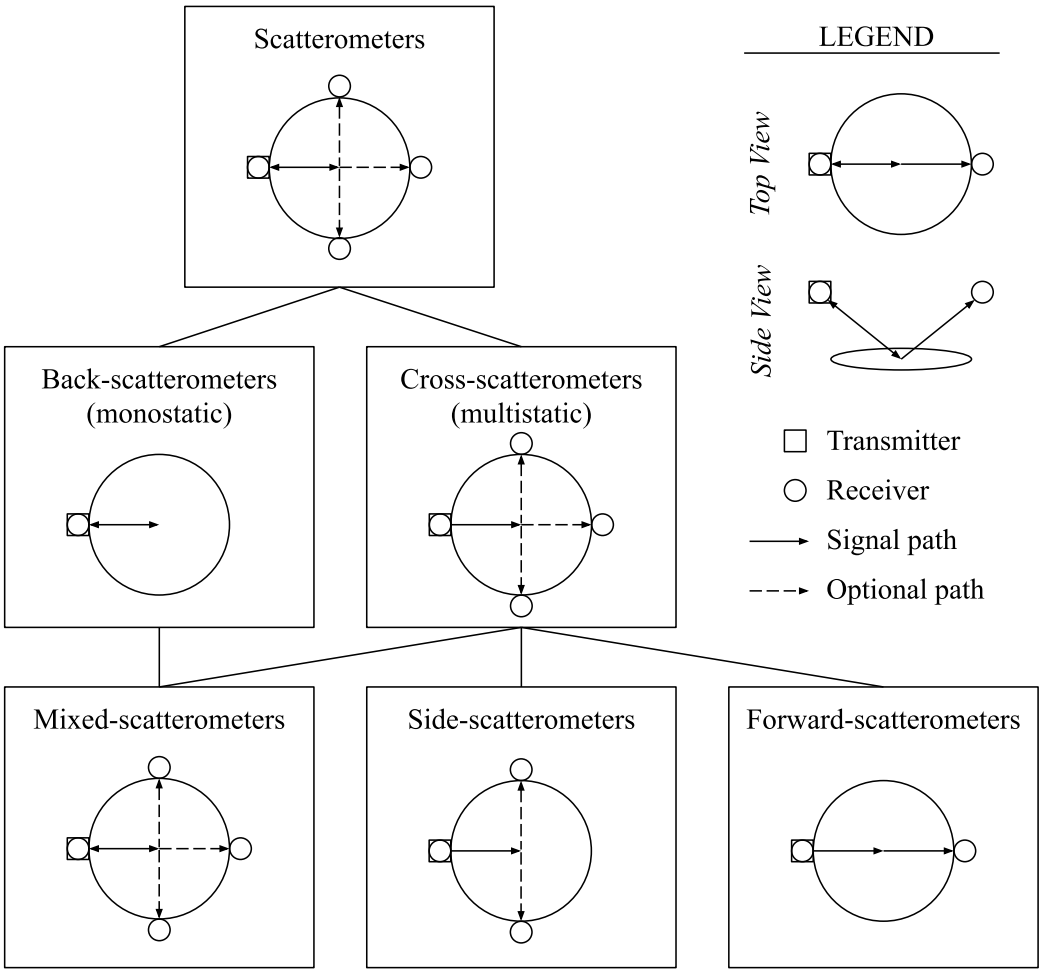

Figure 4.1: Graphical taxonomy of directional configurations of scatterometer measurement. A directionality motif is included for each scatterometer configuration. A legend for the motifs is given at right.

Cooperative scatterometer systems that measure both backscatter and cross-scatter can be termed mixed-scatterometers. Mixed-scatterometers are systems of satellite radars that include monostatic and multistatic radars, as well as radars that operate both monostatically and multistatically. Mixed-scatterometer systems can consist of satellites that each act as back-scatterometers, cross-scatterometers, or both.

4.3 Cooperation

Scatterometer cooperation occurs between multiple scatterometer satellites and between multiple scatterometer front-ends (defined as the transmit/receive electronics and the antenna)

contained on the same satellite. Fig. 4.2 illustrates the taxonomy of multiple front-end and multiple satellite cooperation used in the model of Chapter 5. The majority of cases in Fig. 4.2 (a-d,e,g,i) depict back-scatterometers. Cases f and h of Fig. 4.2 depict cross-scatterometers and Fig. 4.2j depicts a mixed-scatterometer. In the figure, δt indicates a minimal time-delay between periods of near-simultaneous sampling. Δt indicates a longer time-delay between subsequent passes of the same or different satellites.

The cooperative modes of multiple satellites and front-ends described in the following sections are applied to the model of Chapter 5 multiplicatively. For example, NSCAT had six antennas, which used two different types of cooperation. Three antennas cooperated to obtain multiple flavors ($M_{fs} = 3$) in each of two groups that cooperated to expand the swath ($M_{fc} = 2$). The total front-end quantity is modeled as the product of the two multiples, $M_{fc} M_{fs} = 6$.

Independent Scatterometer Satellites and Front-ends

Scatterometer satellites and front-ends receiving the return of their own signal can be said to obtain their scatter measurements independently (Figs. 4.2a-d). Recall that scatterometers require multiple scatter measurements of varying flavors (information diversity via varying geometry, frequency, incidence angle, polarization, etc.) to fully solve for wind vector, as described in Chapter 2. Independent scatterometers that obtain insufficient flavors can co-operate to obtain supplementary measurements with varying flavors (Fig. 4.2c-d). Multiple supplementary front-ends (M_{fs}) can view the same spot on the ground one after another to obtain multiple flavors (Fig. 4.2c). For example, NSCAT and ASCAT both have supplementary front-end multiples of $M_{fs} = 3$ as each side of the swath has 3 different antennas that subsequently view the same spot on the ground from different azimuth angles.

Multiple supplementary satellites (M_{ss}) can cooperate in a cluster, viewing the same location on the ground subsequently with different azimuth angles (Fig. 4.2). For example, each of NSCAT's antennas take turns collecting samples. Supplementary satellites could theoretically focus and obtain a continuous stream of measurements for their dedicated flavor.

If independent scatterometers already obtain enough flavors, they can cooperate in complementary ways (Figs. 4.2a-b). Multiple complementary front-ends (M_{fc}) can cooperate to broaden the swath (Fig. 4.2a). For example, NSCAT and ASCAT have a complementary front-end multiple of $M_{fc} = 2$ as they have groups of antennas observing each side of the subsatellite track.

Multiple complementary satellites (M_{sc}) can cooperate to increase the temporal resolution (Fig. 4.2b). If the satellites are arrayed as a chain in a single orbit, they increase the temporal resolution as the chain passes. The CYGNSS system has a complementary satellite multiple of $M_{sc} = 8$ as its eight small satellite GNSS-reflectometers fly in a chain to measure the temporal variability of tropical cyclones [25].

Satellites arrayed as a constellation in a variety of orbital planes increase the mean revisit rate. For example, the three ASCATs currently operating (2021) form a constellation with a revisit period of about 16 hours. Constellations are modeled in Chapter 5 by the number of orbital planes they occupy (N_{op}). They are not included in Fig. 4.2.

Interdependent Scatterometers

Scatterometer satellites and front-ends receiving a signal that they did not transmit can be said to obtain their scatter measurements interdependently (Fig. 4.2e-j). Interdependent scatterometer satellites (cases f, h, and j of Fig. 4.2) operate in clusters. The language of communication links can be applied to interdependent scatterometer systems, where the various satellites and/or front-ends are the nodes.

When one satellite/front-end only transmits and the other only receives (Figs. 4.2e-f), they form a simplex scatterometer system (M_{sx}, M_{fx}). Simplex scatterometer satellites (Fig. 4.2f) are cross-scatterometers. GNSS-reflectometer systems are examples of simplex scatterometer satellites where a GNSS satellite is the transmitter satellite and the reflectometer is the receiver.

Satellites/front-ends that can each transmit and receive in turn, but not simultaneously (Figs. 4.2g-h) form half-duplex scatterometers (M_{sh}, M_{fh}). Half-duplex scatterometer satellites (Fig. 4.2h) are also cross-scatterometers.

Full-duplex scatterometer satellites/front-ends (M_{sf}, M_{ff}) transmit and receive simultaneously (Figs. 4.2i-j). Polarimetric scatterometers are examples of full-duplex front-ends with multiple dual-polarization antennas [1], allowing them to obtain multiple flavors simultaneously. Other full-duplex front-ends or satellites could use different frequencies or look geometries, respectively. Full-duplex scatterometer satellites are mixed-scatterometers. They have the potential to operate synergistically, continuously obtaining at least three flavors (at least two backscatter and a cross-scatter measurement) with two cooperative small satellites.

4.4 Conclusion

Definition of these modes of multi-satellite and multi-front-end cooperation facilitates parameterization of the scatterometer design space. The methodology developed for parametric modeling is given in Chapter 3. The parametric model of the scatterometer design space is derived in Chapter 5. The contribution to scatterometer performance of multiple satellites and front-ends applied in these varied modes of operation is described in Section 5.11.

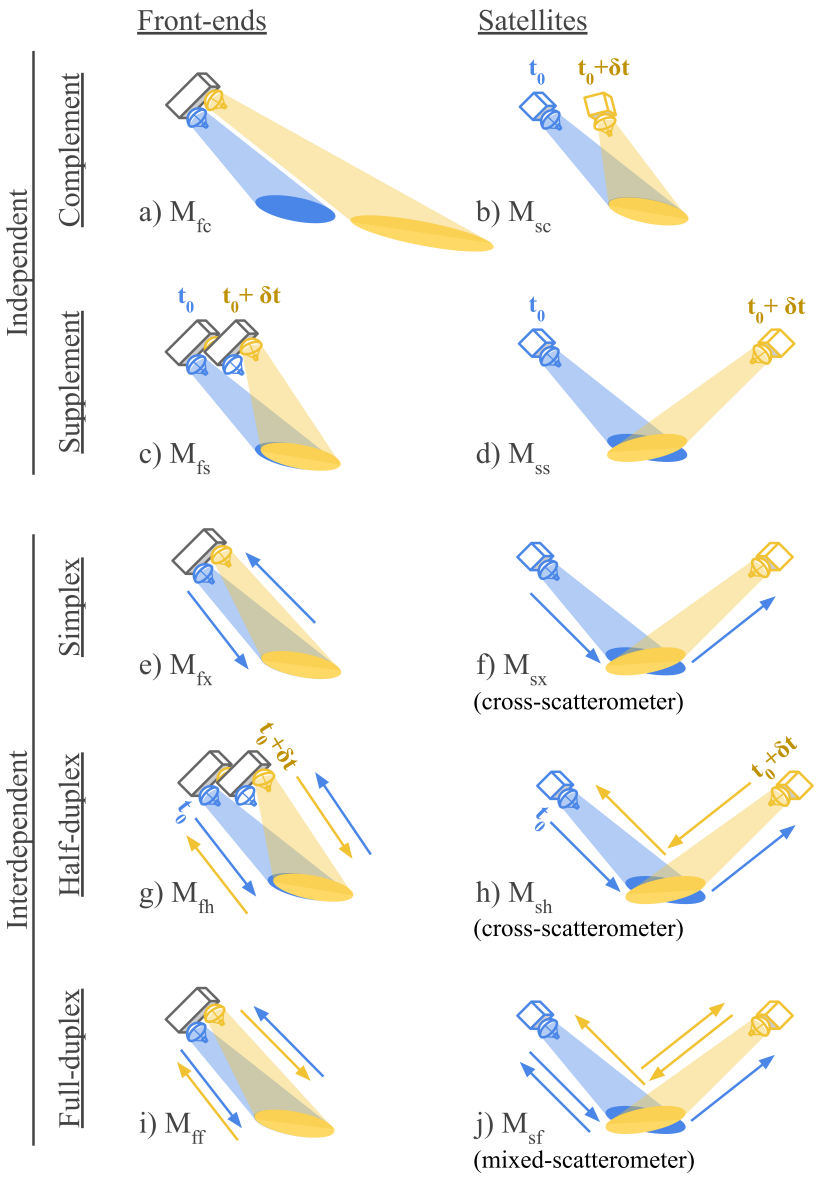

Figure 4.2: Illustration of possible modes of cooperation of multiple scatterometer satellites and front-ends. Separate antennas are used to symbolize separate front-ends, even though multiple front-ends could share a single antenna. a) Complementary front-ends use different geometries to expand the swath. b) Complementary satellites increase the revisit rate, viewing the same area on the ground in sequence. c-d) Supplementary satellites and front-ends measure the same area on the ground at different times with different flavors. e-f) Simplex satellites and front-ends form unique transmit/receive nodes of a scattering link. g-h) Half-duplex satellites and front-ends take turns transmitting the signal and receiving it. j-k) Full-duplex satellites and front-ends transmit and receive the scatter of their own and their cooperator's transmissions.

Chapter 5

Full-system Parametric Extrema Model for Satellite Wind Scatterometry

A fast parametric model of the scatterometer system can speed up the search for designs capable of hourly, global measurement of wind vectors over the surface of the ocean. Previous authors have modeled key aspects of scatterometer performance using closed-form equations suitable for the fast parametric system modeling described in Chapter 3, but a full-system model has not previously been available. This chapter builds on that work and presents a full-system parametric model for satellite scatterometers measuring wind vectors over the surface of the ocean. Previous versions of the model were presented in [34]–[36].

The model comprises two main aspects of the scatterometer: the instrument and the satellite bus. Instrument performance metrics include wind vector accuracy and speed dynamic range (Section 5.1), spatial resolution (Section 5.2), and revisit period (Section 5.3). Satellite bus metrics include net average power supply (Section 5.4), remaining battery power after umbra (Section 5.5), extreme temperatures (Section 5.7), net data transfer (Section 5.8), net data storage (Section 5.9), and cost (Section 5.10). This chapter presents derivations of performance metrics first, given as bold capitals (e.g., $\boldsymbol{Y}$) followed by derivations of the intermediate parameters that contribute to the performance metric, given in functional notation (e.g., $y(\cdot)$). The parametric model is summarized in Section 5.11. The model is validated

by comparison to the actual performance of NSCAT, QuikSCAT, ASCAT, and RFSCAT in Chapter 6.

5.1 Accuracy and Dynamic Range

Wind measurement accuracy and dynamic range are difficult to approximate in closed form because they are functions of multiple measurements with varying look geometry. To handle this, I substitute wind measurement accuracy and dynamic range with proxy performance metrics, including the normalized standard deviation of the σ_0 measurements, the incidence angle range of the measurements, radar wavelength, radar polarization, and number of "flavors".

Radar Signal

Normalized standard deviation is widely used to quantify the accuracy of σ_0 measurements. The bias in σ_0 measurements is also important, but I assume that it is minimized by good design practice. The normalized standard deviation of a σ_0 measurement is given in Eq. 13.118 of Ulaby and Long [1]. Including the multi-pulse coherence approximation given as Eq. 2.15 of Richards et al. [31], the normalized standard deviation, $\boldsymbol{K_p}$, becomes

$$\boldsymbol{K_p} \approx \frac{1}{M_{sc}} \left(\frac{1}{\sqrt{n_d}} \right)^{1+C_I} \sqrt{1 + \frac{2}{S_N} + \frac{2}{S_N^2}} \ , \tag{5.1}$$

where M_{sc} is the multiple of independent, complementary satellites whose measurements are combined, $S_N(\cdot)$ is the measurement signal-to-noise ratio for a single pulse, C_I is the coherence of integration, a Boolean parameter equal to one if integration is coherent and zero if it is not, and $n_d(\cdot)$ is the number of looks by a single radar in a single dwell. Satellite cooperative modes are defined in detail in Chapter 4 and their impacts to scatterometer system performance are summarized in Section 5.11.

The number of looks in a single radar dwell period is

$$n_d = \frac{T_d}{T_\tau} \ , \tag{5.2}$$

where T_d is the dwell time in which multiple pulses are integrated into a single scatter measurement and $T_\tau(\cdot)$ is the pulse repetition interval. The cutoff between one dwell and the next is chosen to minimize the loss caused by non-overlapping pulses (see Section 5.1).

The pulse repetition interval can be expressed as

$$T_\tau = \frac{M_{fs} M_{fc} M_{fh} M_{sh} n_b \tau}{n_{rf} D_r} \ , \tag{5.3}$$

where τ is the pulse length, n_b is the burst count or number of pulses transmitted together and then received together, D_r is the radar duty cycle, M_{fs} and M_{fc} are the multiples of independent supplementary and complementary front-ends, M_{fh} and M_{sh} are the multiples of half-duplex front-ends. $M_{fs}M_{fc}M_{fh}$ front-ends share n_{rf} simultaneous radar signals, so they operate in turns unless the n_{rf} signals are generated simultaneously. Satellite and front-end multiples are defined in detail in Chapter 4 and their impacts to scatterometer system performance are summarized in Section 5.11. The pulse repetition interval, pulse length, and burst count, among other timing elements, are illustrated in Fig. 5.1.

Two modes of pulse operation are illustrated in Fig. 5.1: single pulse and burst. In single pulse transmission and reception, the radar waits to transmit another pulse until after the previous pulse is received. In burst transmission and reception, multiple pulses are batched together in the time before the first pulse returns. The radar waits to transmit another burst until the previous burst is received. Burst operation requires the pulses to be distinguishable in post processing. This could be done using different frequencies (indicated using different colors in Fig. 5.1). For single pulse transmission, n_b should be set to 1 and T_n should be set equal to T_τ.

Assuming constant range and antenna gain across the measurement cell, the signal-to-noise ratio is given in Eq. 2.30 of Richards et al. [31]. Substituting Eq. 2.1 ($\sigma = \sigma_0 A_c$) into this equation. The SNR equation becomes

$$S_N = \frac{P_t G_t G_r \boldsymbol{\lambda}^2 \sigma_0 A_c}{(4\pi)^3 R_s^4 k T_0 F B_r L} \tau B_t \ , \tag{5.4}$$

where P_t is the transmit power, $G_t(\cdot)$ and $G_r(\cdot)$ are the transmit and receive gains, $\sigma_0(\cdot)$ is the wind-dependent normalized radar cross-section, $A_c(\cdot)$ is the measurement cell area,

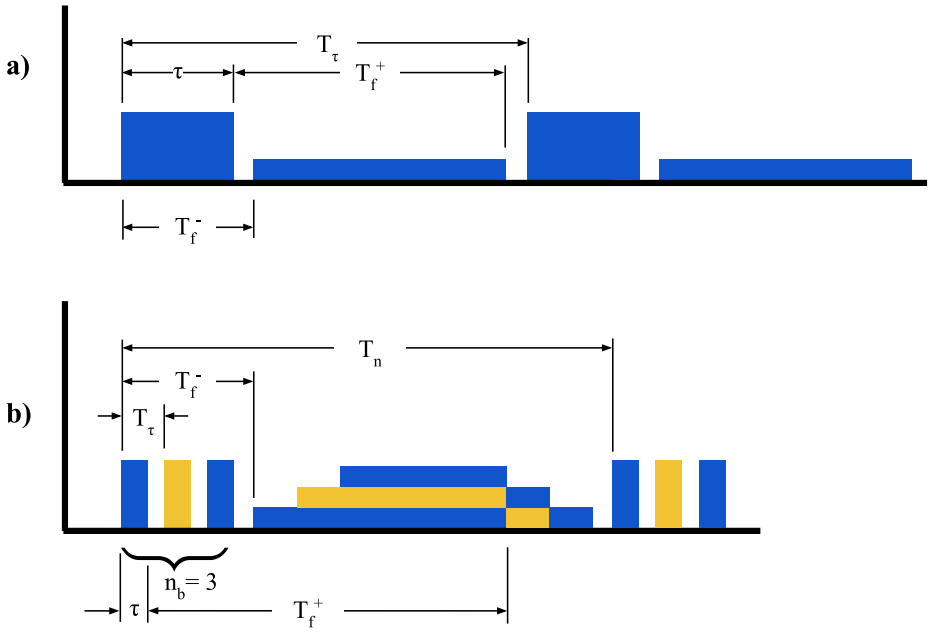

Figure 5.1: Timing illustration of pulse transmission and reception. Tall boxes represent the transmitted pulses while short boxes represent the received echos off the surface. (a) Single pulse transmission and reception. (b) Burst transmission and reception. Different colors indicate different frequencies used to differentiate the pulses in the burst in receive processing.

τ is the pulse length, $B_t(\cdot)$ and B_r are the transmit and receive bandwidths, $R_s(\cdot)$ is the slant range, k is Boltzmann's constant, $T_0 = 290$ K is the standard temperature, $F(\cdot)$ is the receiver noise figure, $L(\cdot)$ is the signal loss, and $\boldsymbol{\lambda}$ is the radar signal wavelength, which is also a proxy performance metric.

Wavelength, $\boldsymbol{\lambda}$, directly impacts dynamic range and accuracy since higher wavelengths are more deeply attenuated by rain. Full vector wind geophysical model functions exist for L-band (24 cm), C-band (5 cm), and Ku-band (2.1 cm). The wavelength is a function of frequency as

$$\boldsymbol{\lambda} = c/f \ , \tag{5.5}$$

where f is the frequency and c is the speed of light in vacuum.

For ICW pulse compression, the transmit bandwidth is

$$B_t = \frac{1}{\tau} \tag{5.6}$$

where τ is the pulse width. For LFM-ICW pulse compression, the transmit bandwidth is the chirp bandwidth,

$$B_t = f^+ - f^- \ , \tag{5.7}$$

where f is the transmit frequency.

Backscatter

The extrema of the Ku-band normalized radar cross-section, σ_0, are approximated from the NSCAT geophysical model function [37] using a 7th-order polynomial fit with vertical polarization. I approximate the minimum case of σ_0 as occurring when the angle between the wind and look directions is $\chi = 90°$ and the wind speed is $U = 3$ m/s. I approximate the maximum case of σ_0 as occurring when $\chi = 180°$ and $U = 30$ m/s. A plot of σ_0 versus incidence angle, azimuth angle, and wind speed is given in Fig. 5.4, which demonstrates the applicability of these extreme approximations. The coefficient of determination, R^2, and root-mean-squared error (RMSE) for the minimum and maximum fits are also given in Table 5.1.

Plots of GMF values for σ_0 as a function of incidence angle, the curve fit, and the error function are given in Fig. 5.2 for the minimum case and Fig. 5.3 for the maximum case. Using MATLAB's "poly7" curve fit, the GMF normalized radar cross-section as a function of incidence angle is approximately

$$\sigma_0(dB) \approx p_7\theta^7 + p_6\theta^6 + p_5\theta^5 + p_4\theta^4 + p_3\theta^3 + p_2\theta^2 + p_1\theta + p_0 \tag{5.8}$$

where θ is the incidence angle and the coefficients, p_n, for the minimum and maximum cases of σ_0 are given in Table 5.1.

Look Geometry

Incidence angle, $\boldsymbol{\theta}$, can be used as a proxy metric for wind vector dynamic range, because the σ_0 dynamic range increases with incidence angle as the projection of the ocean surface

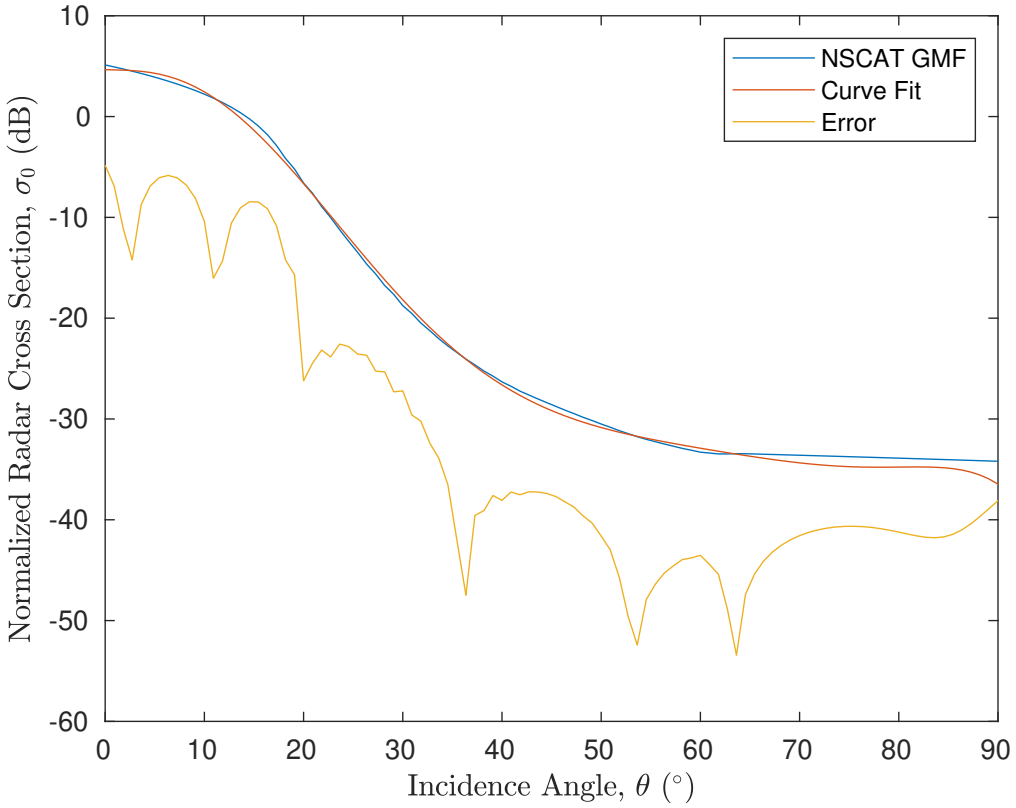

Figure 5.2: 7th-order polynomial curve fit of the *minimum* Ku-band backscatter, σ_0, as a function of incidence angle, θ, for azimuth angle $\chi = 90°$ and wind speed $U = 3$ m/s. For simplicity, only vertical polarization is considered here. The data relating backscatter and incidence angle are taken from the NSCAT geophysical model function [37].

waves along the line-of-sight grows [1]. This relationship is illustrated in Fig. 5.5. Typically, measurements must have an incidence angle greater than 18° and less than 65° to be usable in wind retrieval (see Chapter 16 of Ulaby and Long [1]).

The measurement incidence angle is derived by assuming a spherical Earth, by assuming the orbit is circular, and by defining the look-Earth-angle triangle given in Fig. 5.6. Using the Law of Sines,

$$\frac{\sin(\pi-\theta)}{R_E+h} = \frac{\sin\varphi}{R_E} \ , \tag{5.9}$$

where h is the mean satellite orbital altitude, φ is the elevation look angle, and R_E is the radius of the Earth. Substituting the supplementary angle identity, $\sin(\pi-\theta) = \sin\theta$, into

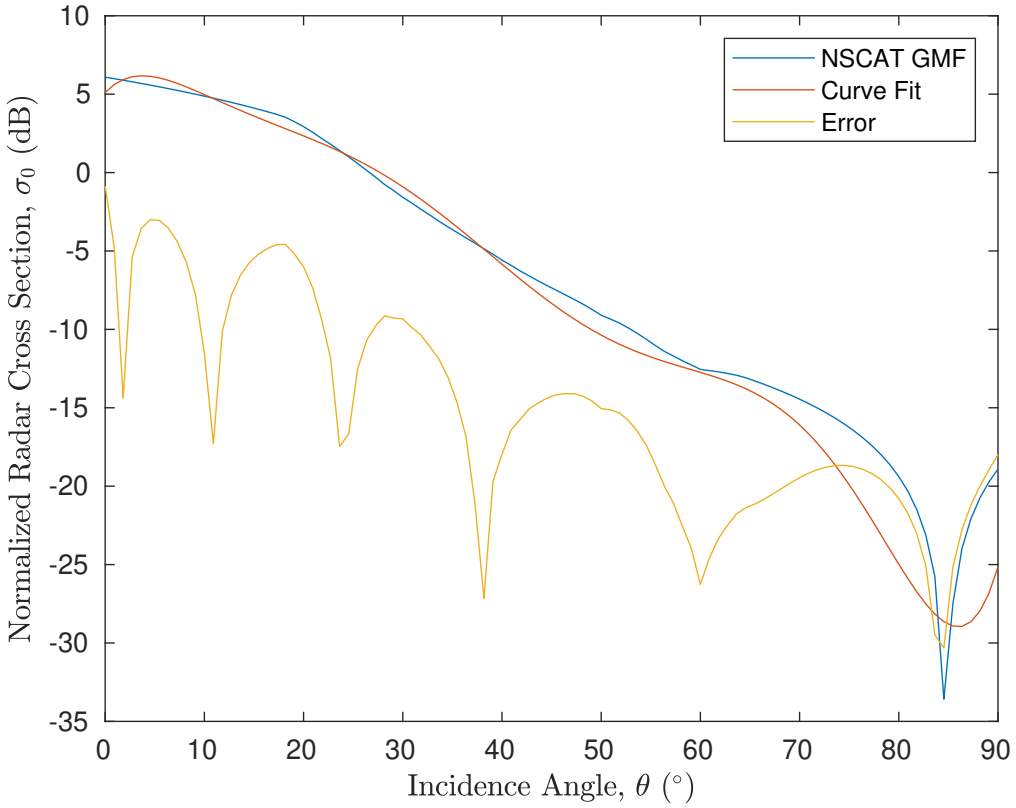

Figure 5.3: 7th-order polynomial curve fit of the *maximum* Ku-band backscatter, σ_0, as a function of incidence angle, θ, for azimuth angle $\chi = 180°$ and wind speed $U = 30$ m/s. For simplicity, only vertical polarization is considered here. The data relating backscatter and incidence angle are taken from the NSCAT geophysical model function [37].

Eq. 5.9 yields the incidence angle function,

$$\theta(\varphi, h) = \sin^{-1}\left(\sin\varphi \frac{R_E + h}{R_E}\right) . \tag{5.10}$$

As illustrated in the front view of Fig. 5.7, the incidence angles occurring at the near and far edges of the swath are

$$\begin{aligned} \boldsymbol{\Theta}^{-}_{edge} &= \theta\left[\varphi^{-}_{edge}, h\right] , \\ \boldsymbol{\Theta}^{+}_{edge} &= \theta\left[\varphi^{+}_{edge}, h\right] , \end{aligned} \tag{5.11}$$

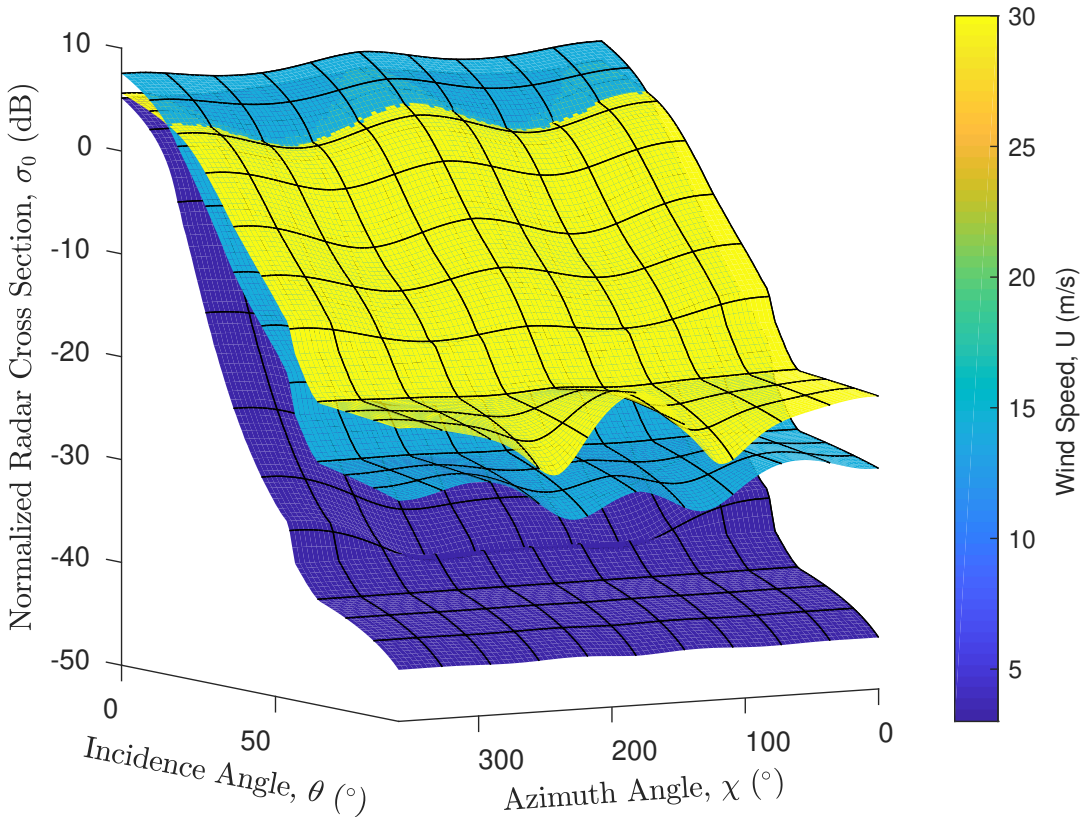

Figure 5.4: Backscatter versus incidence angle, wind speed, and azimuth angle, taken from the NSCAT geophysical model function [37]. The minimum backscatter generally occurs at azimuth angle $\chi = 90°$ and wind speed $U = 3$ m/s. For simplicity, only vertical polarization is considered here. The maximum backscatter generally occurs at azimuth angle $\chi = 180°$ and wind speed $U = 30$ m/s.

where φ^{-}_{edge} and φ^{+}_{edge} are the look angles at the near and far edges of the beam,

$$\begin{aligned} \varphi^{-}_{edge} &= \varphi - \frac{P\theta_{31} - !P\max(\theta_{31}, \theta_{32})}{2} \ , \\ \varphi^{+}_{edge} &= \varphi + \frac{P\theta_{31} + !P\max(\theta_{31}, \theta_{32})}{2} \ , \end{aligned} \tag{5.12}$$

where P is the scanning precession, a Boolean parameter equal to 1 if the satellite precesses as it scans and 0 if it does not. The ! operator expresses negation. θ_{31} and θ_{32} are the first and second beamwidths, which are aligned with the x and y directions when the antenna is pointed in the cross-track direction, as illustrated in Fig. 5.7.

Table 5.1: Coefficients, p_i, coefficient of determination, R^2, and root-mean-squared-error, RMSE, for a 7th-order polynomial curve of Ku-band normalized radar cross-section (in dB) as a function of incidence angle (in radians), taken from the NSCAT GMF. The minimum σ_0 occurs when $\chi = 90°$ and $U = 3$ m/s. The maximum σ_0 occurs when $\chi = 180°$ and $U = 30$ m/s.

	Minimum σ_0 Model	**Maximum σ_0 Model**
$\boldsymbol{p_0}$	-175	5.107
$\boldsymbol{p_1}$	970.5	37.86
$\boldsymbol{p_2}$	-2075	-424.3
$\boldsymbol{p_3}$	2073	1645
$\boldsymbol{p_4}$	-866.2	-3314
$\boldsymbol{p_5}$	37.68	3463
$\boldsymbol{p_6}$	-2.068	-1780
$\boldsymbol{p_7}$	4.657	355.1
$\boldsymbol{R^2}$	0.9993	0.9819
RMSE	0.3926	1.317

The look Earth angle, $\alpha(\varphi, h)$, can also be derived using the geometry of Fig. 5.6. The angles of the triangle add up to π, so $\alpha + \varphi + (\pi - \theta) = \pi$, and the look Earth angle as a generic function of φ and h is

$$\alpha(\varphi, h) = \theta(\varphi, h) - \varphi \ , \tag{5.13}$$

where $\theta(\varphi, h)$ is the incidence angle function and φ is the elevation look angle defined in Fig. 5.6, which is the center of the antenna beam unless otherwise specified.

Antenna Characteristics

According to Ulaby et al. [38], the one-way normalized gain pattern of a uniformly illuminated aperture is

$$F_{n\downarrow} = \left(2 \frac{J_1(\nu)}{\nu} \right)^2 \ , \tag{5.14}$$

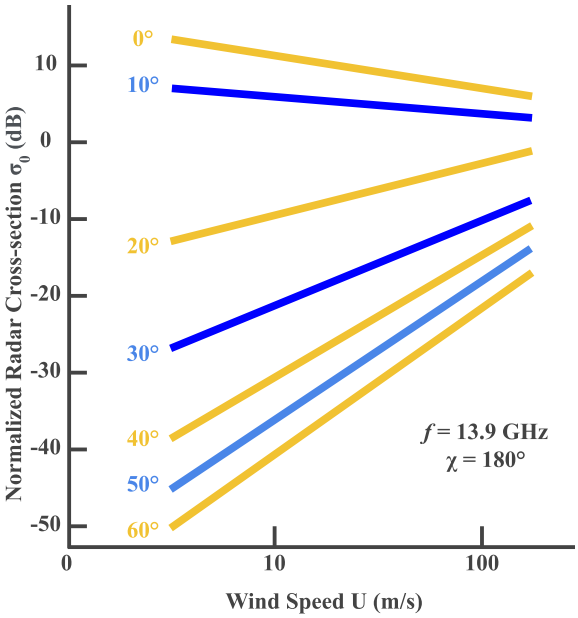

Figure 5.5: Illustration of normalized radar cross-section versus wind speed for $\chi = 180°$ and $f = 13.9$GHz at various incidence angles, taken from Ulaby and Long, Chapter 16 [1]. This demonstrates the relationship between incidence angle and σ_0. The dynamic range (minimum to maximum) of σ_0 is seen here to vary with incidence angle.

where $J_1()$ is the first-order Bessel function of the first kind, $\nu = \pi L \sin\theta_b/\boldsymbol{\lambda}$, L is the antenna length, θ_b is the angle from the center of the beam, and $\boldsymbol{\lambda}$ is the wavelength.

The two-way, normalized gain pattern is the product of the transmit and receive antenna gain patterns. Assuming the transmit and receive antenna patterns are identical, the two-way, normalized gain pattern becomes the square of Eq. 5.14,

$$F_{n\updownarrow} = \left(2\frac{J_1(\nu)}{\nu}\right)^4 . \tag{5.15}$$

The half-power beamwidth of the two-way, normalized gain pattern can be found by solving $F_{n\updownarrow} = 0.5$ for θ_b

$$\begin{aligned} \left(2\frac{J_1(\nu)}{\nu}\right)^4 &= \frac{1}{2} , \\ \frac{J_1(\nu)}{\nu} &\approx 0.42 , \end{aligned} \tag{5.16}$$

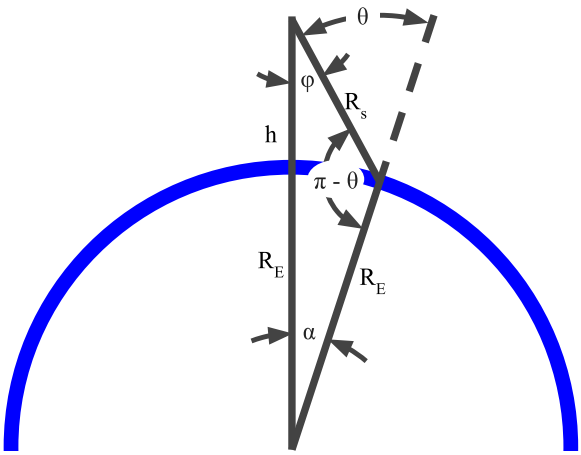

Figure 5.6: Illustration of the look Earth angle triangle, which is defined by the elevation look angle, φ (the angle between satellite nadir and the radar signal direction), the Earth angle between nadir and the measurement cell, α, and the angle $\pi - \theta$, where θ is the incidence angle. The triangle has as its sides the radius of the Earth, R_E, the radar signal slant range, R_s, and the distance from the center of the Earth to the satellite, $R_E + h$, where h is the satellite altitude.

Solving for ν using Wolfram Alpha, substituting $\nu = \pi L \sin\theta_b / \boldsymbol{\lambda}$, solving for θ_b, doubling, and using the small angle approximation, the two-way, half-power beamwidth becomes

$$\theta_{3\updownarrow} = 2\sin^{-1}\left(\frac{0.37\boldsymbol{\lambda}}{L}\right) \approx \frac{0.74\boldsymbol{\lambda}}{L} \ , \tag{5.17}$$

where the small angle approximation is used, $\boldsymbol{\lambda}$ is the wavelength, and L is the antenna length.

In Equation 9.4 of Richards et al. [31], the one-way, uniformly illuminated beamwidth is multiplied by a beamwidth factor, α to account for weighting. Likewise, I multiply the two-way, uniformly illuminated beamwidth with the square of the beamwidth factor. With directionality added, the two-way beamwidths become

$$\theta_{31} = \frac{0.74\alpha_1\boldsymbol{\lambda}}{L_1}, \ \theta_{32} = \frac{0.74\alpha_2\boldsymbol{\lambda}}{L_2} \tag{5.18}$$

where α_1 and α_2 are the beamwidth factors (corresponding to η_a, as described in Chapter 9 of Richards et al. [31]) for the first and second beamwidths. L_1 and L_2 are the antenna lengths corresponding to the first and second beamwidths.

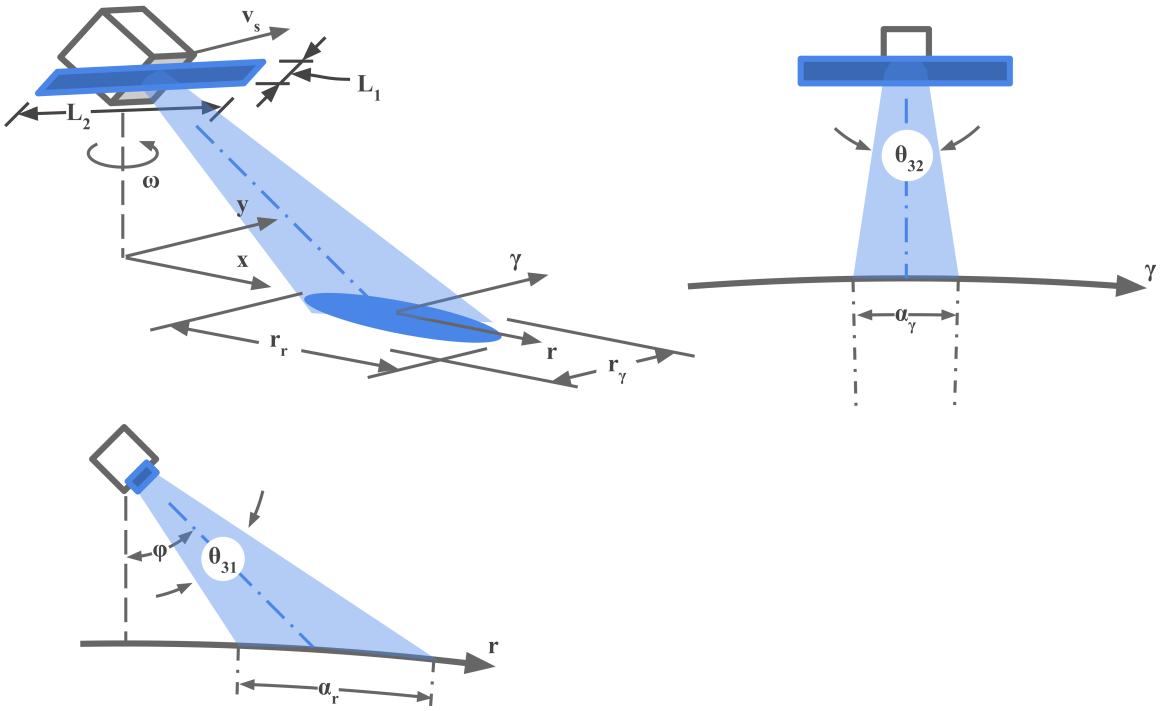

Figure 5.7: Illustration of antenna, beamwidth, and footprint geometry. Isometric (top left), right (top right), and front (bottom left) views are shown of a scanning scatterometer observing the ground. The radar beam is shown in light blue and the footprint is shown in dark blue. The antenna is approximated as a rectangular aperture with first and second beamwidths defined as the beamwidths in the radial and azimuthal directions when the scatterometer is pointed in the cross-track direction, as illustrated here. The first and second antenna lengths are defined as the antenna lengths corresponding to the first and second beamwidths. The radial and azimuthal directions are marked by r and γ. α_r and α_γ are the radial and azimuthal footprint Earth angles. The radar antenna is shown in blue mounted on a satellite shown in black.

The antenna gain is given in Eq. 9.5 of Richards et al. [31] as

$$G = \frac{\eta_e \eta_a 4\pi A_a}{\lambda^2} \tag{5.19}$$

where η_e is the antenna loss efficiency, η_a is the aperture efficiency, and $A_a(\cdot)$ is the antenna aperture area, which is defined as

$$A_a = L_1 L_2 F_a \tag{5.20}$$

where F_a is the antenna shape factor, L_1 and L_2 are the first and second antenna lengths that are defined as the antenna lengths corresponding to beamwidths, assumed to be aligned

with the cross-track and along-track directions when the antenna is pointed in the cross-track direction, as illustrated in Fig. 5.7. The antenna shape factor is the ratio of the actual antenna area with lengths, L_1 and L_1, to the area of a rectangular antenna with the same lengths. For example, for rectangular antennas, the antenna factor is $F_a = 1$, and for elliptical antennas, the antenna shape factor can be shown to be $F_a = \pi/4$.

Measurement Cell Geometry

The derivation of resolution cells from scatterometer measurements follow either a polar orientation or track orientation, as illustrated in Figs. 5.8-5.9. Using resolution cell widths with polar orientation, a rectangular cell approximation gives the minimum and maximum resolution cell areas as

$$\begin{aligned} A_c^- &\approx F_S^2 \min\left(r_{rx} r_{\gamma x}, r_{ry} r_{\gamma y}\right) , \\ A_c^+ &\approx F_S^2 \max\left(r_{rx} r_{\gamma x}, r_{ry} r_{\gamma y}\right) , \end{aligned} \tag{5.21}$$

where F_S is the spatial downsampling factor, r_{rx} and r_{ry}, are the radial resolutions at the cross-track (x) and along-track (y) and $r_{\gamma x}$ and $r_{\gamma y}$ are the azimuthal footprint widths in the x and y directions. Typically $F_S = 1$, but when multiple coherent pixels are combined, F_S can be larger than 1.

Alternatively using resolution cell widths with track orientation, a rectangular cell approximation gives the minimum and maximum resolution cell areas as

$$\begin{aligned} A_c^- &\approx F_S^2 \min\left(r_{xx} r_{yx}, r_{xy} r_{yy}\right) , \\ A_c^+ &\approx F_S^2 \max\left(r_{xx} r_{yx}, r_{xy} r_{yy}\right) , \end{aligned} \tag{5.22}$$

where F_S is the spatial downsampling factor, r_{xx} and r_{xy} are the cross track resolutions at the x and y axes and r_{yx} and r_{yy} are the along-track resolutions in the x and y directions.

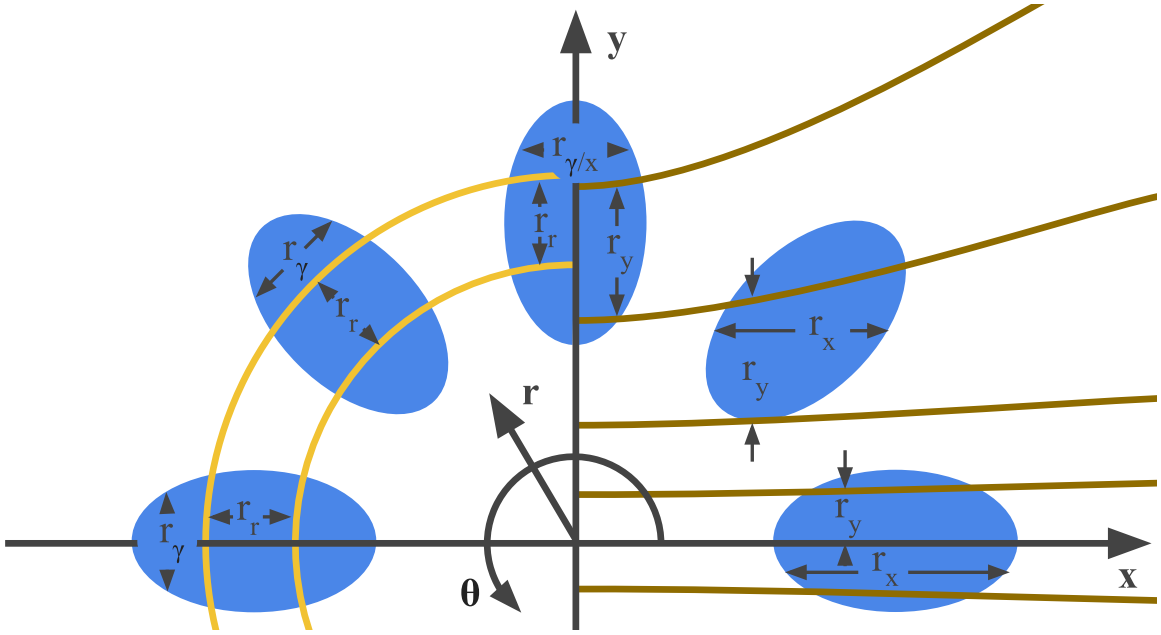

Figure 5.8: Illustration of resolution cells with track orientation (x, y) and polar orientation (r, γ) for various antenna and footprint orientations. The blue ellipse is the footprint. The brown lines on the right are iso-Doppler lines. The yellow lines on the left are iso-range lines. On the right half, the illustration shows the case of track resolution, where the radar beam is divided into resolution cells of along-track length defined by the Doppler resolution and cross-track length defined by the footprint width. On the left half, the illustration shows the case of polar resolution, where the radar beam is divided into resolution cells of radial length defined by the range resolution and azimuthal length defined by the footprint width.

Without resolution processing, the measurement cell side lengths are just the dimensions of the footprint, $r = a$, which are defined using polar orientation (see Figs. 5.8-5.9):

$$\begin{bmatrix} a_{rx} & a_{ry} \\ a_{\gamma x} & a_{\gamma y} \end{bmatrix} = \begin{bmatrix} a_r(\theta_{31}) & a_r(\theta_{32}) \\ a_\gamma(\theta_{32}) & a_\gamma(\theta_{31}) \end{bmatrix} \begin{bmatrix} 1 & !P \\ 0 & P \end{bmatrix}, \tag{5.23}$$

where P is the precession Boolean, equal to one if the satellite precesses and zero if it does not, a_{rx} and a_{ry}, are the radial footprint sizes at the cross-track (x) and along-track (y) axes, $a_{\gamma x}$ and $a_{\gamma y}$ are the azimuthal footprint sizes in the x and y directions, and θ_{31} and θ_{32} are the first and second beamwidth directions, aligned with the x-axis and y-axis when pointed in the cross-track direction, by definition. Whether the radial and azimuthal footprint sizes use the first or second beamwidth depends on whether precession occurs, so for clarity, the

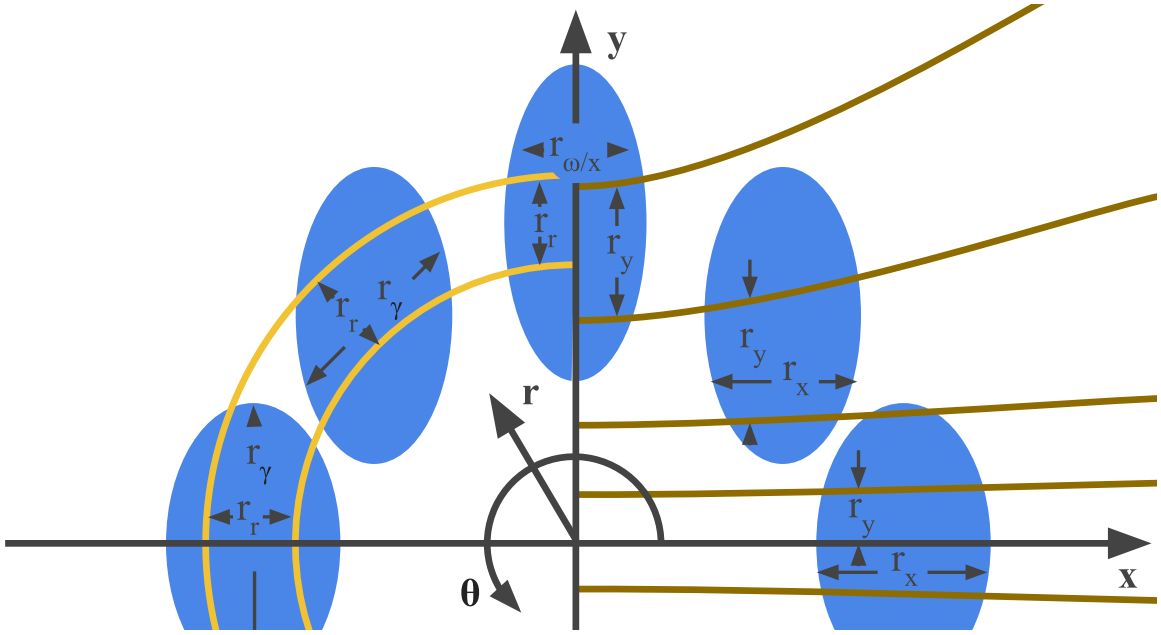

Figure 5.9: Illustration of footprints resulting from a precessed scan. Fig. 5.8 is here repeated, but the footprints are altered to reflect the impact of precession on the footprint. To make this impact discernible, the first beamwidth in this figure is shorter than the second beamwidth.

radial and azimuthal footprint sizes are expressed as generic functions of θ_3 and given below. The impact of precession on the footprint is illustrated in Fig. 5.9.

The footprint size is the projection of the beamwidth of the antenna on the ground. The radial and azimuthal footprint sizes are illustrated in Fig. 5.7 and their generic functions are

$$a_r(\theta_3) = \alpha_{r,edge}(\theta_3, h) R_E \ , \tag{5.24}$$

$$a_\gamma(\theta_3) = \alpha_\gamma(\theta_3) R_E \ , \tag{5.25}$$

where $\alpha_r(\theta_3, h)$ and $\alpha_\gamma(\theta_3, h)$ are the Earth angles subtended by the radial and azimuthal footprint sizes, expressed as generic functions of θ_3 and h.

The radial and azimuthal footprint Earth angles, α_r and α_γ, are derived similarly to the look Earth angle. They are subtended by the footprint width in the radial and azimuthal directions, which are illustrated in the isometric view of Fig. 5.7.

The radial footprint geometry is illustrated in the front view (bottom-left corner) of Fig. 5.7. The radial footprint Earth angle is the difference between the Earth angle of the

far end of the beam, α_{r1}, and the Earth angle of the near end, α_{r0}. Accounting for multiple beams and substituting the edge elevation look angles of Eq. 5.12 with the look Earth angle function of Eq. 5.13 yields functions for the radial footprint Earth angle, corresponding to the near and far edges of the swath,

$$\alpha_{r,edge}(\theta_3) = \alpha\left(\varphi + \frac{\theta_3}{2}, h\right) - \alpha\left(\varphi - \frac{\theta_3}{2}, h\right) , \tag{5.26}$$

where $\alpha(\varphi, h)$ is the look Earth angle function and φ is the look angle of the center of the beam.

The azimuthal footprint geometry is illustrated in the right-hand view of Fig. 5.7. Due to symmetry, the azimuthal footprint Earth angle is twice the Earth angle found when half the beamwidth, $\theta_3/2$, is used in place of the look direction in Eq. 5.13. Slant range, R_s, is also substituted for altitude. Thus, the function for the azimuthal footprint Earth angle is approximately

$$\alpha_\gamma(\theta_3) \approx 2\alpha\left(\frac{\theta_3}{2}, R_s\right) , \tag{5.27}$$

where $\alpha(\varphi, h)$ is the look Earth angle function and R_s is the slant range.

The footprint can be subdivided to further refine the measurement cell resolution, using either range, range-Doppler, or Doppler processing. Measurement cells using these processing methods are illustrated in Figs. 5.8-5.9. If range or LFM range-Doppler processing is used, as by QuikSCAT [39] and ASCAT [24], side lengths have polar orientation, as shown in the left half of Figs. 5.8-5.9. If Doppler processing is used, as by NSCAT [2], side lengths have track orientation, as shown in the right half of Figs. 5.8-5.9.

Accounting for potential precession, the radial and azimuthal resolutions using range or LFM range-Doppler processing and beamwidth are

$$\begin{bmatrix} r_{rx} & r_{ry} \\ r_{\gamma x} & r_{\gamma y} \end{bmatrix} = \begin{bmatrix} r_{rrd} & r_{rrd} \\ a_\gamma(\theta_{31}) & a_\gamma(\theta_{32}) \end{bmatrix} \begin{bmatrix} 1 & !P \\ 0 & P \end{bmatrix} , \tag{5.28}$$

where P is the precession Boolean, equal to one if the satellite precesses and zero if it does not, r_{rx} and r_{ry}, are the radial measurement cell widths at the cross-track (x) and along-track (y) axes, r_{rrd} is the measurement cell length derived through range or LFM range/Doppler processing, $r_{\gamma x}$ and $r_{\gamma y}$ are the azimuthal measurement cell widths in the x and y directions, $a_\gamma(\theta_3)$ is the azimuthal footprint width function given in Eq. 5.25, and θ_{31} and θ_{32} are the first and second beamwidth directions, aligned with the x-axis and y-axis when pointed in the cross-track direction, by definition.

Range processing divides the slant range as derived in Eq. 1.19 (ICW form) of Richards et al. [31] and Eq. 13.36 (LFM-ICW form) of Ulaby and Long [1] as

$$r_r = \frac{c}{2B_t} \ , \tag{5.29}$$

where c is the speed of light and B_t is the transmit bandwidth. Remember that an ICW signal has transmit bandwidth $B_t(\tau) = \frac{1}{\tau}$. For satellite scatterometry, Eq. 5.29 is projected on a locally flat surface as illustrated in Fig. 5.10, giving the resolution cell a radial side length of

$$r_{rrd} = \frac{c\cos\theta}{2B_t} \ , \tag{5.30}$$

where c is the speed of light, $\theta(\cdot)$ is the incidence angle (illustrated in Fig. 2.1), and B_t is the transmit bandwidth.

Accounting for potential precession, the cross-track and along-track resolutions using Doppler-only processing and beamwidth are

$$\begin{bmatrix} r_{xx} & r_{xy} \\ r_{yx} & r_{yy} \end{bmatrix} = \begin{bmatrix} a_r(\theta_{31}) & a_{\gamma y}/\max\left[a_{\gamma y}/a_r(\theta_{31}),\ \sin\psi\right] & a_\gamma(\theta_{32}) & a_\gamma(\theta_{31}) \\ r_{Dx} & 0 & r_{Dy} & r_{Dy} \end{bmatrix} \begin{bmatrix} S & 0 \\ !S & 0 \\ 0 & !P \\ 0 & P \end{bmatrix} \ , \tag{5.31}$$

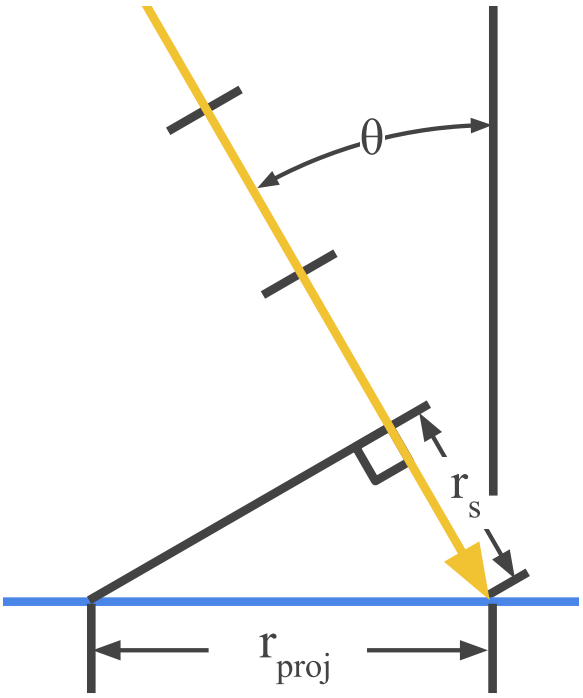

Figure 5.10: Illustration of the incidence angle and the range resolution projected on the ground. The radar beam is shown in yellow with black hash marks marking range resolution cells. The projected resolution cell is shown to depend on the incidence angle of the radar beam. The incidence angle is the angle between the local vertical and the radar beam.

where $S(\cdot)$ is the scanning Boolean parameter, P is the precession Boolean parameter and the ! operator expresses negation, r_{xx} and r_{xy} are the cross track resolutions at the x and y axes, r_{yx} and r_{yy} are the along-track resolutions in the x and y directions, r_{Dx} and r_{Dy} are the Doppler resolutions at the x and y axes, $a_r(\theta_3)$ and $a_\gamma(\theta_3)$ are the radial and azimuthal footprint width functions given in Eq. 5.24 and Eq. 5.25, and θ_{31} and θ_{32} are the first and second beamwidth directions, aligned with the x-axis and y-axis when pointed in the cross-track direction, by definition.

The scanning Boolean is expressed as a function of the scan rate as

$$S = \begin{cases} 0 & \omega = 0 \\ 1 & \omega > 0 \end{cases}, \tag{5.32}$$

where ω is the scanning rate.

Doppler processing generally divides the footprint in the along-track direction. Assuming a locally flat Earth, Doppler shift is given as a function of the position of the resolution cell in Eq. 13.26 of Ulaby and Long [1] as

$$f_D = -\frac{2v_s y}{\boldsymbol{\lambda}\sqrt{x^2+y^2+h^2}} \ , \tag{5.33}$$

where $v_s(\cdot)$ is the satellite speed, (x, y) are the coordinates of the resolution cell in the along-track and cross-track coordinate system, and h is the altitude of the satellite. The satellite speed is given in Equation B-3 by Elachi et al. [40] as

$$v_s = \sqrt{g_s R_E^2/(R_E+h)} \ , \tag{5.34}$$

where g_s is standard Earth gravity (~9.81 m/s).

For the closed-form model, spatial resolutions are derived at the x and y axes only, r_{Dx} and r_{Dy}. These cases are shown over iso-Doppler lines in Figs. 5.8-5.9. The spatial resolutions using Doppler processing corresponds to the Doppler resolution, f_D, which is derived in Chapter 17 of Richards et al. [31] as

$$\Delta f_D = |f_D(y+\Delta y) - f_D(y)| \approx \frac{0.89}{T_d} \ , \tag{5.35}$$

where T_d is the dwell time.

The minimum Doppler shift occurs along the x-axis. For $y << x$, Eq. 5.33 can be approximated as

$$f_D \approx -\frac{2v_s y}{\boldsymbol{\lambda}\sqrt{x^2+h^2}} \ . \tag{5.36}$$

For the case of minimum Doppler resolution, which occurs when the radar is looking to the side, the slant range is $R_s(\cdot) = \sqrt{x^2+h^2}$. By substituting this into Eq. 5.36, this can be further simplified to

$$f_D(y) \approx -\frac{2v_s y}{\boldsymbol{\lambda} R_s} \ , \tag{5.37}$$

where the slant range is derived as a function of design parameters using the look geometry in Fig. 5.6. Slant range can be solved from the law of sines as

$$R_s = \sin\alpha \frac{R_E}{\sin\varphi} \ , \tag{5.38}$$

where the slant range at the center of the beam is used for simplicity.

Because the Doppler shift is zero on the x-axis, where $y = 0$, Eq. 5.35 here becomes $\Delta f_D = |f_D(\Delta y)|$. Substituting this and Eq. 5.35 into Eq. 5.37 and solving for spatial resolution yields the minimum spatial resolution using Doppler processing in the cross-track direction:

$$r_{Dx} \approx \frac{0.89\boldsymbol{\lambda} R_s}{2T_d v_s} \ . \tag{5.39}$$

On the y-axis, when the antenna is pointing forward, $x = 0$, and Eq. 5.33 simplifies to

$$f_D = -\frac{2v_s y}{\boldsymbol{\lambda}\sqrt{y^2+h^2}} \ . \tag{5.40}$$

Substituting Eq. 5.40 into Eq. 5.35 yields

$$\frac{0.89}{T_d} = \left| -\frac{2v_s(y+\Delta y)}{\boldsymbol{\lambda}\sqrt{(y+\Delta y)^2+h^2}} + \frac{2v_s y}{\boldsymbol{\lambda}\sqrt{y^2+h^2}} \right| \ . \tag{5.41}$$

The term $\frac{y+\Delta y}{\sqrt{(y+\Delta y)^2+h^2}}$ is substituted with the first two terms of its Taylor series expansion at $\Delta y = 0$ (see Appendix B). This Taylor series approximation is best suited when $\Delta_y << y \approx h$. This is appropriate for satellites. Doppler won't be used if the Doppler resolution, Δ_y, is not much less than the surface range, y. Further, the surface range, y, is about equal to the altitude for larger look angles, where the maximum Doppler resolution occurs. The substitution yields an approximation for the maximum spatial resolution using Doppler processing:

$$\frac{0.89\boldsymbol{\lambda}}{2v_s T_d} \approx \left| -\left(\frac{y}{\sqrt{y^2+h^2}} + \frac{h^2\Delta y}{(y^2+h^2)^{\frac{3}{2}}} \right) + \frac{y}{\sqrt{y^2+h^2}} \right| = \frac{h^2\Delta y}{(y^2+h^2)^{\frac{3}{2}}} \ . \tag{5.42}$$

The maximum Doppler-derived resolution occurs in the forward looking case, so $R_s(\cdot) = \sqrt{y^2 + h^2}$. Substituting this into Eq. 5.42 and solving yields the maximum spatial resolution using Doppler processing in the along-track direction:

$$r_{Dy} = \Delta y \approx \frac{0.89 \boldsymbol{\lambda} R_s^3}{2 v_s T_d h^2} \ . \tag{5.43}$$

Losses

The total system loss, $L(\cdot)$, is

$$L = L_t L_r L_a L_{sp} L_s L_\tau L_e \ , \tag{5.44}$$

where $L_t < 3dB$ and $L_r < 3dB$ are the scatterometer transmit and receive losses (Section 2.7 of Richards et al. [31]), $L_a < 0.5dB$, is the atmospheric loss (inverse of transmission % given in Figure 1-19 of Elachi et al. [40]), $L_{sp} < 0.5dB$ is the signal processing loss due to quantization error (Chapter 13 of Richards et al. [31]), $L_s(\cdot)$ is the smear loss, $L_\tau(\cdot)$ is the pulse loss caused by the pulse transmission overlapping with pulse return, L_e is the echo loss caused by a receive bandwidth smaller than the combined transmit bandwidth and echo Doppler shift. Eq. 5.44 is adapted from Equation 2.16 of Richards et al. [31] with the addition of the smear loss.

Smear loss is the result of motion of the footprint between the beginning of the transmit pulse and the end of receive. Smear loss is dominated by antenna rotation. Satellite motion is not usually significant. For a scanning scatterometer, the area from which signal is received is shifted away from the area to which the signal is transmitted, so the useable area is, at worst, reduced to the overlapping area of the first transmit and final receive beam of the pulse repetition interval, $T_\tau(\cdot)$, as illustrated in Fig. 5.11. This reduction is expressed as a smear loss, $L_s(\cdot)$. For simplicity, in this calculation, the antenna gain pattern is assumed to be uniform and the footprint is assumed to be square. Thus, the smear loss is approximately

$$L_s \approx \frac{2}{1 - \frac{S_d}{a_\gamma}} = \frac{2 a_\gamma}{a_\gamma - S_d}, \tag{5.45}$$

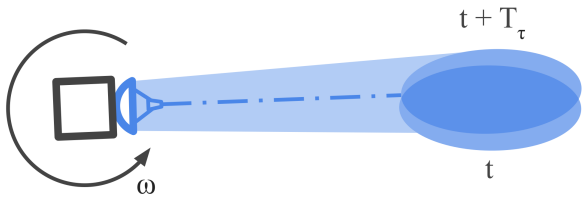

Figure 5.11: Smear loss illustration. The satellite with antenna pointed at the ground is rotating at rate ω. While the beam is scanned, the area from which signal is received (ending at time $t+T_\tau$) is shifted away from the area to which signal is transmitted (starting at time t), so the useable area is, at worst, reduced to the overlapping area of the first transmit and final receive beam of the pulse repetition interval, T_τ. This reduction is expressed as a smear loss, L_s.

where $a_\gamma(\cdot)$ is the azimuthal footprint width and $S_d(\cdot)$ is the dwell step. The minimum and maximum of the cross-track and along-track azimuthal footprint width should be used for the minimum and maximum smear losses.

The dwell step, $S_d(\cdot)$, is the distance travelled by the footprint over the course of a single dwell period, T_d. It is

$$S_d = R_g \omega T_d \tag{5.46}$$

where ω is the scan rate, T_d is the dwell time, and $R_g(\cdot)$ is the ground range, which is defined as the distance between the sub-satellite point and the center of the footprint. The ground range is

$$R_g = \alpha R_E \ , \tag{5.47}$$

where α is the look Earth angle.

Pulse loss is caused by timing overlap between one pulse and the echo of another pulse. Pulse loss is illustrated in Fig. 5.12. In the case of Fig. 5.12a, the pulse length, τ and/or the burst count, n_b, should be reduced. In the case of Fig. 5.12b, the pulse (or burst) repetition interval should be increased. Pulse loss can be expressed as

$$L_\tau = \max\left(1, \frac{n_b \tau}{T_f}\right) \max\left(1, M_{fh} M_{sh} \frac{\tau + T_f}{T_\tau}\right) \ , \tag{5.48}$$

where M_{fh} and M_{sh} are the multiples of half-duplex antennas and satellites, n_b is the burst count or number of pulses transmitted together and then received in together, τ is the pulse

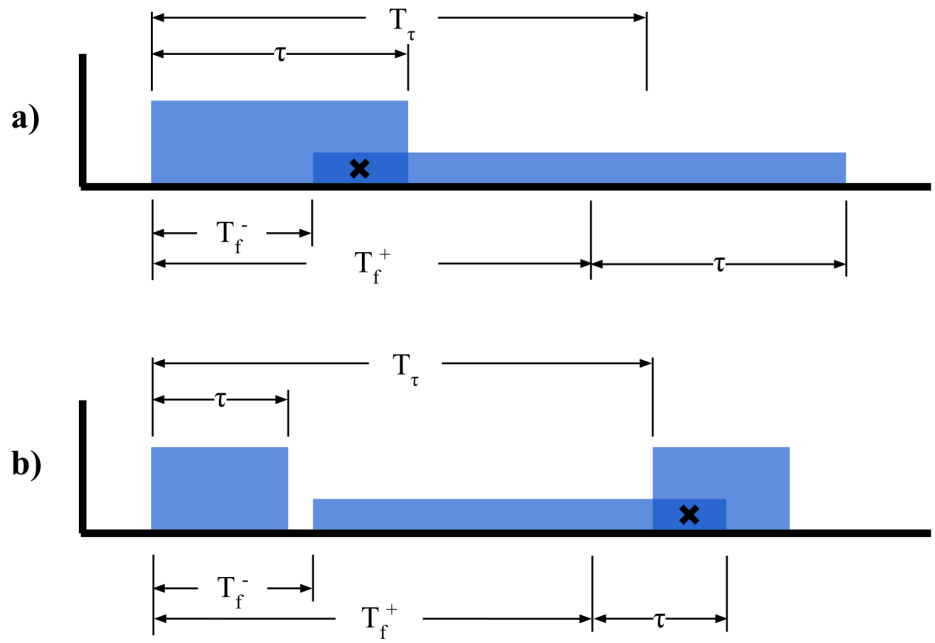

Figure 5.12: Pulse overlap loss is caused by (a) the pulse or burst of pulses continuing after the beginning of the echo arrives at the radar or (b) the next pulse being transmitted before the end of the echo arrives at the radar. In the case of bursts, substitute the one pulse in the figure with a burst of pulses and substitute the pulse repetition interval, T_τ, for the burst repetition interval, T_b.

length, $T_f(\cdot)$ is the pulse time of flight, and T_τ is the pulse repetition interval. The max function ensures that non-overlap is not counted as a gain. Satellite and front-end multiples are defined in detail in Chapter 4 and their impacts to scatterometer system performance are summarized in Section 5.11.

The loss due to part of the echo being outside the receiver bandwidth, or echo loss, depends on whether the radar compensates for the Doppler shift dynamically. If it does not compensate, then the Doppler loss is

$$L_D = \max\left(1, \frac{B_t + 2f_{D,e}}{B_r}\right), \tag{5.49}$$

where B_t and B_r are the transmit and receive bandwidths and $f_{D,e}(\cdot)$ is the two-way echo Doppler shift.

If the radar compensates for changing Doppler shifts throughout the scan, but not across the footprint, then the Doppler loss is

$$L_D = \max\left(1, \frac{B_t + B_D}{B_r}\right) , \tag{5.50}$$

where B_t and B_r are the transmit and receive bandwidths and $B_D(\cdot)$ is the Doppler bandwidth across the the combined footprint.

If the radar compensates for different Doppler bandwidths across the scan and across different measurement cells within each footprint, then the Doppler loss is

$$L_D = \max\left(1, \frac{B_t + B_{D,c}}{B_r}\right) , \tag{5.51}$$

where B_t and B_r are the transmit and receive bandwidths and $B_{D,c}(\cdot)$ is the Doppler bandwidth across a single measurement cell.

The two-way echo Doppler shift is

$$f_{D,e} = \frac{2v_c}{\lambda} , \tag{5.52}$$

where $v_c(\cdot)$ is the radial velocity in the direction of the measurement cell and λ is the radar wavelength.

The derivation of the radial velocity is illustrated in Fig. 5.13. The radial velocity in the direction of the measurement cell is

$$v_c = v_s \sin\varphi , \tag{5.53}$$

where $v_s(\cdot)$ is the satellite velocity and φ is the look direction, or the direction of the measurement cell measured from nadir.

The Doppler bandwidth across the combined footprint is

$$B_D = f_{D,e}^{+} - f_{D,e}^{-} , \tag{5.54}$$

where $f_{D,e}$ is the echo Doppler shift.

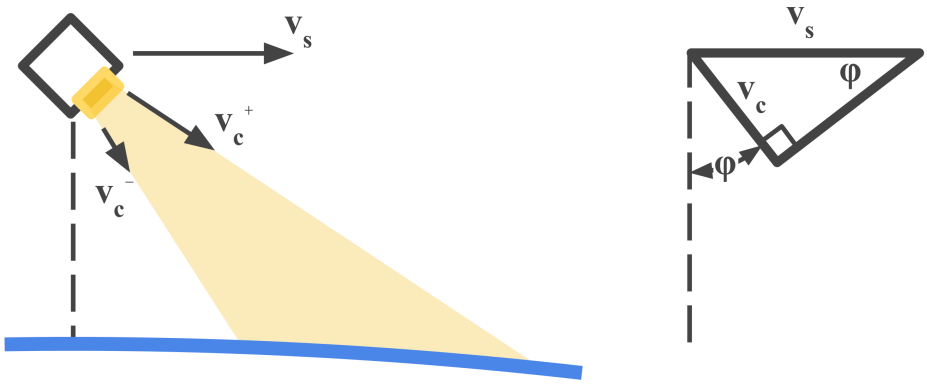

Figure 5.13: (left) Doppler shift geometry. A scatterometer beam (yellow) illuminates the Earth's surface (blue). Arrows indicate the satellite velocity vector, v_s, and the range radial velocity vectors, v_c. (right) The right triangle used in finding the radial velocities, v_c.

The Doppler bandwidth across a single measurement cell is approximately

$$B_{D,c} = B_D \frac{r_y}{a_y} \ , \tag{5.55}$$

where $B_D(\cdot)$ is the Doppler bandwidth across the footprint, $r_y(\cdot)$ is the along-track resolution, and $a_y(\cdot)$ is the along-track footprint width.

The along-track footprint width is

$$a_y = (R_g^+ - R_g^-) \sin\psi \ , \tag{5.56}$$

where R_g is the ground range and ψ is the azimuth look angle measured from the cross track direction.

The time of flight is the time it takes for a signal to arrive at the surface and return to the transmitter (see Fig. 5.1 and Fig. 5.12). It is

$$T_f = 2\frac{R_s}{c} \ , \tag{5.57}$$

where $R_s(\cdot)$ is the slant range and c is the speed of light.

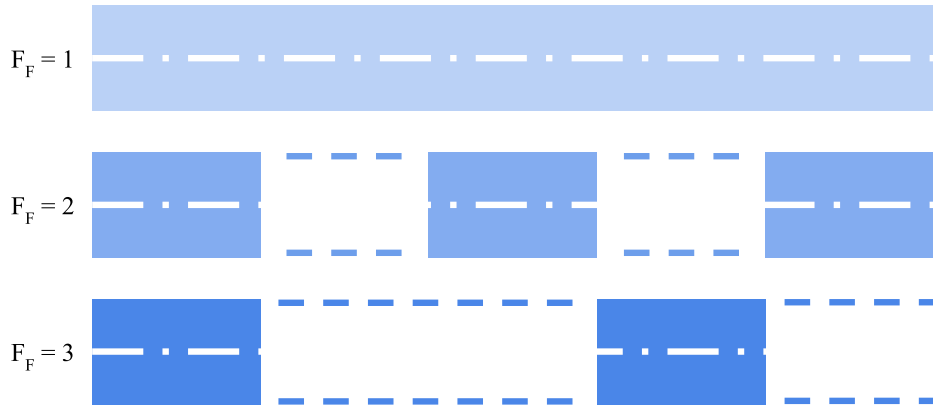

Figure 5.14: Illustration of focus factor. Several satellite swaths are shown in blue. The white centerlines are the subsatellite track or center of the swath. The top swath has focus factor $F_F = 1$, meaning the satellite uses a consistent scan pattern for all points on its path, giving all areas equal attention. The middle and bottom swaths have focus factors $F_F = 2$ and $F_F = 3$, meaning the satellite takes the time that it would have observed the white areas and observes the blue areas instead, obtaining two and three times as many flavors of the blue areas at the expense of linear coverage.

Measurement Flavors

The number of flavors, $\boldsymbol{F}$, impacts wind retrieval, especially wind direction accuracy, as described in Section 2.1. It is approximated as

$$\boldsymbol{F} \approx M_{fs} M_{ss} M_{fh} M_{sh} \left(M_{ff} \frac{(M_{ff}+1)}{2} \right) \left(M_{sf} \frac{(M_{sf}+1)}{2} \right) F_F F_\omega \ , \tag{5.58}$$

where M_{fs}, M_{fh} and M_{ff} are the multiples of independent, supplementary, half-duplex and full-duplex front-ends, M_{ss}, M_{sh} and M_{sf} are the multiples of independent, supplementary, half-duplex and full-duplex satellites, F_F is the focus factor, and $F_\omega(\cdot)$ is the scan factor. The focus factor is the degree to which one region along the satellite path is prioritized over others, illustrated in Fig. 5.14. Satellite and front-end multiples are defined in detail in Chapter 4 and their impacts to scatterometer system performance are summarized in Section 5.11.

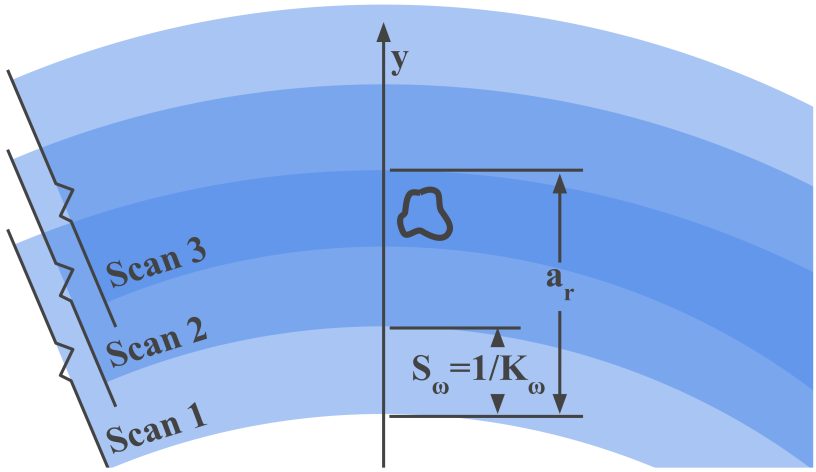

Figure 5.15: Illustration of overlapping scans resulting from a scan factor greater than one. A measurement cell area of arbitrary shape is outlined in black. Several subsequent scans are are shown in translucent blue. For a circularly scanning satellite with its footprint width larger than its scan step, S_ω, the measurement cell will be revisited by multiple scans in a row. This applies to most of the swath, but for the edges of the swath (not shown) the number of re-scan looks may be greater.

The scan factor determines whether scanning adds flavors, as illustrated in Fig. 5.15, or skips some areas, giving them fewer flavors, as illustrated in Fig. 5.16.

$$F_\omega = \begin{cases} 2M_{fc}a_{ry}K_\omega & \omega > 0 \\ 1 & \omega = 0 \end{cases}, \tag{5.59}$$

where $K_\omega(\cdot)$ is the spatial scan rate, or inverse of the scan step (the along-track distance between one scan and the next), $a_{ry}M_{fc}$ is the composite footprint width, or the product of a the radial width of a single footprint in the along-track direction, $a_{ry}(\cdot)$, and the multiple of independent, complementary front-ends with different incidence angles, M_{fc}, assuming that each antenna has the same aperture dimensions, L_1 and L_2. The ratio of the composite footprint to the scan step is doubled to account for incoming and outgoing scans. Satellite and front-end multiples are defined in detail in Chapter 4 and their impacts to scatterometer system performance are summarized in Section 5.11.

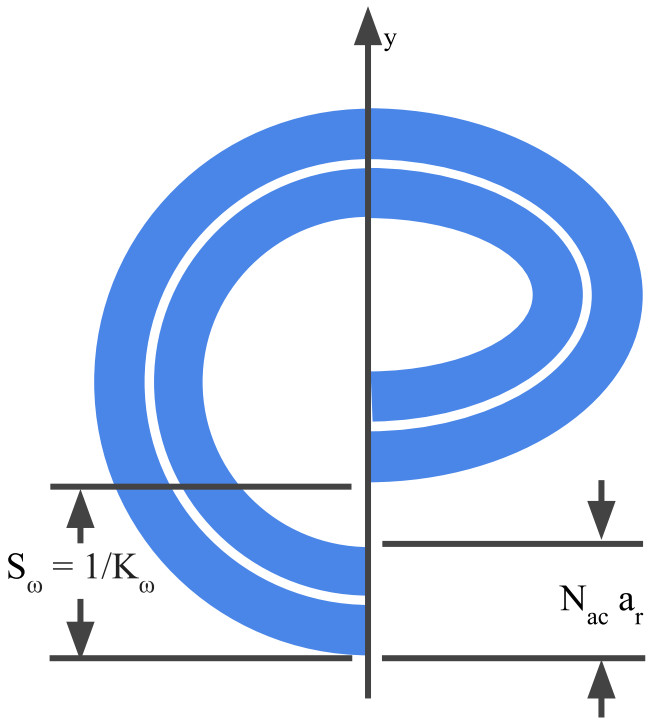

Figure 5.16: Illustration of gaps between scans resulting from a scan factor less than one. $S_\omega = 1/K_\omega$ is the scan step, the distance along the sub-satellite path between one scan and the next.

The spatial scan rate, K_ω, is

$$K_\omega = \frac{\omega}{2\pi v_g} \ , \tag{5.60}$$

where v_g is the satellite velocity projected on the ground. Assuming a spherical Earth and neglecting Earth rotation, the satellite ground velocity is approximately

$$v_g \approx \frac{2\pi R_E}{T_s} \ , \tag{5.61}$$

where R_E is the Earth's radius and $T_s(\cdot)$ is the satellite orbital period, which is given in Equation B-4 by Elachi et al. [40] as

$$T_s = 2\pi(R_E + h)/v_s \ , \tag{5.62}$$

where h is the satellite altitude and $v_s(h)$ is the satellite speed.

5.2 Spatial Resolution

The average spatial resolution, $\bar{\boldsymbol{r}}$, is

$$\bar{\boldsymbol{r}} = \sqrt{A_c} \ , \tag{5.63}$$

A_c is the measurement cell area. This approximation neglects post-measurement resolution enhancement schemes [41].

5.3 Revisit Period

The revisit period, $\boldsymbol{T_r}$, is the average time between one measurement and the next at a given location. Neglecting orbital precession, the revisit period for a single satellite is roughly the time it takes for the Earth to rotate underneath it, T_E. Additional satellites in various orbits decrease the revisit period approximately linearly, as

$$\boldsymbol{T_r} \approx \frac{T_E}{N_o C} \ , \tag{5.64}$$

where T_E =23.93 hrs is the rotational period of the Earth or sidereal day (the time it takes for the Earth to rotate underneath the satellite), N_o is the number of orbital planes in the constellation, and C is the fraction of the globe covered by a single satellite in a single day. If the satellite doesn't cover the whole globe by itself, C is less than unity and makes it take longer than a day for revisits to occur on average. If the satellite covers the globe more than once in a day, then C is greater than unity and causes revisits to occur more frequently than once per day.

Eq. 5.64 is meant to be an approximate average, assuming all orbits have the same inclination. Actual revisit time for a given region depends on its latitude. A constellation with a variety of orbits of varying inclination angle may have a shorter average revisit than estimated here.

The satellite can be modeled as having a simple coverage, C_s, of all of Earth's surface between the minimum and maximum latitudes of its swath, Ω, reduced by gaps (or increased by overlaps) between passes, C_e, and gaps due to downtime and diversions from normal

operations, C_l. The daily coverage fraction is then the product of these:

$$C \approx C_s C_e C_l \ . \tag{5.65}$$

The simple daily coverage fraction is the fraction of the globe between the minimum latitude and the maximum latitude of its swath, Ω, as illustrated in Fig. 5.17. Assuming a spherical Earth, the coverage fraction in this simplified case is the ratio of two symmetrical spherical zones given by Weisstein [42] (with $R_E \sin(\Omega)$ substituted for h) to the surface area of the Earth. The "simple" coverage is thus

$$C_s = \frac{2\Big(2\pi R_E[\sin(\Omega)R_E]\Big)}{4\pi R_E^2} = \sin\Omega \ , \tag{5.66}$$

where R_E is the Earth radius and Ω is the extreme latitude of the swath.

Ω is $I + \alpha(\varphi^+_{edge})$ for a circular orbit with inclination, I of domain (0, $\pi/2$), $\alpha^+_{edge} = \alpha(\varphi^+_{edge})$ is the maximum Earth angle of the swath. Typically, launch inclinations are expressed over (0, π) to account for both prograde and retrograde orbits. As a result, I has a domain of (0, π) and Ω is

$$\Omega = \frac{\pi}{2} - \max\left(\left|\frac{\pi}{2} - I\right| - \alpha(\varphi^+_{edge}), 0\right) \ . \tag{5.67}$$

The change in coverage due to gaps or overlap between passes is approximated as the coverage fraction due to gaps or overlap at the equator, the equatorial coverage, C_e. As illustrated in Fig. 5.18, the equatorial coverage is the ratio of the swath width projected on the equator, $W_s \sin I$, to the orbit step, S_o, i.e.,

$$C_e = \frac{W_s / \sin I}{S_o} \ , \tag{5.68}$$

where, W_s is the swath width, I is the orbital inclination, and S_o is the orbit step. This is an approximate change in coverage which may overestimate the amount of the globe missed due to equatorial gaps.

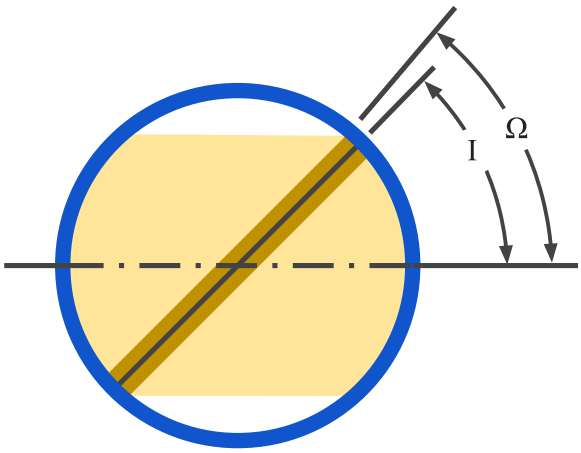

Figure 5.17: Simplified model of coverage of the Earth by a single satellite based on satellite inclination and swath width. The outline of the Earth is shown in blue, with the equator shown as a horizontal centerline in black. The satellite swath is shown in burnt yellow with the simplified area of the globe covered light yellow. I is the orbital inclination and Ω is the max latitude covered by the swath.

The swath width, $W_s(\cdot)$, is derived using an Earth angle method as

$$W_s \approx \begin{cases} 2\left[\alpha(\varphi^+)R_E + \frac{1}{2}a_{rx}\right] & \omega > 0 \\ M_{fc}\cos(\psi^-)\left(\left[\alpha(\varphi^+)R_E + \frac{1}{2}a_{rx}\right] - \left[\alpha(\varphi^-)R_E - \frac{1}{2}a_{rx}\right]\right) & \omega = 0 \end{cases}, \tag{5.69}$$

where $\alpha(\varphi)$ is the look Earth angle function, given in Eq. 5.13, φ is the look angle of the center of the beam, ψ is the azimuth look angle of the fixed beams, measured from the x-axis (cross-track), R_E is the radius of the Earth, a_{rx} is the radial footprint width in the cross-scan direction, M_{fc} is the number of independent, complementary front-ends.

The orbit step, S_o, is the distance between the sub-satellite track at one equatorial crossing and the next. It is given in degree-form in Section B-1-4 of Elachi et al. [40] as

$$S_o = 360° \frac{N}{L} \tag{5.70}$$

where 360° is the angular extent of an orbit and $\frac{N}{L}$ is the ratio of satellite orbital revolutions to Earth revolutions, which can be expressed in terms of the satellite orbital period, T_s, and

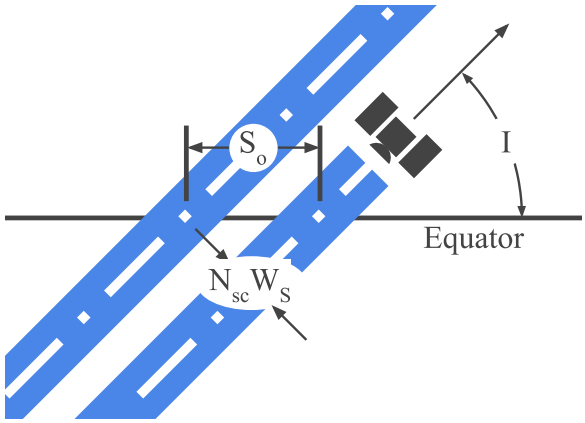

Figure 5.18: Equatorial coverage geometry. S_o is the orbit step, the equatorial distance between the sub-satellite path on one orbit and the sub-satellite path on the next orbit.

Earth's rotation period, T_E, as follows

$$\frac{N}{L} = \frac{N}{L}\frac{2\pi t_0}{2\pi t_0} = \frac{f_s}{f_E} = \frac{1/T_s}{1/T_E} = \frac{T_E}{T_s} \ , \tag{5.71}$$

where t_0 is unit time, f_s is the frequency of orbit of the satellite and f_E is the frequency of rotation of the Earth.

Substituting Eq. 5.71 into Eq. 5.70 and converting to distance-form by multiplying by the ratio of meters to degrees in the Earth perimeter, $\frac{2\pi R_E}{360^\circ}$, yields the final distance-form of the orbit step:

$$S_o = 2\pi R_E \frac{T_s}{T_E} \ , \tag{5.72}$$

When the scatterometer takes downtime to charge its batteries or cool off, or when it skips areas along its path as illustrated in Fig. 5.14, it results in a linear, along path reduction in coverage fraction, which can be modeled as

$$C_l = \min\left(\frac{U}{C_o}, 1\right)\frac{1}{F_F} \ . \tag{5.73}$$

where F_F is the focus factor, C_o is the fraction of the Earth covered by ocean, and the uptime, U, is the fraction of the orbit in which the scatterometer is operating.

5.4 Orbital Average Power Usage

The power system performance can be expressed as the ratio of power generated to power used over the course of the orbit. If the average orbital power usage is less than one, the power generation exceeds power consumption. On the other hand, insufficient power generation results in orbital average power usage greater than one, meaning the batteries will at times be drained of power and the system will require time to recharge. The orbital average power usage is

$$\boldsymbol{U_P} = \frac{\overline{P_s} + \overline{P_b}}{\overline{P_g}} \ , \tag{5.74}$$

where $\overline{P_g}(\cdot)$ is the average generated power, $\overline{P_s}(\cdot)$ is the average power consumed by the scatterometer, and $\overline{P_b}(\cdot)$ is the average power consumed by the satellite bus.

Power Generation

The average power generated by solar panels, $\overline{P_g}$, is

$$\overline{P_g} = \overline{P_S} + \overline{P_{S,d}} + \overline{P_E} - \overline{P_w} \ , \tag{5.75}$$

where $\overline{P_S}$ is the solar power generated during normal operations, $\overline{P_{S,d}}$ is the solar power generated during dedicated solar charging, $\overline{P_E}$ is the solar power generated from light reflected off the Earth, and $\overline{P_w}$ is the dedicated solar power generation wasted due to battery oversaturation.

The orbital average solar power generated during normal operations is

$$\overline{P_S} = \eta_S \overline{A_S} G_S (1 - D_{ch}) \ , \tag{5.76}$$

where η_S is the efficiency of the solar cells, $\overline{A_S(\cdot)}$ is the average sun-facing satellite solar panel area, G_S is solar irradiance in Earth orbit, and D_{ch} is the downtime for dedicated solar charging, which is the fraction of the orbit during which the satellite suspends normal operation and orients its largest solar-generating surface toward the sun.

The orbital average solar power generated during dedicated solar charging is

$$\overline{P_{S,d}} = P_{S,d} D_{ch} \ , \tag{5.77}$$

where $P_{S,d}$ is the instantaneous power generated during solar charging and D_{ch} is the charging downtime.

The instantaneous solar power dedicated during solar charging is

$$P_{S,d} = \eta_S A_{S,d} G_S \ , \tag{5.78}$$

where η_S is the efficiency of the solar cells, $A_{S,d}$ is the dedicated solar charging area, and G_S is solar irradiance in Earth orbit.

The orbital average solar power generated from light reflected off the Earth is given by Keesee [43] as

$$\overline{P_E} = \eta_S \, a \, \overline{A_E} \sin^2(\rho) \Big(0.664 + 0.521\rho + 0.203\rho^2\Big)\Big(1 - D_{ch}\Big) G_S \ , \tag{5.79}$$

where η_S is the efficiency of the solar cells, $\overline{A_E(\cdot)}$ is the average Earth-facing satellite solar panel area, a is the albedo of the Earth, ρ is the angular diameter of the Earth from the perspective of the satellite, D_{ch} is the charging downtime, and G_S is the solar irradiance in Earth orbit.

The orbital average power wasted due to saturation of the batteries is

$$\overline{P_w} = \frac{B_s I_c \overline{V_b}}{T_s} \ , \tag{5.80}$$

where $B_s(\cdot)$ is the battery saturation, $\overline{V_b}$ is the average battery voltage, T_s is the satellite orbital speed, and I_c is the battery current capacity, or the product of the current which the battery can deliver and the duration for which it can deliver that current.

The battery saturation is

$$B_s = \max\left(0, \frac{F_c D_{ch} P_{S,d} T_s}{I_c \overline{V_b}} - 1\right) \ , \tag{5.81}$$

where D_{ch} is the charging downtime, $P_{S,d}(\cdot)$ is the instantaneous dedicated charging power, T_s is the satellite orbital period, I_c is the battery current capacity, $\overline{V_b}$ is the average battery voltage, and F_c is the dedicated charging consecutivity, which is the largest fraction of the dedicated solar charging duty cycle that occurs consecutively, ranging from 0 to 1. For example, for a charging downtime of $D_{ch} = 20\%$ and a dedicated charging consecutivity of $F_c = 0.5$, the longest period over which the batteries must store solar-generated power is $D_{ch}F_c = 10\%$ of the orbit.

The average, sun-facing, solar panel area is

$$\overline{A_S} = \sum_{i=1}^{n} \eta_{x,i}\eta_{y,i}\eta_{z,i}C_{s,i}A_i \ , \tag{5.82}$$

where n is the number of panels defined, A_i is the area of the i^{th} panel, $C_{s,i}$ is the fraction of the i^{th} panel covered in solar cells, and $\eta_{x,i}(\cdot)$, $\eta_{y,i}(\cdot)$, and $\eta_{z,i}(\cdot)$ are the solar illumination efficiencies of the i^{th} panel due to rotation about the x, y, and z axes, averaged across the orbit.

For closed-form approximation of orbital average illumination, I define a solar illumination efficiency. The geometry of illumination efficiency is illustrated in Fig. 5.19. The illumination efficiency is defined generally as

$$\eta = \frac{A_p}{A} = \sin\psi \tag{5.83}$$

where A_p is the area of the projection of the surface normal to the illumination vector, A is the surface area of the panel, and ψ is the angle between the solar illumination vector and the normal of the face.

Finding the average solar illumination efficiencies across the course of an orbit involves integrating a nonlinear function, (see Appendix C). Instead, as illustrated in Fig. 5.20, I approximate the average solar illumination efficiency for each face about each rotation axis by taking the average of the solar illumination efficiency for four points in a circular orbit, given by the orbit Earth angle α_o (see Fig. 5.20). The orbital average solar illumination

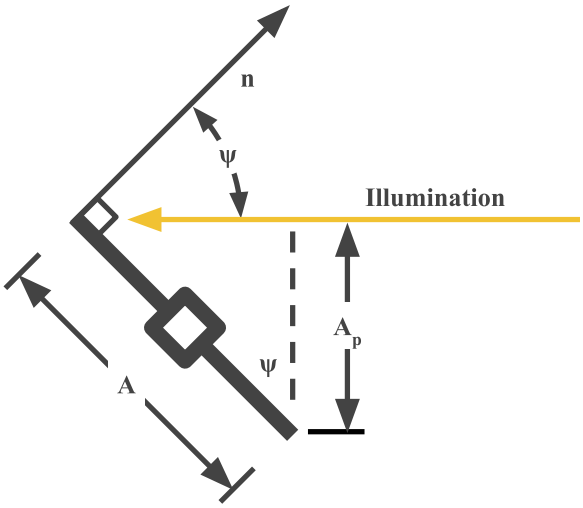

Figure 5.19: Illustration of illumination angle, ψ. Side view of a satellite with solar panels with incoming solar radiation shown in yellow. ψ is the angle between the normal to the plane of the solar panels and the solar rays. n is the panel normal vector. A is the surface area of the solar panel and A_p is the area of the solar panels projected in the direction of illumination.

efficiency approximation is

$$\begin{aligned}\overline{\eta_{u,i}} &= \frac{1}{4}\Bigg[(1-2F_u)\frac{\eta_{u,i}(\pi)+\eta_{u,i}(\pi/2)}{2} + \frac{\eta_{u,i}(\pi/2)+\eta_{u,i}(0)}{2} \\ &\quad + \frac{\eta_{u,i}(0)+\eta_{u,i}(-\pi/2)}{2} + (1-2F_u)\frac{\eta_{u,i}(\pi)+\eta_{u,i}(-\pi/2)}{2}\Bigg] \\ &= \frac{1}{4}\Big[\eta_{u,i}(0) + (1-F_u)\Big[\eta_{u,i}(\pi/2)+\eta_{u,i}(-\pi/2)\Big] + (1-F_u)\eta_{u,i}(\pi)\Big] \ ,\end{aligned} \tag{5.84}$$

where $F_u(h)$ is the fraction of time a spacecraft in a circular Earth orbit spends in umbra and $\eta_{u,i}(\alpha_o)$ is the solar illumination efficiency of the i^{th} face averaged over rotation about the u^{th} axis when the satellite's orbital position is at an Earth angle of α_o away from the sun.

If the satellite is not rotating, the solar illumination efficiencies as a function of orbital position are

$$\eta_{u,i}(\alpha_o) = \max\Big(0, \cos\Big[\psi_{u,i}(\alpha_o)\Big]\Big) \ , \tag{5.85}$$

where $\psi_{u,i}$ is the wrapped rotation angle with respect to the Sun and α_o is the Earth angle between the satellite and the sun direction.

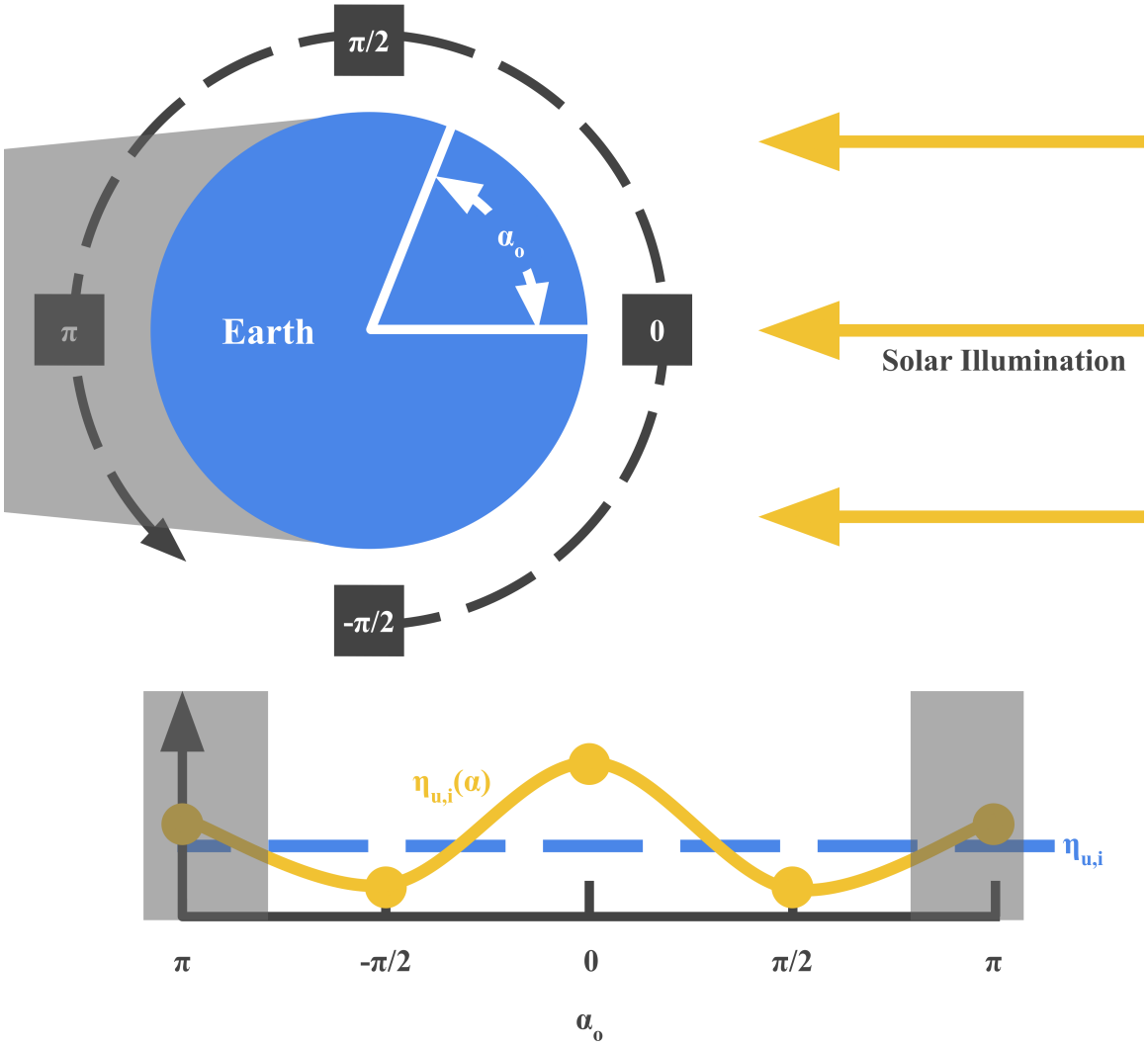

Figure 5.20: Top: Illustration of several different orbital positions with different Earth angles between the satellite and the illumination vector. The Earth angle value, α_o, for each orbital position is marked on the satellite. The umbra is indicated in gray. Bottom: A solar illumination efficiency curve, $\eta_{u,i}(\alpha)$ for a single panel across the orbit, along with the average solar illumination efficiency. The curve is averaged as in Eq. 5.84, due to the non-linearity of the solar illumination efficiency as a function of satellite rotation (see Appendix C). The umbra is represented by the vertical gray sections, demonstrating the impact of the umbra on the average illumination efficiency, $\eta_{u,i}$. The orbit is treated as nominally circular.

Table 5.2: Sun-facing surface offset angles for a rectangular prism. The offset for the i^{th} face about the u^{th} axis is the angle between the illumination direction to the normal of the face. The Sun-facing surface offset angle is used with the wrapping function of Eq. 5.87 to limit the illumination range for each face to the range of angles at which the face is illuminated by the Sun. The nominal offset of each face about each axis is given for several positions in a circular orbit, as illustrated in Fig. 5.21. α_o is the Earth angle between the sun direction and the satellite direction. Long dashes are used when rotating a face about that axis does not present the face to the sun.

	$\boldsymbol{\alpha = -\frac{\pi}{2}}$			$\boldsymbol{\alpha = 0}$			$\boldsymbol{\alpha = \frac{\pi}{2}}$			$\boldsymbol{\alpha = \pi}$		
i	**u:x**	**u:y**	**u:z**	**u:x**	**u:y**	**u:z**	**u:x**	**u:y**	**u:z**	**u:x**	**u:y**	**u:z**
1	—	$\frac{\pi}{2}$	$\frac{\pi}{2}$	—	β	0	—	$\frac{\pi}{2}$	$-\frac{\pi}{2}$	—	$\pi - \lvert\beta\rvert$	π
2	$\pi - \lvert\beta\rvert$	—	π	$-\frac{\pi}{2}$	—	$\frac{\pi}{2}$	$-\beta$	—	0	$-\frac{\pi}{2}$	—	$-\frac{\pi}{2}$
3	$\beta - \frac{\pi}{2}$	—	0	0	$\beta - \frac{\pi}{2}$	—	$\frac{\pi}{2} - \beta$	0	—	0	$\frac{\pi}{2} - \beta$	—
4	—	$-\frac{\pi}{2}$	$-\frac{\pi}{2}$	—	$\pi - \lvert\beta\rvert$	π	—	$-\frac{\pi}{2}$	$\frac{\pi}{2}$	—	$-\beta$	0
5	β	—	0	$\frac{\pi}{2}$	—	$-\frac{\pi}{2}$	$\pi - \lvert\beta\rvert$	—	π	$\frac{\pi}{2}$	—	$\frac{\pi}{2}$
6	$\beta + \frac{\pi}{2}$	—	0	0	$\beta + \frac{\pi}{2}$	—	$-\frac{\pi}{2} - \beta$	0	—	0	$-\frac{\pi}{2} - \beta$	—

For a rotating satellite, the solar illumination efficiencies as a function of orbital position are

$$\eta_{u,i}(\alpha_o) = \frac{\int_{\psi^-_{u,i}(\alpha_o)}^{\psi^+_{u,i}(\alpha_o)} \cos\psi d\psi}{\int_{\psi^-_u}^{\psi^+_u} d\psi} = \frac{\sin(\psi^+_{u,i}(\alpha_o)) - \sin(\psi^-_{u,i}(\alpha_o))}{\psi^+_u - \psi^-_u} \ , \tag{5.86}$$

where ψ_u is the total rotation range of the satellite about the u^{th} axis and $[\psi^-_{u,i}(\alpha_o), \psi^+_{u,i}(\alpha_o)]$ is the range of illumination angles for the i^{th} face about the u^{th} axis at the α_o point in a circular orbit. α_o points in the orbit are illustrated in Fig. 5.20.

To make Eq. 5.86 work, the rotation range of the satellite about the u^{th} axis, $[\psi^-, \psi^+]$, must be shifted by the offset angle of the i^{th} face about that axis, $\epsilon_{u,i}$. Having shifted the rotation range, the illumination angles are limited to the possible illumination range

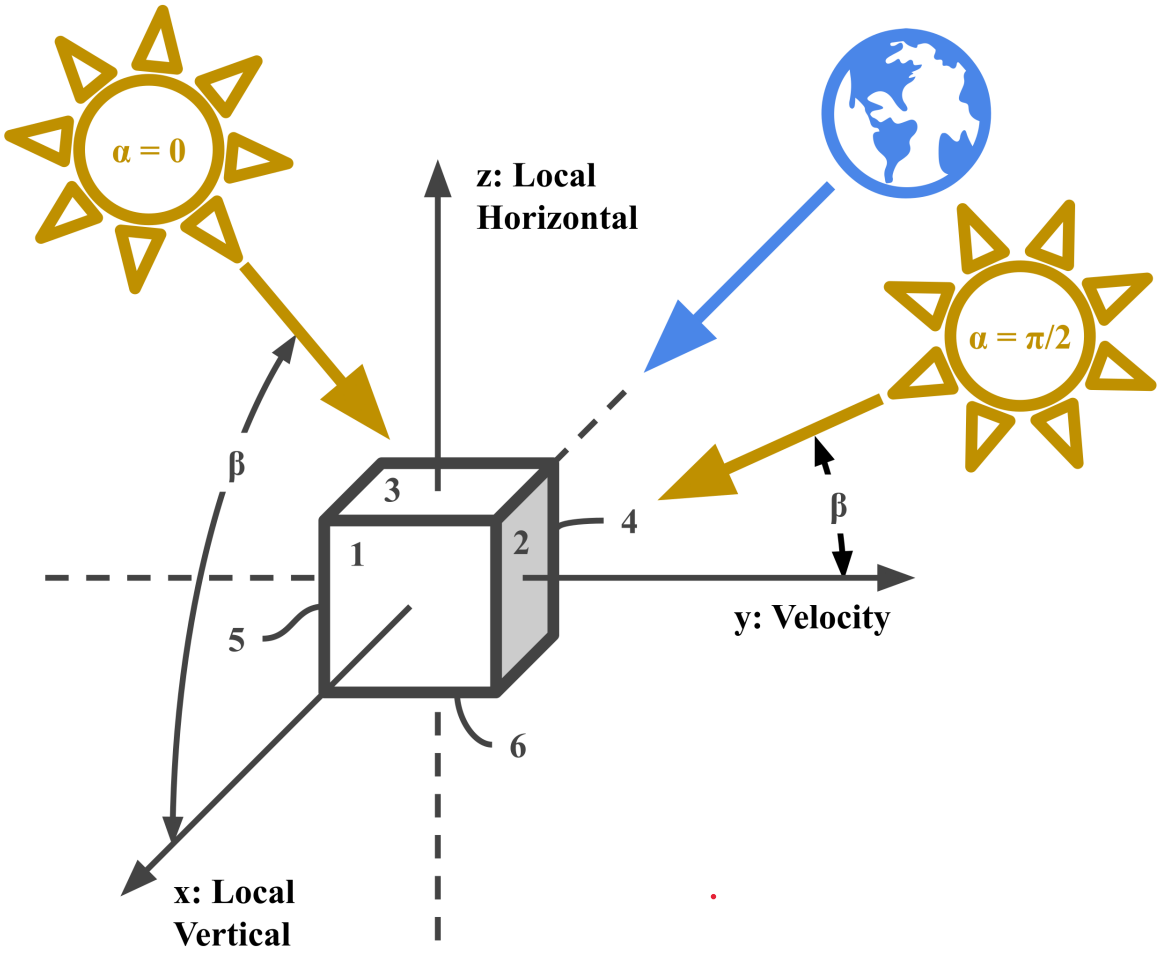

Figure 5.21: Illustration of the surface offset geometry for a variety of illumination scenarios. The offset for the i^{th} face about the u^{th} axis is the angle between the illumination direction to the normal of the face. A local vertical, local horizontal coordinate system is used, with velocity as the third axis under the assumption that the orbit is circular. Two solar illumination cases are illustrated: π, when the satellite is between the Earth and the sun, and $\pi/2$ when the satellite is to the side of the Earth with respect to the sun. The illumination offsets in each case depend on both the orbit position and the beta angle of the orbit. The Earth is assumed to nominally align with the x-axis, which is the down direction.

$[-\pi/2, \pi/2]$. This gives us the illumination angles of the i^{th} face,

$$[\psi^-_{u,i}(\alpha), \psi^+_{u,i}(\alpha)] = \left[\min\left(\frac{\pi}{2}, \max\left(-\frac{\pi}{2}, \psi^-_u + \epsilon_{u,i}(\alpha)\right)\right), \right. \tag{5.87}$$

$$\left. \min\left(\frac{\pi}{2}, \max\left(-\frac{\pi}{2}, \psi^+_u + \epsilon_{u,i}(\alpha)\right)\right)\right], \tag{5.88}$$

where $[\psi_u^-, \psi_u^+]$ is the range of rotation angles of the satellite about the u^{th} axis and $\epsilon_{u,i}(\alpha_o)$ is the offset angle of the i^{th} face about the u^{th} axis, given in Table 5.2. Note that generally, this range of rotation angles, $\psi_{u,i}$, should be limited to $[-\pi,\pi]$, unless rotation is continuous, in which case $[-2\pi, 2\pi]$ should be used to overcome the keyhole presented by this wrapping.

The fraction of time spent in umbra, F_u, is given by Sumanth [44] as

$$F_u = \begin{cases} 0 & |\beta| < \beta^* \\ \frac{1}{\pi}\cos^{-1}\left(\frac{\sqrt{h^2+2R_E h}}{(R_E+h)cos(\beta)}\right) & |\beta| \geq \beta^* \end{cases} \tag{5.89}$$

where $\beta(I)$ is the orbit beta angle, $\beta^*(\cdot)$ is the maximum beta angle at which the satellite spends time in the umbra, h is the satellite orbital altitude, and R_E is the Earth radius. The orbit is assumed to be circular.

The minimum and maximum orbit beta angles are

$$\begin{aligned} \beta^- &= 0 \\ \beta^+ &= I - \epsilon \end{aligned} \tag{5.90}$$

where $\epsilon = 0.13\pi$ is the obliquity of Earth's rotation and the absolute value of β is used, giving $\beta = 0$ as the minimum case.

The orbit umbra beta angle is given by Sumanth [44] as

$$\beta^* = \sin^{-1}\left(\frac{R_E}{R_E+h}\right) , \tag{5.91}$$

where R_E is the Earth radius and h is the orbit altitude.

The average Earth-facing charging area is

$$\overline{A_E} = \sum_{i=1}^{n} \zeta_{x,i}\zeta_{y,i}\zeta_{z,i}(1-F_u)C_{s,i}A_i \ , \tag{5.92}$$

where $\zeta_{x,i}(\cdot)$, $\zeta_{y,i}(\cdot)$, and $\zeta_{z,i}(\cdot)$ are the Earth illumination efficiencies of the i^{th} panel due to rotation about the x, y, and z axes, $C_{s,i}$ is the solar cell coverage of the i^{th} panel, $F_u(h)$ is the fraction of the orbit spent in umbra, and A_i is the surface are of the i^{th} panel.

If the satellite is not rotating, the Earth illumination efficiencies as a function of orbital position are

$$\zeta_{u,i} = \max\left(0, \cos\psi_{E,u,i}\right) , \tag{5.93}$$

where $\psi_{E,u,i}$ is the wrapped rotation angle given in Eq. 5.95.

If the satellite is rotating, the Earth illumination efficiencies are

$$\zeta_{u,i} = \frac{\int_{\psi^-_{E,u,i}}^{\psi^+_{E,u,i}} \cos\psi d\psi}{\int_{\psi_u^-}^{\psi_u^+} d\psi} = \frac{\sin(\psi^+_{E,u,i}) - \sin(\psi^-_{E,u,i})}{\psi_u^+ - \psi_u^-} \tag{5.94}$$

where the rotation ranges are wrapped to the Earth-illumination range for the i^{th} face, in like manner as Eq. 5.87. The range of Earth-illumination angles is

$$\left[\psi^-_{E,u,i}, \psi^+_{E,u,i}\right] = \left[\min\left(\frac{\pi}{2}, \max\left(-\frac{\pi}{2}, \psi_u^- + \xi_{u,i}\right)\right), \right. \tag{5.95}$$

$$\left. \min\left(\frac{\pi}{2}, \max\left(-\frac{\pi}{2}, \psi_u^+ + \xi_{u,i}\right)\right)\right] , \tag{5.96}$$

where ψ_u^- and ψ_u^+ are the rotation extrema about the u^{th} axis and $\xi_{u,i}$ is the Earth illumination offset of the i^{th} face from the u^{th} axis, given in Table 5.3.

Power Consumption

The average power consumed by the scatterometer, $\overline{P_s}$, is

$$\overline{P_s} = P_s U , \tag{5.97}$$

where $P_s(\cdot)$ is the scatterometer operating power, which is

$$P_s = n_{rf} \frac{P_t D_r}{\eta_{DC}\eta_r} , \tag{5.98}$$

where n_{rf} is the number of radar signals generated simultaneously by the scatterometer system, P_t is the peak forward transmit power, D_r is the radar duty cycle, η_{DC} is the efficiency

Table 5.3: Earth-facing surface offset angles for a rectangular prism. The offset for the i^{th}, $\xi_{u,i}$, face about the u^{th} axis is the angle between the illumination direction to the normal of the face. The Earth-facing surface offset angle is used to limit the illumination range for each face to the range of angles at which the face is illuminated by the Earth. Surface offset angles are illustrated in Fig. 5.21.

	Axis		
Face	**x**	**y**	**z**
X+: 1	—	π	π
Y+: 2	—	—	$-\frac{\pi}{2}$
Z+: 3	—	$\frac{\pi}{2}$	—
X-: 4	—	0	0
Y-: 5	—	—	$\frac{\pi}{2}$
Z-: 6	—	$-\frac{\pi}{2}$	—

of the DC-DC conversion system that regulates battery power, and η_r is the scatterometer power amplifier efficiency.

The average power consumed by a satellite bus with n subsystems is

$$\overline{P_b} = \frac{1}{\eta_{DC}} \sum_{i=1}^{n} m_i P_i D_i \ , \tag{5.99}$$

where m_i, P_i, and D_i are the redundancy factor, power consumption, and on/off duty cycle of subsystem i. For the scatterometer, I consider the power consumption of the computation (cpu), communications (com), control (ctl), and heating (h) subsystems, so the average power consumed by the satellite bus is

$$\overline{P_b} = \frac{1}{\eta_{DC}} (m_{cpu} P_{cpu} D_{cpu} + m_{com} P_{com} D_{com} + m_{ctl} P_{ctl} D_{ctl} + m_h P_h D_h) \ . \tag{5.100}$$

where $D_{com}(\cdot)$ is the communications duty cycle.

For a communications system that periodically transmits system status telemetry in a beacon and historical telemetry during downlink passes, the communications duty cycle,

$D_{com}(\cdot)$ is

$$D_{com} = D_l + D_b \ . \tag{5.101}$$

where D_l is the downlink duty cycle and D_b is the beacon duty cycle.

The downlink duty cycle is

$$D_l = \frac{R_i + R_t}{R_c} \ . \tag{5.102}$$

where $R_i(\cdot)$ is the instrument data collection rate, $R_t(\cdot)$ is the satellite telemetry collection rate, and R_c is the communications bitrate.

The beacon duty cycle is

$$D_b = \frac{\tau_b}{T_b} \ . \tag{5.103}$$

where $\tau_b(\cdot)$ is the beacon duration, and T_b is the beacon repeat period.

The instrument data collection rate is

$$R_i = \boldsymbol{F} S_c U R_m \ , \tag{5.104}$$

where $\boldsymbol{F}$ is the number of scatterometer measurement flavors, U is the instrument uptime, $R_m(\cdot)$ is the measurement collection rate, and S_c is the measurement data size including all calibration data.

The measurement collection rate

$$R_m = \frac{W_s v_g}{A_c} \ , \tag{5.105}$$

where $W_s(\cdot)$ is the swath width, $v_g(\cdot)$ is the satellite speed projected on the ground, and $A_c(\cdot)$ is the measurement cell area.

The satellite telemetry collection rate is

$$R_t = \frac{S_b}{T_t} \ , \tag{5.106}$$

where S_b is the beacon or telemetry packet data size and T_t is the telemetry sampling period.

The beacon duration is

$$\tau_b = \frac{S_b}{R_c} \ , \tag{5.107}$$

where S_b is the beacon data size and R_c is the communications bitrate.

5.5 Post-umbra Battery Charge

Assuming the batteries are fully charged when the satellite enters the umbra, the post-umbra battery charge, $\boldsymbol{B}$, is the percentage of the battery capacity remaining after the satellite has passed through the umbra,

$$\boldsymbol{B} = \frac{E_c - (\overline{P_s} + \overline{P_b})T_s F_u}{E_c} \ , \tag{5.108}$$

where $E_c(\cdot)$ is the battery system's energy capacity, $\overline{P_s}(\cdot)$ and $\overline{P_b}(\cdot)$ are the average power consumption of the scatterometer and the bus, $T_s(\cdot)$ is the satellite orbital period, and $F_u(h)$ is the fraction of the orbit spent in umbra.

The battery system energy capacity is

$$E_c = I_c \overline{V_b} \ , \tag{5.109}$$

where I_c is the current capacity in A-s and $\overline{V_b}$ is the average voltage of the batteries.

5.6 Instantaneous Battery Usage

The instantaneous battery usage, $\boldsymbol{U_B}$, is the fraction of the power that the batteries are capable of delivering that is used by the satellite in a given moment,

$$\boldsymbol{U_B} = \frac{P_b + P_s}{P_{max}} \ , \tag{5.110}$$

where $P_b(\cdot)$ is the peak bus power consumption, $P_s(\cdot)$ is the peak scatterometer power consumption, and $P_{max}(\cdot)$ is the maximum load that the battery can support.

The maximum load that the battery can support is

$$P_{max} = E_c F_L \overline{V_b} \ , \tag{5.111}$$

where E_c is the battery system's energy capacity, F_L is the battery load factor, and $\overline{V_b}$ is the average battery voltage.

5.7 Temperature Extremes

The approach to spacecraft thermal modeling in this section is derived from the approach used by Czernik [45] and Keesee [43]. To find the temperature extrema that the satellite may encounter, I model an approximate scenario consisting of static orbital positions in which the satellite reaches steady state and all satellite surfaces come into thermal equilibrium.

The energy balance of the steady state system is

$$q_{net} = q_{in} - q_{out} = 0 \ , \tag{5.112}$$

where q_{in} is the heat entering the satellite, which includes heat generated by the scatterometer and absorbed from the solar radiation, solar reflection off the Earth, and Earth thermal radiation. q_{out} is energy dissipated to deep space.

Satellite temperatures vary over the course of the orbit. To find the range of temperatures, I apply a weighted average of the minimum equilibrium temperature, occurring in a cold orbit position in umbra, and the maximum equilibrium temperature, occurring in a hot orbit position in sunlight. This yields

$$\begin{aligned} \boldsymbol{T^-} &= F_u^+ T_{eq}^- + (1 - F_u^+) T_{eq}^+ \\ \boldsymbol{T^+} &= F_u^- T_{eq}^- + (1 - F_u^-) T_{eq}^+ \ , \end{aligned} \tag{5.113}$$

where $F_u(h)$ is the umbra fraction, which is used to weight the average according to the time spent in umbra, and T_{eq} is the equilibrium temperature.

Heat Dissipation

Approximating the apparent temperature of deep space as 0 K, the energy dissipated to deep space is

$$q_{out} = \sigma_b A_\epsilon T^4 \ , \tag{5.114}$$

where σ_b is the Stefan-Boltzmann constant, $A_\epsilon(\cdot)$, is the emissive area of the satellite, and T is the surface temperature, assumed to be equal for all surfaces.

The total emissive area of a satellite is the sum of the emissive areas of its individual faces. I model the satellite as having six faces. For a six-sided satellite, the total emissive area is

$$A_\epsilon = \sum_{i=1}^{6} A_i \Big[\epsilon_{s,i} C_{s,i} + \epsilon_{c,i} (1 - C_{s,i}) \Big] \ , \tag{5.115}$$

where $\epsilon_{s,i}$, $\epsilon_{c,i}$, A_i, and $C_{s,i}$ are the solar cell emissivity, coating emissivity, surface area, and solar cell coverage of the i^{th} surface.

Minimum Equilibrium Temperature

The theoretical equilibrium scenario with the minimum temperature, T_{eq}^- occurs with the satellite stationary in umbra. The heat entering the system is

$$q_{in} = q_E + q_s + q_b + D_h P_h \ , \tag{5.116}$$

where $q_E(\cdot)$ is the average heat radiated from Earth to the satellite, $q_s(\cdot)$ is the average waste heat generated by the scatterometer, D_h is the heater duty cycle, and P_h is the heater power.

Substituting Eq. 5.114 and Eq. 5.116 into Eq. 5.112 yields the minimum equilibrium temperature is

$$T_{eq}^- = \sqrt[4]{\frac{q_E + q_s + q_b + D_h P_h}{\sigma_b A_\epsilon}} \ , \tag{5.117}$$

where q_E is the thermal radiation from the Earth to the spacecraft, q_s is waste heat generated by the scatterometer, D_h is the heater duty cycle, P_h is the heater power, σ_b is the Stefan-Boltzmann constant, and A_ϵ is the effective emission area of the satellite.

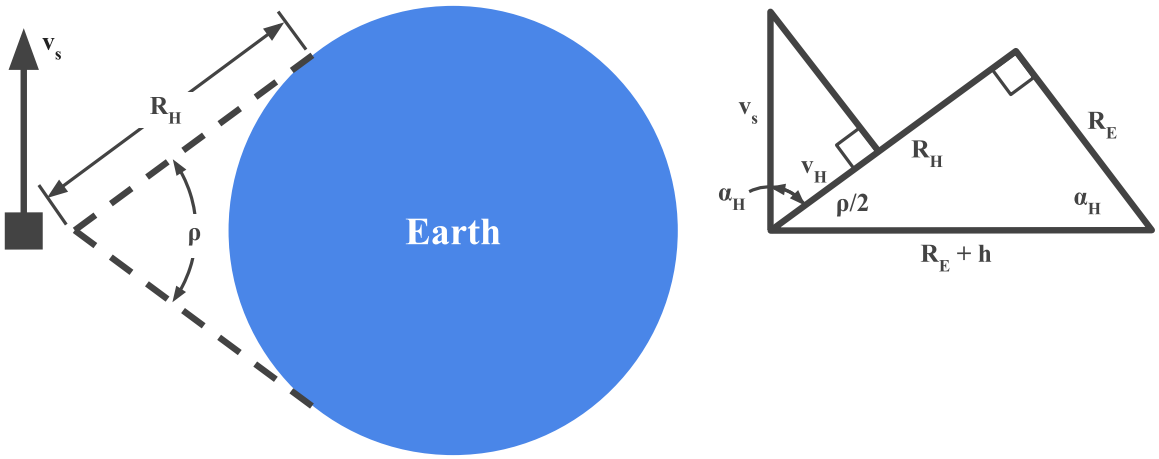

Figure 5.22: (left) Illustration of horizon geometry. ρ is the angular diameter of the Earth from the perspective of the satellite. R_H is the slant range from the satellite to the horizon. v_s is the speed of the satellite. (right) The right triangles used to solve for slant range to the horizon, apparent angular diameter of the Earth, and the radial velocity of the spacecraft with respect to the horizon, v_H. R_E is the Earth radius. h is the altitude, h. α_H is the horizon Earth angle.

The thermal radiation absorbed by the satellite from Earth is

$$q_E = q_I \overline{A_{E,\epsilon}} \sin^2 \rho \tag{5.118}$$

where q_I is the energy flux at Earth's surface, $\overline{A_{E,\epsilon}(\cdot)}$ is the emissive area facing the Earth averaged over the rotation pattern of the satellite, $\rho(\cdot)$ is the angular diameter of the Earth from the perspective of the satellite. While this is expressed as radiation from Earth, often the Earth is colder than the satellite, so the emissivity of the satellite surface is used [43].

As illustrated in Fig. 5.22, the angular diameter of the Earth from the perspective of the satellite is

$$\rho = 2\sin^{-1}\left(\frac{R_E}{R_E + h}\right), \tag{5.119}$$

where R_E is the radius of the Earth and h is the altitude of the satellite.

The emissive area facing the Earth, averaged over the rotation pattern of a six-sided satellite is

$$\overline{A_{E,\epsilon}} = \sum_{i=0}^{6} \zeta_{x,i}\zeta_{y,i}\zeta_{z,i}\Big[\epsilon_s C_{s,i} + \epsilon_c(1 - C_{s,i})\Big] A_i \tag{5.120}$$

where $\zeta_{x,i}(\cdot)$, $\zeta_{y,i}(\cdot)$, and $\zeta_{z,i}(\cdot)$ are the Earth illumination efficiencies of the i^{th} panel due to rotation about the x, y, and z axes, ϵ_s and ϵ_c are the emissivities of the solar cells and the surface where solar cells are absent, $C_{s,i}$ is the solar cell coverage of the i^{th} surface, and A_i is the surface are of the i^{th} face. Emissivity, ϵ, is used instead of absorptivity, α, because the radiant energy is in the infrared spectrum.

The scatterometer waste heat is

$$q_s = \overline{P_s}(1-\eta_{DC})(1-\eta_r) \tag{5.121}$$

where $\overline{P_s}$ is the average scatterometer power, η_{DC} is the efficiency of the DC-DC battery power conversion system, and η_r is the scatterometer power amplifier efficiency.

The bus waste heat is

$$q_b = \overline{P_b}(1-\eta_{DC}) \ , \tag{5.122}$$

where $\overline{P_b}$ is the average bus power and η_{DC} is the power system efficiency.

Maximum Equilibrium Temperature

The theoretical equilibrium scenario with the maximum temperature, T_{eq}^{+} occurs with the satellite stationary between the Earth and the sun. Heat entering the system in this case is

$$q_{in} = q_S + q_a + q_E + q_s + q_b, \tag{5.123}$$

where $q_S(\cdot)$ is the heat absorbed from the sun, $q_a(\cdot)$ is solar radiation reflected off the Earth, $q_E(\cdot)$ is Earth thermal radiation, q_s is waste heat generated by the scatterometer, and q_b is waste heat from the bus.

Substituting Eq. 5.114 and Eq. 5.123 into Eq. 5.112 yields the maximum equilibrium temperature

$$T_{eq}^{+} = \sqrt[4]{\frac{q_S + q_a + q_E + q_s + q_b}{\sigma_b A_\epsilon}} \ , \tag{5.124}$$

where q_S is heat absorbed from the Sun, q_a is solar radiation reflected off the Earth, q_E is the thermal radiation from the Earth to the spacecraft, q_s is waste heat generated by the

scatterometer, q_b is waste heat from the bus, σ_b is the Stefan-Boltzmann constant, and A_ϵ is the effective area of the satellite that dissipates heat to deep space.

Solar radiation absorbed by the satellite is

$$q_S = G_S \overline{A_{S,\alpha}} \ , \tag{5.125}$$

where G_S is the solar irradiance in Earth orbit and $\overline{A_{S\alpha}(\cdot)}$ is the absorptive area of the satellite averaged across its rotation pattern,

$$\overline{A_{S,\alpha}} = \sum_{i=1}^{6} \eta_{x,i}(0)\eta_{y,i}(0)\eta_{z,i}(0)\Big[(\alpha_S - \eta_S)C_{s,i} + \alpha_c(1-C_{s,i})\Big]A_i \ , \tag{5.126}$$

where $\eta_{x,i}$, $\eta_{y,i}$, and $\eta_{z,i}$ are the solar illumination efficiencies of the i^{th} panel due to rotation about the x, y, and z axes.

The solar radiation reflected off the Earth and absorbed by the satellite, given by Keesee [43], is

$$q_a = G_S a \overline{A_{E,\alpha}} \sin^2\rho(0.664 + 0.521\rho + 0.203\rho^2) \ , \tag{5.127}$$

where G_S is the solar irradiance in Earth orbit, a is the albedo of the Earth, $\overline{A_{E,\alpha}}$ is the absorptive area facing the Earth averaged over the rotation pattern of the satellite, and ρ is the angular diameter of the Earth from the perspective of the satellite.

The absorptive area facing the Earth, averaged over the rotation pattern of a six-sided satellite is

$$\overline{A_{E,\alpha}} = \sum_{i=0}^{6} \zeta_{x,i}\zeta_{y,i}\zeta_{z,i}\Big[(\alpha_S - \eta_S)C_{s,i} + \alpha_c(1-C_{s,i})\Big]A_i \tag{5.128}$$

where $\zeta_{x,i}(\cdot)$, $\zeta_{y,i}(\cdot)$, and $\zeta_{z,i}(\cdot)$ are the Earth-illumination efficiencies of the i^{th} panel due to rotation about the x, y, and z axes, α_S is the absorptivity of the solar cells, α_c is the absorptivity of the surface where solar cells are absent, η_S is the solar cell efficiency, $C_{s,i}$ is the solar cell coverage of the i^{th} surface, and A_i is the surface are of the i^{th} face.

5.8 Downlink Capacity Usage

Communications system performance can be measured using the fraction of downlink capacity used in communicating all mission data to ground. As such a satellite that has more downlink capacity than it needs would have a usage less than one and a satellite that generates more data than it can downlink has a usage greater than one. The downlink capacity utilization is

$$\boldsymbol{U_C} = \frac{D_{com}}{D_{gl}} \ , \tag{5.129}$$

where $D_{gl}(\cdot)$ is the downlink availability duty cycle and $D_{com}(\cdot)$ is the communications duty cycle required to downlink the data collected.

The downlink availability duty cycle is the percentage of time that ground stations are available,

$$D_{gl} = N_g D_g \ , \tag{5.130}$$

where N_g is the number of ground stations and $D_g(\cdot)$ is the average ground station duty cycle.

The average ground station duty cycle is the fraction of time that the average ground station is both available and visible to the satellite,

$$D_g = \frac{T_l}{T_p} \ , \tag{5.131}$$

where T_l is the downlink session duration and T_p is the time between passes over a given ground station.

5.9 Data Storage Usage

The data storage usage is the fraction of data storage capacity required to store data collected between passes,

$$\boldsymbol{U_D} = \frac{(R_i + R_t)T_{gl}}{S_d} \ , \tag{5.132}$$

where S_d is the data storage capacity, R_i is the scatterometer data collection rate, R_t is the satellite telemetry collection rate, and $T_{gl}(\cdot)$ is the time between downlink sessions. This assumes the downlink capacity usage, $\boldsymbol{U_C}$, is less than one. Data storage usage, $\boldsymbol{U_D}$, diverges if $\boldsymbol{U_C}$ is greater than one.

The average time between downlink sessions is

$$T_{gl} = \frac{T_p}{N_g} \ , \tag{5.133}$$

where T_p is the time between passes over a given ground station and N_g is the total number of ground stations.

5.10 Cost

The total cost of the scatterometer system is the cost of manufacturing and launching all the satellites in the system,

$$\boldsymbol{C} = N_s(C_s + C_L) \ , \tag{5.134}$$

where $N_s(\cdot)$ is the total number of satellites in the system, C_s is the cost of a single satellite, assuming each satellite is identical, and $C_L(\cdot)$ is the cost of launching a single satellite.

The total number of satellites is the product of the number of orbits and the multiples of each satellite in those orbits. The total is

$$N_s = N_o M_{sc} M_{ss} M_{sh} M_{sf} \ . \tag{5.135}$$

where N_o is the number of orbital planes, each with an identical grouping of $M_{sc}M_{ss}M_{sh}M_{sf}$ satellites, where M_{sc} is the multiple of independent, complementary satellites, M_{ss} is the multiple of independent, supplementary satellites, M_{sh} is the multiple of half-duplex scatterometers, and M_{sf} is the multiple of full-duplex scatterometers. Satellite and front-end multiples, as well as the number of orbital planes, are defined in detail in Chapter 4 and their impacts to scatterometer system performance are summarized in Section 5.11.

CubeSat pricing is used as an estimate of the cost of launching a single satellite, which is conservative since the mass cost ($/kg) of CubeSat launch is higher than that of larger satellites. Thus, the cost of a satellite with N_U CubeSat units is

$$C_L = N_U C_U \ , \tag{5.136}$$

where C_U is the mass cost of CubeSat launch, a market constant.

5.11 Summary

The preceding sections present a full-system, parametric extrema model for satellite scatterometers designed for measuring wind vectors over the surface of the ocean. To summarize this extensive model, this section includes several tables with all parameters discussed in the text. The performance metrics of this model are summarized in Table 5.4. The design parameters are summarized in Table 5.5. The intermediate parameters are summarized in Table 5.6. Finally, the performance tradeoffs of multiple front-ends, satellites, and orbital planes are summarized in Table 5.7.

Table 5.4: Performance metrics for satellite wind scatterometers.

Performance Metric	**Symbol**	**Equation**
Normalized standard deviation*†	$\boldsymbol{K_p}$	Eq. 5.1
Incidence angle†	$\boldsymbol{\Theta}$	Eq. 5.11
Wavelength*†	$\boldsymbol{\lambda}$	Eq. 5.5
Polarization*	$\boldsymbol{pol}$	N/A
Quantity of information-diverse looks*	$\boldsymbol{F}$	Eq. 5.58
Spatial resolution	$\boldsymbol{r}$	Eq. 5.63
Revisit period	$\boldsymbol{T_r}$	Eq. 5.64
Orbital average power usage	$\boldsymbol{U_P}$	Eq. 5.74
Post-umbra battery charge	$\boldsymbol{B}$	Eq. 5.108
Peak instantaneous battery usage	$\boldsymbol{U_B}$	Eq. 5.110
Temperature	$\boldsymbol{T}$	Eq. 5.113
Downlink capacity usage	$\boldsymbol{U_C}$	Eq. 5.129
Data storage usage	$\boldsymbol{U_D}$	Eq. 5.132
System cost	$\boldsymbol{C}$	Eq. 5.134

* Proxy for wind measurement accuracy.
† Proxy for wind measurement dynamic range.

Table 5.5: Design parameters for satellite wind scatterometers.

Design Parameter	**Symbol**
Radar Transmit Power	P_t
Radar Transmit Frequency	f
Doppler Compensation Mode	(Case)[1]
Radar Polarization	pol
Radar Receive Bandwidth	B_r
Radar Dwell Time	T_d

[1]Doppler compensation modes include cell, scan, and none.

Table 5.5 – (continued)

Design Parameter		**Symbol**
Radar Pulse Compression Mode		(Case)[2]
Radar Resolution Mode		(Case)[3]
Radar Pulse Length		τ
Radar Burst Count		n_b
Radar Duty Cycle		D_r
Radar Coherent Integration Boolean		C_I
Number of Simultaneous Radar Signals		n_{rf}
Radar Noise Factor		F_n
Radar Transmit Loss		L_t
Radar Receive Loss		L_r
Radar Signal Processing Loss		L_{sp}
Radar Loss due to Atmospheric Attenuation		L_a
Spatial Downsampling Factor		F_s
Antenna Multiples	Independent Supplement	M_{fs}
	Half-duplex	M_{fc}
	Full-duplex	M_{fh}
	Independent Complement	M_{ff}
Antenna Length in the n$^{\text{th}}$ Direction		L_n
Antenna Beamwidth Factor in the n$^{\text{th}}$ Direction		α_n
Antenna Efficiency	Transmit	η_t
	Receive	η_r
Antenna Aperture Efficiency	Transmit	$\eta_{a,t}$
	Receive	$\eta_{a,r}$
Antenna Shape Factor		F_a

[2]Radar pulse compression modes include ICW and LFM

[3]Radar resolution modes include range, Doppler, range-Doppler, and footprint.

Table 5.5 – (continued)

Design Parameter		**Symbol**
Look Angle	Elevation	φ
	Azimuth	ψ
	Elevation Determination Error	e_φ
	Azimuth Determination Error	e_ψ
Scan Rate		ω
Uptime		U
Focus Factor		F_F
Precession Boolean		P
Satellite Multiples	Independent Supplement	M_{ss}
	Independent Complement	M_{sc}
	Half-duplex	M_{sh}
	Full-duplex	M_{sf}
Orbit	Altitude	h
	Inclination	I
Charging Downtime		D_{ch}
Dedicated Charging Consecutivity		F_c
Solar Cell Efficiency		η_s
Power System Efficiency		η_{DC}
Scatterometer System Efficiency		η_s
Maximum Power Consumption	Radio	P_r
	Computer	P_c
	Attitude Control	P_m
	Star Tracker	P_{st}
	Heater	P_h

Table 5.5 – (continued)

Design Parameter		**Symbol**
Duty Cycle	Computer	D_c
	Attitude Control	D_m
	Star Tracker	D_{st}
	Heater	D_h
Beacon Size		S_b
Beacon Repeat Period		T_b
Telemetry sampling period		T_t
Ground Station Session Duration		T_l
Ground Station Quantity		N_g
Storage Size of Measurement and Calibration Data		S_c
Communications Bitrate		R_c
Communications Bandwidth		B_c
Data Storage Capacity		S_d
Battery Capacity (A-s)		I_c
Average Battery Voltage		V_b
Battery Load Factor		F_L
Satellite Size (CubeSat Units)		N_U
Thermal Emissivity	Satellite Coating	ϵ_c
	Solar Cells	ϵ_s
Thermal Absorptivity	Satellite Coating	α_c
	Solar Cells	α_s
Satellite Rotation About the u^{th} Axis		ψ_u
Area of the i^{th} Face		A_i
Solar Cell Coverage of the i^{th} Face		$C_{s,i}$
Dedicated solar power generation area		$A_{S,d}$
Satellite cost		C_s

Table 5.6: Intermediate parameters for satellite wind scatterometers.

Intermediate Parameter	**Symbol**	**Equation**
Looks in a single dwell	n_d	Eq. 5.2
Signal-to-noise ratio	S_N	Eq. 5.4
Normalized radar cross section (scatter)	σ_0	Eq. 5.8
Transmit bandwidth	B_t	Eq. 5.6, Eq. 5.7
Pulse time of flight	T_f	Eq. 5.57
Pulse repetition interval	T_τ	Eq. 5.3
Smear loss	L_s	Eq. 5.45
Pulse loss	L_τ	Eq. 5.48
Doppler loss	L_D	Eq. 5.51, Eq. 5.50, Eq. 5.49
Two way Doppler shift	$f_{D,e}$	Eq. 5.52
Radial velocity of the measurement cell	v_c	Eq. 5.53
Doppler bandwidth	B_D	Eq. 5.54
Cell Doppler bandwidth	$B_{D,c}$	Eq. 5.55
Total system loss	L	Eq. 5.44
Edge look angle	φ_{edge}	Eq. 5.12
Look center Earth angle	α	Eq. 5.13
Look edge Earth angle	α_{edge}	Eq. 5.26
Look center incidence angle	φ	Eq. 5.10
Slant range	R_s	Eq. 5.38
Ground range from nadir to measurement cell	R_g	Eq. 5.47
Maximum swath latitude	Ω	Eq. 5.67
Transmit or receive antenna gain	G_t or G_r	Eq. 5.19
Two-way, half-power antenna beamwidth corresponding to the n$^{\text{th}}$ direction	θ_{3n}	Eq. 5.18
Antenna aperture area	A_a	Eq. 5.20

Table 5.6 – (continued)

Intermediate Parameter		**Symbol**	**Equation**
Footprint size	Radial cross-track	a_{rx}	Eq. 5.24, Eq. 5.25, Eq. 5.56
	Radial along-track	a_{ry}	
	Azimuthal cross-track	$a_{\gamma x}$	
	Azimuthal along-track	$a_{\gamma y}$	
	Along-track	a_y	
Spatial resolution	Radial cross-track	a_{rx}	Eq. 5.23, Eq. 5.28, Eq. 5.31
	Radial along-track	a_{ry}	
	Azimuthal cross-track	$a_{\gamma x}$	
	Azimuthal along-track	$a_{\gamma y}$	
	Cross-track cross-track	a_{xx}	
	Cross-track along-track	a_{xy}	
	Along-track cross-track	a_{yx}	
	Along-track along-track	a_{yy}	
Swath width		W_s	Eq. 5.69
Measurement cell area		A_c	Eq. 5.21, Eq. 5.22
Spatial scan rate		K_ω	Eq. 5.60
Scan factor		F_ω	Eq. 5.59
Dwell step		S_d	Eq. 5.46
Linear coverage		C_l	Eq. 5.73
Equatorial coverage		C_e	Eq. 5.68
Daily coverage by a single satellite		C	Eq. 5.65
Satellite orbital speed		v_s	Eq. 5.34
Satellite orbital period		T_s	Eq. 5.62
Satellite speed projected on the ground		v_g	Eq. 5.61
Equatorial orbit step		S_o	Eq. 5.72
Total constellation size		N_s	Eq. 5.135

Table 5.6 – (continued)

Intermediate Parameter		**Symbol**	**Equation**
Orbit beta angle		β	Eq. 5.90
Umbra cutoff beta angle		β^*	Eq. 5.91
umbra fraction		F_u	Eq. 5.89
Earth angular diameter from satellite		ρ	Eq. 5.119
Instrument data collection rate		R_i	Eq. 5.104
Telemetry data collection rate		R_t	Eq. 5.106
Downlink duty cycle		D_l	Eq. 5.102
Beacon duty cycle		D_b	Eq. 5.103
Beacon duration		τ_b	Eq. 5.107
Communications duty cycle		D_{com}	Eq. 5.101
Downlink availability duty cycle		D_{gl}	Eq. 5.130
Time between downlink passes		T_{gl}	Eq. 5.133
Average ground station duty cycle		D_g	Eq. 5.131
Scatterometer maximum power consumption		P_s	Eq. 5.98
Bus maximum power consumption		P_b	Eq. 5.99, Eq. 5.100
Maximum battery load		P_{max}	Eq. 5.111
Average scatterometer power consumption		$\overline{P_s}$	Eq. 5.97
Average bus power consumption		$\overline{P_b}$	Eq. 5.100
Battery saturation during dedicated charging		B_s	Eq. 5.81
Dedicated charging instantaneous power		$P_{S,d}$	Eq. 5.78
Orbital average power generation	Operational solar	$\overline{P_S}$	Eq. 5.76
	Dedicated solar	$\overline{P_{S,d}}$	Eq. 5.77
	Earth reflected	$\overline{P_E}$	Eq. 5.79
	Saturation Waste	$\overline{P_w}$	Eq. 5.80
	Total	$\overline{P_g}$	Eq. 5.75
Launch cost		C_L	Eq. 5.136

Table 5.6 – (continued)

Intermediate Parameter		**Symbol**	**Equation**
Satellite equilibrium temperature		T_{eq}	Eq. 5.117, Eq. 5.124
Added Heat	Solar	$\overline{q_S}$	Eq. 5.125
	Earth thermal	$\overline{q_E}$	Eq. 5.118
	Earth reflected	$\overline{q_a}$	Eq. 5.127
	Scatterometer waste	$\overline{q_s}$	Eq. 5.121
	Bus waste	$\overline{q_b}$	Eq. 5.122
Satellite emissive area		A_ϵ	Eq. 5.115
Operational solar power generation area		A_S	Eq. 5.82
Average sun-facing illumination efficiency of the i^{th} face about the u^{th} axis		$\eta_{u,i}$	Eq. 5.85, Eq. 5.86
Average Earth illumination efficiency of the i^{th} face about the u^{th} axis		$\zeta_{u,i}$	Eq. 5.94
Average Earth-facing solar generating area		A_E	Eq. 5.92
Average Sun-facing thermal absorptive area		$A_{S,\alpha}$	Eq. 5.126
Average Earth-facing thermal emissive area		$A_{E,\epsilon}$	Eq. 5.120
Average Earth-facing thermal absorptive area		$A_{E,\alpha}$	Eq. 5.128
Solar illumination range for the i^{th} face about the u^{th} axis		$\psi_{S,u,i}$	Eq. 5.87
Earth illumination range for the i^{th} face about the u^{th} axis		$\psi_{E,u,i}$	Eq. 5.95
Sun-facing illumination offset of the i^{th} face about the u^{th} axis		$\epsilon_{u,i}$	Table 5.2
Earth-facing illumination offset of the i^{th} face about the u^{th} axis		$\xi_{u,i}$	Table 5.3

Table 5.7: Applications of co-operative satellites and front-ends. The $\propto$ symbol is used where the performance metric is proportional to the cooperative multiple. The $\sim$ multiple is used where the performance metric is a more complex function of the cooperative multiple, which approximately changes the performance metric as indicated.

	Independent		
	Supplement	**Complement**	
Satellites	$\boldsymbol{F} \propto M_{ss}{}^{*}$	$\boldsymbol{K_{pp}} \propto M_{sc}$	
front-ends	$\boldsymbol{F} \propto M_{fs}{}^{*}$	$\boldsymbol{C}, \boldsymbol{F} \propto M_{fc}{}^{**}$	
Orbits‡	N/A	$\boldsymbol{T_r} \propto N_o$	
	Interdependent		
	Simplex	**Half-duplex**	**Full-duplex**
Satellites	$\boldsymbol{F} \propto M_{sh}{}^{*}$	$\boldsymbol{F} \propto M_{sh}{}^{*}$, $\boldsymbol{K} \sim M_{sh}$	$\boldsymbol{F} \sim M_{sf}^2/2^{*}$
front-ends	$\boldsymbol{F} \propto M_{fh}{}^{\dagger}$	$\boldsymbol{F} \propto M_{fh}{}^{\dagger}$, $\boldsymbol{K} \sim M_{fh}$	$\boldsymbol{F} \sim M_{ff}^2/2^{\dagger}$
Orbits‡	N/A	N/A	

* Additional $\boldsymbol{F}$ achieved through look or signal diversity.
** M_{fc} contributes to $\boldsymbol{F}$ only if scanning.
† Additional $\boldsymbol{F}$ achieved through signal diversity.
‡ Each orbit is assumed to have a grouping of $M_{sc}M_{ss}M_{sh}M_{sf}$ satellites in it.

Chapter 6

Validation of the Model Using Heritage Designs

The model presented in Chapter 5 is so extensive that evaluating its accuracy poses a challenge. The derivation is as detailed as possible, but any errors in the derivation can be obscured by this complexity. This is even more true for the implementation of the model, which required manual entry of over 200 parameters for each of the many designs explored and manual coding of more than 800 equations.

Validation of the model involves a paradox: the model is designed to speed up the process of exploring the design space, but it can only reliably be validated by simulating and building scatterometer point designs and comparing their performance to the model predictions. Further, model validation is only truly reliable in the region of the point design. Thus, the parametric extrema model should be seen as a screening tool, and further simulation and production should follow for the most promising designs.

While validation of the model across the entire design space is impractical. Point validation still improves model reliability. Several current and past scatterometers were used to validate the model, including NSCAT, ASCAT, QuikSCAT, and RFSCAT. Design parameters were collected from the literature and used in the model to predict the performance of these heritage scatterometer systems. Table 6.1 compares the predicted performance to actual performance reported in the literature. This approach helped reveal several limitations in the model that were improved upon during model development.

After refinement of the model, most of the predicted ranges encompass the reported values. This is suitable for the early stage of the process in which full-system, parametric, extrema modeling is expected to occur.

The design parameters used in these point design validations are presented in Appendix D. Collecting these design parameters proved to be very challenging. Parametrically expressing the entire design required a number of design parameters to be included that are not commonly reported in the literature. Where available, the parameters found in the literature were relied upon. Where parameters were unavailable, assumed values were chosen so that they combined with available parameters to produce intermediate parameter predictions that matched values available in the literature. This was especially true of the design parameters that contribute to antenna gain, which is often reported while its driving parameters are not.

In some cases, neither design parameters nor intermediate parameters were available. Often scatterometers trade spatial resolution for accuracy using larger Doppler bins and spatial averaging. Without a parameterization for this tradeoff, the model predicts the minimum possible spatial resolution, which can be excessively fine (as in synthetic aperture radar). This tradeoff is not typically reported in the literature, so the spatial downsampling and Doppler binning factors were adjusted until they aligned the normalized standard deviation and spatial resolution with the literature.

The scatterometer literature seldom reports the design parameters of the satellite bus that hosts the scatterometer instrument, so the bus portions of the model were not validated. Future work could adapt techniques from software unit testing to evaluate model reliability in a more comprehensive manner.

Table 6.1: Heritage point design comparison between performance predicted by the model and performance reported in the literature.

Performance Metric		**Predicted Values**	**Actual Values**
NSCAT	Normalized Standard Deviation	0.2 - 2	0.1 - 4.0 [46]
	Look Edge Incidence Angle	18°- 58°	18°- 59° [47]
	Wavelength	2.14 cm	2.14 cm [48]
	Polarization	H/V	H/V [48]
	Flavors	4	4 [48]
	Spatial Resolution	16 km - 45 km	25 km [48]
	Daily Global Coverage	52%	70% [49]
ASCAT	Normalized Standard Deviation	0.015 - 5.7	0.03 - 0.1 [50]
	Look Edge Incidence Angle	28°- 60°	25°- 65° [50]
	Wavelength	5.7 cm	5.7 cm [50]
	Polarization	V	V [50]
	Flavors	3	3 [50]
	Spatial Resolution	25 km	25 km [50]
	Daily Global Coverage	68%-69%	66% [50]
QuikSCAT	Normalized Standard Deviation	0.057 - 4	0.010 - 0.100 [51]
	Look Edge Incidence Angle	45°- 54°	46°- 54° [52]
	Wavelength	2.24 cm	2.24 cm [51]
	Polarization	H/V	H/V [51]
	Flavors	4 - 8	2 - 4
	Spatial Resolution	25 km	12.5 km - 25 km [51]
	Daily Global Coverage	65%	90% [51]
RFSCAT	Normalized Standard Deviation	0.02 - 0.63	0.08 - 0.20 [53]
	Look Edge Incidence Angle	27°- 52°	26°- 51° [53]
	Wavelength	2.26 cm	2.26 cm [53]
	Polarization	H/V	H/V [53]
	Flavors	1	upto 18 [54]
	Spatial Resolution	17 km - 23 km	12.5 km - 25 km [53]
	Daily Global Coverage	44%	90% [55]

Chapter 7

Concepts for New Satellite Wind Scatterometer Systems

The goal of the model developed in Chapter 5 is to make it easier to search for new scatterometer system designs with potential to achieve high performance at low cost by exploiting new technologies. I used the model to explore many scatterometer system designs. This chapter presents two of those designs which lie in areas of the design space not previously explored, specifically in areas of satellite cooperation (see Chapter 4). Early versions of these concepts were presented in [34]. Additional concepts are presented in [56], [57].

Section 7.1 describes several technological and marketplace advances that expand the design space, making cooperative scatterometer systems possible. The concepts presented in this chapter have the potential to significantly improve scatterometer performance on a variety of measures. For each concept, I briefly describe an example design, including key subsystems and the volume they consume, expressed in CubeSat units (U). Note that CubeSat units measure 10 cm on each side and weigh 1.33 kg.

7.1 Expansion of the Scatterometer Design Space

Technology advances enable designs to be implemented with parameters that were previously outside the accessible design range. Compared to the 1970-1990 timeframe when the

traditional approaches to satellite wind scatterometry were developed, electronics are now smaller, larger structures can now be deployed, and launches can now be shared by multiple small satellites. These advances have expanded the scatterometer design space, primarily by making it affordable to deploy multiple satellites in multiple orbital planes to observe the planet more frequently.

Mobile computing has driven mass production of miniaturized, low-power electrical components. This expands the accessible range of transmit power as it leads electronics to consume less of the power budget and leaves more room for power systems. Similar trends have expanded the range of possible bandwidths and wavelengths, but the complications of frequency allocations and the difficulty of developing the GMF at new frequencies make these advances beyond the scope of this work.

Advanced deployable mechanisms, including compliant ([58], [59]) and origami-adapted [60] mechanisms, allow larger solar arrays and antennas to be stowed in a smaller volume for later deployment. This expands the accessible range of antenna length and transmit power.

These advances increase satellite capability-to-volume ratio. Satellites can now be more capable for a given size or smaller for a given capability. This tradeoff favors smaller satellites. Satellite miniaturization is a compounding process, so capability-to-volume ratio may increase with miniaturization. For example, a smaller processing system requires less power and enables a smaller power system. This in turn allows for a smaller attitude control system, which consumes less power, etc. Smaller satellites cost less to build and less to launch. Many can be launched for the price of a large satellite.

With many small satellites, the responsibilities of a large, monolithic satellite can be disaggregated into a "faction" of dissimilar, cooperative satellites (see Chapter 4). This creates an opportunity for redundant satellites instead of redundant components. Redundant components have unique interfaces, roughly equal to $m^2n^2/2$, where m is the number of redundant multiples of n components in the system. For example, a secondary power system must interface with each powered subsystem, be mounted, and be factored into navigation and control models. Every unique interface brings with it added design and assembly work with added opportunities for design and assembly faults. For redundant satellites without redundant components, $m = 1$. This reduces unique interfaces to $n^2/2$, so redundant satellites

have fewer interfaces by a factor of m^2. Redundant satellites may have better reliability with less complexity than a single satellite with redundant components. This further reduces cost, allowing more satellites to be deployed under the same budget.

Satellite costs can also be reduced by subjecting components and assemblies to only those ground-based environmental tests which pass the expected value criterion: $\Delta\rho_e(C_S + C_L) > C_T$, where $\Delta\rho_e$ is the expected reliability increase, and C_S, C_L, and C_T are the costs of the satellite, launch, and ground test, respectively. In practice, this is difficult to calculate a priori, and must be estimated intuitively. If scatterometers are operated in very low orbits, which have relatively mild temperatures, mild radiation, and brief orbital life, some space environmental testing can be traded for on-orbit testing.

For a constellation, these approaches allow for new satellite designs to be tested in space sooner and for lessons from space to be iterated upon more frequently. More frequent deployments enable rapid, low-cost improvement of small satellite constellations [30], [61].

7.2 Interdependent Simplex Scatterometer Faction

Factions (described in Chapter 4) can leverage compounding size reduction by separating the functions of a single scatterometer into modular segments. This is the motivation behind the half-duplex scatterometer faction, illustrated in Fig. 7.1. This approach might use a 3U CubeSat transceiver and downlink module to illuminate the surface and two 1.5U CubeSat receiver modules with synchronized timing to observe the scattered signal from two additional azimuth angles. This architecture achieves the necessary flavors with a single antenna and no moving parts, but requires formation flying. Multiple factions can be combined into a larger constellation to provide global coverage and increased revisit rate.

For the 1.5U receiver modules, the receiver and bus electronics can be tightly packed into 0.5U. These may include a 10 W-hr LiPo power system, magnetorquers, and integrated command and data handling (CDH), tasking telemetry and control (TTC), GPS-receiver for clock synchronization, and scatterometer receiver electronics. The remaining 1U is expected to be sufficient to stow an accordion-folded 1 x 0.1 m patch-array antenna.

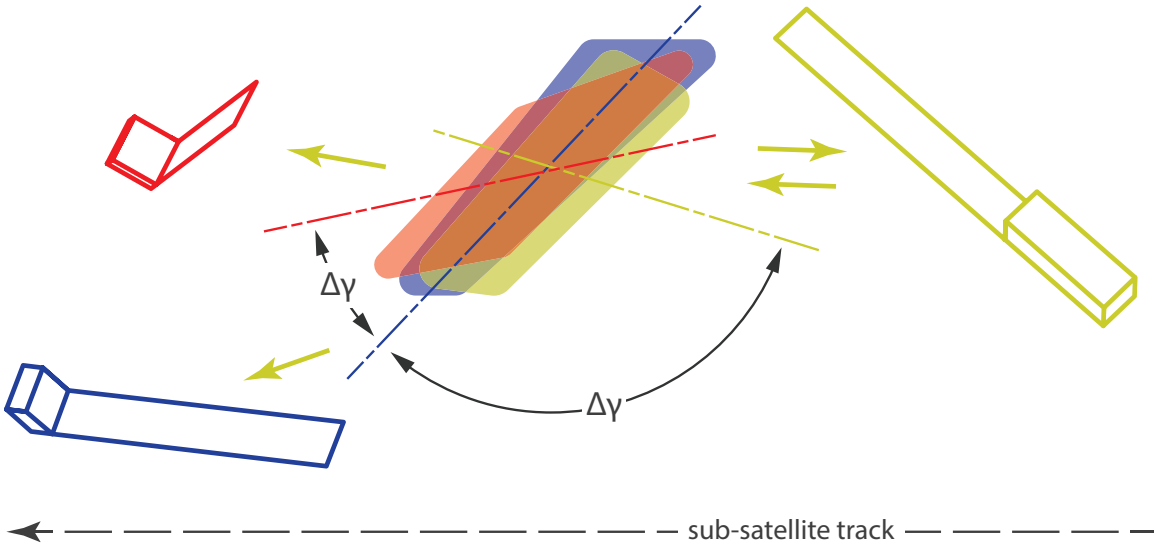

Figure 7.1: Interdependent, simplex scatterometer faction, consisting of a 3U Tx/Rx CubeSat and two, 1.5U Rx CubeSats, each with 1-meter, fan-beam antennas. Together, the faction obtains the required three azimuth-diverse looks. Arrows illustrate unit transmit and receive functionality. $\Delta\gamma$ illustrates the azimuth diversity of the look directions. Ground footprints displacement is exaggerated for clarity.

For the 3U transceiver module, 0.75U is allocated for a flexible, deployable solar array, such as that used for the Lightweight, Integrated Solar Array and Antenna (LISA-T) [62], to provide 150W for radar and bus operation. Another 0.75U is allocated to the bus, the electronics for the radar transmitter, and additional LiPo power storage for eclipsed radar operations.

7.3 Interdependent, Full-duplex Scatterometer Cluster

Full-duplex scatterometer cooperation allows each instrument to take advantage of the signal scattered by its companion(s) in addition to its own. A full-duplex scatterometer approach, illustrated in Fig. 7.2, might include two identical scatterometers with synchronized timing. Pointing at the same region on the surface, they transmit in tandem, then receive in tandem. Assuming the signals are separable, each receives and demodulates its own signal as well as the signal of the other sensor. This pairing produces two flavors for each instrument: one

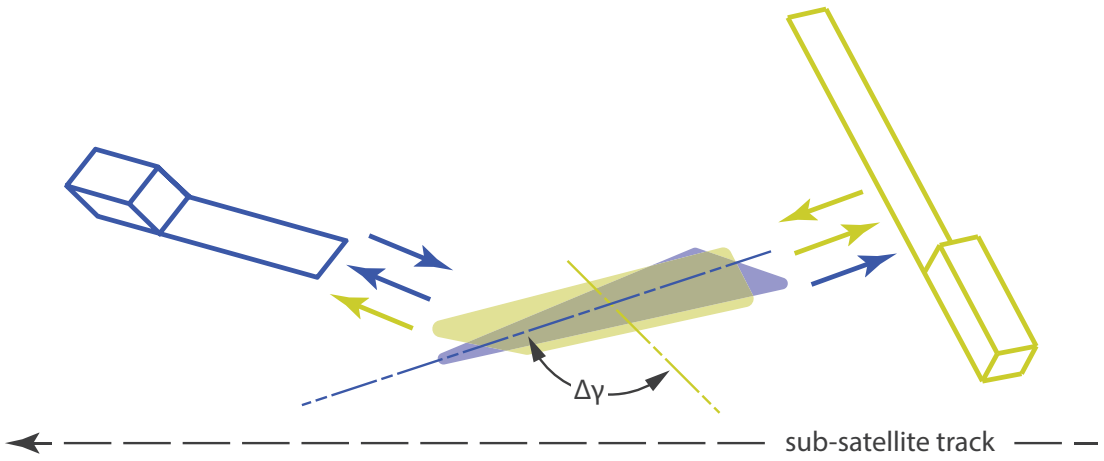

Figure 7.2: Interdependent, full-duplex scatterometer pair of two 3U Tx/Rx CubeSats with 2-meter, fan-beam antennas, providing three to four azimuth-diverse looks (including backscatter and forward scatter). Arrows illustrate unit transmit and receive functionality. $\Delta\gamma$ illustrates the azimuth diversity of the look directions. Ground footprints displacement is exaggerated for clarity.

reverse scattering measurement for each (σ^0_{11}, σ^0_{22}) and one forward scattering measurement for each (σ^0_{12}, σ^0_{21}). $\sigma^0_{12} = \sigma^0_{21}$, so this configuration produces three flavors.

The subsystem breakdown is similar to that of the half-duplex architecture 3U transceiver module, described in Section 7.2, but in this case, a two-meter antenna is used to improve the spatial resolution. Half of the antenna is accordion-folded into 1U of the satellite while the other half is wrapped around the satellite. The wrap around segment is unfurled first with the accordion-folded segment being released afterward.

7.4 Estimated Performance Comparisons

The performance of these architectures predicted by the model is summarized in Table 7.1. The design parameters used in their estimation is provided in Appendix D. See heritage point design performance given in Table 6.1 for comparison.

To achieve revisit comparable to heritage scatterometers (26 hours), eight orbital planes are used, each with one faction/cluster. This comes to 24 satellites for the half-duplex case and 16 for the full-duplex case. However, since the total CubeSat faction/cluster volume

is 6U in both cases, the total volume comes out to 108U for both. Estimated performance of this constellation is similar to that of a single heritage scatterometer.

To achieve hourly revisit, a larger constellation of 200 orbital planes, each with one faction/cluster, can be employed. This requires 600 satellites for the half-duplex case and 400 for the full-duplex case. Both cases total 1200U, which translates to roughly 1600 kg of weight, compared to a weight of 870 kg for QuikSCAT [63]. Precedent has been established for satellite constellations with hundreds of satellites: Planet, Inc. recently constructed, launched, and commissioned roughly 300 satellites [30]. A constellation of scatterometers could give insight into near-hourly variations in wind, enabling researchers and forecasters to observe, model, and track the subdiurnal, mesoscale atmospheric processes that are not currently observable.

These constellation architectures have the potential to not only increase revisit rate, but to decrease cost as well. Based on rough, order-of-magnitude cost investigation, a small constellation with performance equivalent to the traditional scatterometers could be built and launched for an order of magnitude less cost, on the order of O($10M) for a small CubeSat constellation versus O($100M) for a traditional scatterometer. A large constellation, on the order of O($100M), could be equivalent in cost to a traditional scatterometer, with an order of magnitude more frequent revisit.

Table 7.1: Estimated performance of sample designs for CubeSat scatterometer constellations.

Constellation Parameters	**Simplex**	**Full-duplex**
Number of Orbital Planes	8 | 200	8 | 200
Factions/Clusters per Orbital Plane	1	1
Satellites per Faction/Cluster	3	2
Total Satellites	24 | 600	16 | 400
Total CubeSat Units	108U | 1200U	108U | 1200U
Total System Mass	1600 kg	1600 kg
Performance Metric	**Simplex**	**Full-duplex**
Normalized Standard Deviation	0.005—2.1	0.004—1.2
Flavors	3	3
Spatial Resolution	25 km	25 km
Revisit Period	26 hrs | 1 hr	26 hrs |1 hr
Orbital Average Power Usage	(26%, 100%)	(18%, 100%)
Post-umbra Battery Charge	100%	100%
Instantaneous Battery Usage	(6%, 18%)	(6%, 18%)
Extreme Temperatures	315.0 K	315.0 K
Downlink Capacity Usage	(1.9%, 5.8%)	(1.9%, 5.8%)
Data Storage Capacity Usage	(0.0%, 0.0%)	(0.0%, 0.0%)

Chapter 8

Conclusion

With decades of improvements in the technologies upon which scatterometers are dependent, new system architectures are becoming increasingly feasible, many of which undoubtedly remain undiscovered. This work set out to explore the design space of scatterometry more thoroughly. It employed a new modeling approach designed to streamline design space exploration and discovery of new architectures. This chapter summarizes my work and discusses conclusions. Finally, it suggests potential areas of future work.

8.1 Summary

The design process for complex systems, such as scatterometers, typically involves a large set of fragmented simulations and studies. Each change in the design can require a long time to re-evaluate. To reduce friction in the process of searching for new designs, I developed a novel modeling approach, called full-system parametric extrema modeling. Model construction involves defining parametric relationships for bounds on the performance metrics based on the range of possible design parameter values.

To model satellite scatterometers parametrically, I developed an expanded taxonomy of modes of satellite radar cooperation. This enabled multiple modes of multi-satellite cooperation to be included in the model as multipliers on the relevant equations. The taxonomy is adapted from a morphological analysis of distributed satellites performed by Selva

et al.[29], to which I added several additional modes and labeled them based on distributed architectures used in past satellite missions.

The core of this work is a full-system, parametric extrema model of satellite wind scatterometer systems. The model makes it easier to quickly explore the space of possible scatterometer designs. The model includes aspects of scatterometer measurement performance and satellite bus performance. Some parametric relationships are available in the literature and are adapted for use here. Others are not and are derived in this work.

The model was validated against heritage scatterometers, including NSCAT and SeaWinds on QuikSCAT, ASCAT, and RFSCAT. Design parameters were collected and fed into the model and the resulting performance predictions were compared to performance reported in the literature.

8.2 Conclusions

The scatterometer system model provides insight into the potential of recent technologies to enable affordable constellations of cooperative CubeSat scatterometers for near-hourly measurement of ocean vector winds. I used the model to explore many concepts for cooperative satellite wind scatterometers. I successfully found new architectures for distributed satellite scatterometer systems capable of measuring ocean surface vector winds with more frequent revisit or reduced cost. These new scatterometer concepts use the taxonomy of distributed, cooperative satellites described in this work.

The scatterometer designs found through this work, and designs yet to be found, have the potential to reduce the costs of satellite scatterometry by multiple orders of magnitude. These reductions in cost enable more satellites to be launched in a constellation capable of monitoring ocean vector winds on timescales nearer to real time. Similar reductions may enable scatterometer advances in other aspects of performance, including spatial resolution and accuracy. These improvements will give greater visibility into atmospheric processes and the weather that impacts everyone on Earth.

Many system relationships are too complex to model parametrically, so they typically require more intensive, slower modeling approaches. The parametric extrema modeling

approach developed in this work makes it feasible to parametrically model some complex relationships by providing a maximum bound on performance instead of a specific performance expectation.

The typical complexity of modeling complex systems makes it difficult to (1) maintain them with changing part supply and (2) upgrade them with new technologies. As a result, complex systems, like scatterometers, risk gaps in service and slowed progress. By making redesign and evaluation faster, parametric extrema modeling may facilitate lower-cost maintenance and improvement of infrastructure technologies used in a wide range of activities and endeavors.

8.3 Future Work in Parametric Extrema Modeling

- Future software implementations of the model could integrate the derivations with the calculation results in a way that makes it simpler to understand the workings of any metric of interest.

- Model results were difficult to convert to forms familiar to professionals in the industry. Future work could integrate the model with parametric documentation to automatically detail a given design in common formats based on the calculations of the model. For example, parametric documentation could convert model parameters and metrics into design reports, power and link budgets, and design comparisons. Parametric diagrams would be especially powerful.

- Parametric extrema modelling is still infeasible for some measures of performance, such as wind measurement accuracy and dynamic range. For others, parametric extrema modeling is still too complicated. For example, solar illumination requires 400 parametric equations, where a couple dozen lines of simulation code would do. Future work could integrate simulations which sync with the rest of the design and are automatically rerun when design parameters are updated.

- Optimizing designs using the parametric model required manually stepping through values. Future work could develop approaches for automatically producing tradeoff plots of the variation in each performance metric with select parameters.

- It is tedious to trace equation dependencies to find a parameter responsible for an error. Future work could produce design dependency trees, which could be quickly navigated to determine which parameters should be changed to improve a given performance metric.

- It remains difficult to fully explore the design space of complex systems. Future work could develop an approach for determining the design parameters of greatest significance using Monte Carlo analysis to perform screening experiments. From this, a simplified design space could be developed, which would be easier to explore more broadly.

Near the end of my work, I found a recently-released software tool, called Valispace, that can be used to implement a parametric extrema model and even contains some of the above improvements. Valispace is parametric system modeling software that supports parametric documentation. Valispace also supports automatic refresh of connected simulations which would be useful for implementing a more effective, streamlined version of my model.

8.4 Future Work in the Satellite Wind Scatterometer Model

- The particular polynomial fit for backscatter as a function of incidence angle included in Chapter 5 is only applicable to one frequency band, Ku-band. Additional polynomial fits should be obtained for other geophysical model functions, including those for C-band and L-band, to support trade-offs in operating frequency.

- Calibration uncertainty in the backscatter measurements is important to performance, but it is assumed to be achieved through good design practice and neglected in the model of Chapter 5. Future work could extend the model to account for various key

effects on calibration uncertainty, such as the stability of the radar gain with thermal variation and the errors in pointing and geolocation.

- The revisit period used in Chapter 5 is actually closer to a mean temporal resolution. Temporal resolution can have much wider bounds. For example, CYGNSS had fine temporal resolution along the "chain" (see Chapter 4) and coarse temporal resolution between each pass of the chain [25]. Future iterations of the model should include a performance metric which expresses the full range of temporal resolutions.

- The model includes "Downlink Capacity" among the performance metrics, but uses transmitter bitrate as a design parameter. This makes it difficult to understand the requirements placed on the satellite bus by the radio power, pointing, and communications antenna needed to produce the required bitrate. Future work could integrate a parametric link budget (e.g. [64]).

- Future work could expand the model to the rest of the satellite bus, including attitude determination and control, orbit keeping and variation, and more detailed size, mass, and cost.

- Many modes of cooperation included in the model were not considered in the concepts of Chapter 7. Some modes of cooperation were described in Chapter 4, but not included in the model. And there are yet more concepts for cooperation that could be added to the taxonomy (see gaps in Table 3 of Selva et al.[29]).

- Instruments like scatterometers, such as radiometers, precipitation radars, synthetic aperture radars, and altimeters, could be included in the model to support dual-mode operation.

Bibliography

[1] F. T. Ulaby and D. G. Long, *Microwave Radar and Radiometric Remote Sensing*. University of Michigan Press, 2014.

[2] F. M. Naderi, M. H. Freilich, and D. G. Long, "Spaceborne radar measurement of wind velocity over the ocean-an overview of the NSCAT scatterometer system," *Proceedings of the IEEE*, vol. 79, no. 6, pp. 850–866, 1991. DOI: 10.1109/5.90163.

[3] D. G. Long, "Polar applications of spaceborne scatterometers," *IEEE Journal of Selected Topics in Applied Earth Observations and Remote Sensing*, vol. 10, no. 5, pp. 2307–2320, 2017. DOI: 10.1109/jstars.2016.2629418.

[4] H. Stephen, D. Long, and P. Hardin, "Vegetation study of Amazon using QSCAT in comparison with SASS, ESCAT, and NSCAT," in *Proceedings of the International Geoscience and Remote Sensing Symposium*, vol. , Jul. 2000, pp. 429–431. DOI: 10.1109/IGARSS.2000.860554.

[5] D. B. Lindell and D. G. Long, "High-resolution soil moisture retrieval with ASCAT," *IEEE Geoscience and Remote Sensing Letters*, vol. 13, no. 7, pp. 972–976, 2016. DOI: 10.1109/lgrs.2016.2557321.

[6] H. Stephen and D. Long, "Surface statistics of Saharan sand dunes derived from scatterometer measurements," in *Proceedings of the International Geoscience and Remote Sensing Symposium*, vol. , Jul. 2003, pp. 1549–1551. DOI: 10.1109/IGARSS.2003.1294171.

[7] National Academies of Sciences, Engineering, and Medicine, *Thriving on our changing planet: A decadal strategy for Earth observation from space*. National Academies Press, 2018.

[8] M. G. Schlax, D. B. Chelton, and M. H. Freilich, "Sampling errors in wind fields constructed from single and tandem scatterometer datasets," *Journal of Atmospheric and Oceanic Technology*, vol. 18, no. 6, pp. 1014–1036, 2001.

[9] G. De Chiarra and P. Laloyaux, "On the impact of scatterometer winds in coupled and uncoupled DAS: Preliminary results," 2017. [Online]. Available: `https://mdc.coaps.fsu.edu/scatterometry/meeting/docs/2017/docs/Thursday/morning/FirstSession/930DeChiara_IOVWST2017_v1.0.pdf` (visited on 12/28/2020).

[10] (2010). NHC issuance criteria changes for tropical cyclone watches/warnings, [Online]. Available: `https://www.nhc.noaa.gov/watchwarn_changes.shtml` (visited on 03/26/2021).

[11] Disaster Technical Assistance Center Supplemental Research Bulletin, "Greater impact: How disasters affect people of low socioeconomic status," U.S. Substance Abuse and Mental Health Services Administration, Jul. 2017.

[12] S. Hallegatte, A. Vogt-Schilb, M. Bangalore, and J. Rozenberg, *Unbreakable: building the resilience of the poor in the face of natural disasters*. World Bank Publications, 2016.

[13] H. Ritchie, "Natural disasters," *Our World in Data*, 2014. [Online]. Available: `https://ourworldindata.org/natural-disasters`.

[14] J. P. Kossin, K. R. Knapp, T. L. Olander, and C. S. Velden, "Global increase in major tropical cyclone exceedance probability over the past four decades," *Proceedings of the National Academy of Sciences*, vol. 117, no. 22, pp. 11 975–11 980, 2020.

[15] A. Smith, N. Lott, T. Houston, K. Shein, J. Crouch, and J. Enloe. (Jul. 2020). US billion-dollar weather & climate disasters 1980-2019, NOAA National Centers for Environmental Information, [Online]. Available: `https://www.ncdc.noaa.gov/billions/events.pdf` (visited on 07/16/2020).

[16] W. Lin and X. Dong, "Design and optimization of a Ku-band rotating, range-gated fan-beam scatterometer," *International Journal of Remote Sensing*, vol. 32, no. 8, pp. 2151–2171, 2011. DOI: `10.1080/01431161003674626`.

[17] W. Tsai, J. Graf, C. Winn, J. Huddleston, S. Dunbar, M. Freilich, F. Wentz, D. Long, and W. Jones, "Postlaunch sensor verification and calibration of the NASA scatterometer," *IEEE Transactions on Geoscience and Remote Sensing*, vol. 37, no. 3, pp. 1517–1542, May 1999. DOI: 10.1109/36.763264.

[18] H. Hersbach, A. Stoffelen, and S. de Haan, "An improved C-band scatterometer ocean geophysical model function: CMOD5," *Journal of Geophysical Research: Oceans*, vol. 112, no. C3, 2007.

[19] H. J. Kramer. (2020). Skylab space station, [Online]. Available: https://directory.eoportal.org/web/eoportal/satellite-missions/s/skylab (visited on 06/19/2020).

[20] ——, (2020). Seasat mission – the world's first satellite mission dedicated to oceanography, [Online]. Available: https://directory.eoportal.org/web/eoportal/satellite-missions/s/seasat (visited on 06/19/2020).

[21] E. P. Attema, "The active microwave instrument on-board the ERS-1 satellite," *Proceedings of the IEEE*, vol. 79, no. 6, pp. 791–799, 1991.

[22] H. J. Kramer. (2020). ERS-1 (European remote-sensing satellite-1), [Online]. Available: https://directory.eoportal.org/web/eoportal/satellite-missions/e/ers-1 (visited on 06/19/2020).

[23] M. Spencer, C. Wu, and D. Long, "Tradeoffs in the design of a spaceborne scanning pencil beam scatterometer: Application to SeaWinds," *IEEE Transactions on Geoscience and Remote Sensing*, vol. 35, no. 1, pp. 115–126, 1997. DOI: 10.1109/36.551940.

[24] J. Figa-Saldaña, J. J. Wilson, E. Attema, R. Gelsthorpe, M. Drinkwater, and A. Stoffelen, "The advanced scatterometer (ASCAT) on the meteorological operational (MetOp) platform: A follow on for European wind scatterometers," *Canadian Journal of Remote Sensing*, vol. 28, no. 3, pp. 404–412, 2002.

[25] C. S. Ruf, C. Chew, T. Lang, M. G. Morris, K. Nave, A. Ridley, and R. Balasubramaniam, "A new paradigm in Earth environmental monitoring with the CYGNSS small satellite constellation," *Nature Scientific Reports*, vol. 8, no. 1, pp. 1–13, 2018.

[26] P. Jales, S. Esterhuizen, D. Masters, V. Nguyen, O. N. Correig, T. Yuasa, and J. Cartwright, "The new Spire GNSS-R satellite missions and products," in *Image and Signal Processing for Remote Sensing XXVI*, International Society for Optics and Photonics, vol. 11533, 2020, p. 1 153 316.

[27] C. A. Mattson and C. D. Sorensen, *Fundamentals of Product Development*. CreateSpace Independent Publishing Platform, 2015.

[28] C. M. Christensen, *The innovator's dilemma: when new technologies cause great firms to fail*. Harvard Business Review Press, 2013.

[29] D. Selva, A. Golkar, O. Korobova, I. L. Cruz, P. Collopy, and O. L. de Weck, "Distributed Earth satellite systems: What is needed to move forward?" *Journal of Aerospace Information Systems*, vol. 14, no. 8, pp. 412–438, 2017.

[30] R. Zimmerman, D. Doan, L. Leung, J. Mason, N. Parsons, and K. Shahid, "Commissioning the world's largest satellite constellation," in *Proceedings of the Small Satellite Conference*, vol. 31, 2017.

[31] M. A. Richards, J. A. Scheer, and W. A. Holm, *Principles of Modern Radar*. Scitech Publishing Inc., 2015.

[32] Radar Systems Panel and IEEE Aerospace and Electronic Systems Society, "IEEE standard for radar definitions," *IEEE Std 686-2017 (Revision of IEEE Std 686-2008)*, pp. 13, 29–29, 2017. DOI: 10.1109/IEEESTD.2017.8048479.

[33] Alliance for Telecommunications Industry Solutions. (2011). ANS telecom glossary, American national standard T1.523-2001, [Online]. Available: http://glossary.atis.org (visited on 07/11/2021).

[34] M. P. Walton and D. G. Long, "Architectures for Earth-observing cubesat scatterometers," vol. 10769, 2018. DOI: 10.1117/12.2321696.

[35] P. Walton and D. Long, "Space of solutions to ocean surface wind measurement using scatterometer constellations," *Journal of Applied Remote Sensing*, vol. 13, no. 3, p. 032 506, 2019, International Society for Optics and Photonics.

[36] P. Walton, D. Long, and C. Carver, "Full-system parametric extrema model for satellite wind scatterometry," in *CubeSats and SmallSats for Remote Sensing IV*, International Society for Optics and Photonics, vol. 11505, 2020, 115050P.

[37] D. G. Long, "Matlab NSCAT1 tabular model function evaluation code," *IEEE Remote Sensing Code Library*, 2018. DOI: 10.21982/M8P35J.

[38] F. T. Ulaby, R. K. Moore, and A. K. Fung, *Microwave Remote Sensing: Active and Passive, Microwave Remote Sensing Fundamentals and Radiometry*. 1981, vol. 1.

[39] M. Spencer, W. Tsai, and D. Long, "High-resolution measurements with a spaceborne pencil-beam scatterometer using combined range/Doppler discrimination techniques," *IEEE Transactions on Geoscience and Remote Sensing*, vol. 41, no. 3, pp. 567–581, 2003. DOI: 10.1109/tgrs.2003.809938.

[40] C. Elachi and J. van Zyl, *Introduction to the Physics and Techniques of Remote Sensing*, 2nd ed. Hoboken, New Jersey: John Wiley & Sons, Inc., 2006.

[41] D. Long, "Comparison of SeaWinds backscatter imaging algorithms," *IEEE Journal of Selected Topics in Applied Earth Observations*, vol. 10, no. 3, pp. 2214–2231, 2017.

[42] E. W. Weisstein. (2020). Spherical segment, Mathworld, A Wolfram Web Resource, [Online]. Available: https://mathworld.wolfram.com/SphericalSegment.html (visited on 06/19/2020).

[43] C. J. E. Keesee, "Spacecraft thermal control systems," *Lecture taught by Col. John E. Keesee, undated; Course 16-851, Satellite Engineering, School of Engineering, Massachusetts Institute of Technology*, 2003.

[44] R. Sumanth, "Computation of eclipse time for low-earth orbiting small satellites," *International Journal of Aviation, Aeronautics, and Aerospace*, vol. 6, no. 5, p. 15, 2019.

[45] S. Czernik, "Design of the thermal control system for compass-1," PhD thesis, Department of Aerospace Engineering, University of Applied Sciences Aachen, Germany, 2008.

[46] C. Mejia, F. Badran, A. Bentamy, M. Crepon, S. Thiria, and N. Tran, "Determination of the geophysical model function of nscat and its corresponding variance by the use of neural networks," *Journal of Geophysical Research: Oceans*, vol. 104, no. C5, pp. 11 539–11 556, 1999. DOI: 10.1029/1998JC900118.

[47] F. J. Wentz and D. K. Smith, "A model function for the ocean-normalized radar cross section at 14 GHz derived from NSCAT observations," *Journal of Geophysical Research: Oceans*, vol. 104, no. C5, pp. 11 499–11 514, 1999. DOI: 10.1029/98JC02148.

[48] J. E. Graf, F. Naderi, and Wu-Yang Tsai, "Overview of NASA scatterometers projects," in *1995 International Geoscience and Remote Sensing Symposium, IGARSS '95. Quantitative Remote Sensing for Science and Applications*, vol. 2, 1995, 1564–1566 vol.2.

[49] J. P. Laboratory. (1997). Missions: NSCAT, [Online]. Available: https://winds.jpl.nasa.gov/missions/nscat/ (visited on 08/20/2020).

[50] J. Figa-Saldaña, J. J. Wilson, E. Attema, R. Gelsthorpe, M. R. Drinkwater, and A. Stoffelen, "The Advanced Scatterometer (ASCAT) on the Meteorological Operational (MetOp) platform: A follow on for European wind scatterometers," *Canadian Journal of Remote Sensing*, vol. 28, no. 3, pp. 404–412, 2002. DOI: 10.5589/m02-035.

[51] T. Lungu and P. Callahan, "QuikSCAT science data product user's manual: Overview and geophysical data products," *D-18053-Rev A, version*, vol. 3, p. 91, 2006.

[52] D. Long, "A QuikSCAT/SeaWinds sigma-0 browse product. version 2.0, Utah. on-line document available," *http://www.scp.byu.edu/docs/pdf/QscatBrowse.pdf*, 2000.

[53] W. Lin, X. Dong, M. Portabella, S. Lang, Y. He, R. Yun, Z. Wang, X. Xu, D. Zhu, and J. Liu, "A perspective on the performance of the CFOSAT rotating fan-beam scatterometer," *IEEE Transactions on Geoscience and Remote Sensing*, vol. 57, no. 2, pp. 627–639, 2019.

[54] Z. Li, A. Stoffelen, and A. Verhoef, "CFOSAT and WindRad rotating fan-beam scatterometer simulation and wind retrieval performance evaluation," 2019.

[55] R. Yun, X. Xu, X. Dong, and D. Zhu, "Simulation and retrieval of wind of CFOSAT rotating-fan beam scatterometer," in *2016 IEEE International Geoscience and Remote Sensing Symposium (IGARSS)*, 2016, pp. 5797–5800.

[56] M. P. Walton, A. Laraway, C. Carver, J. Bartschi, B. Coles, and D. G. Long, "Hourly ocean vector winds measured by a constellation of nanosatellite scatterometers," in *Proceedings of the 101st American Meteorological Society Conference*, (Virtual), Care Weather and Brigham Young University, vol. Joint 1A, Jan. 11, 2021. [Online]. Available: `https://ams.confex.com/ams/101ANNUAL/meetingapp.cgi/Paper/381257` (visited on 07/29/2021).

[57] P. Walton, D. Long, and T. Lang, "Veery, a small scatterometer intended for a constellation capable of global, hourly ocean vector wind measurement," in *Proceedings of the International Ocean Surface Vector Winds Science Team Meeting*, (Virtual), Brigham Young University and NASA Marshall Space Flight Center, Feb. 24, 2021.

[58] R. Fowler, L. Howell, and S. Magleby, "Compliant space mechanisms: A new frontier for compliant mechanisms," *Mech. Sci*, vol. 2, no. 2, pp. 205–215, 2011.

[59] B. DeFigueiredo, S. Magleby, and L. Howell, "Flexible and conformal electronics using rigid substrates," in *U.S. Patent 650453*, Jan. 2018.

[60] S. A. Zirbel, B. P. Trease, M. W. Thomson, R. J. Lang, S. P. Magleby, and L. H. Howell, "Hanaflex: A large solar array for space applications," in *Proceedings of SPIE, Micro- and Nanotechnology Sensors, Systems, and Applications VII*, vol. 9467, 2015, pp. 9467 – 9467–9. DOI: `10.1117/12.2177730`.

[61] C. Boshuizen, J. Mason, P. Klupar, and S. Spanhake, "Results from the Planet Labs flock constellation," in *Proceedings of the Small Satellite Conference*, vol. 28, 2014.

[62] T. R. Lockett, A. Martinez, D. Boyd, M. SanSoucie, B. Farmer, T. Schneider, G. Laue, L. Fabisinski, L. Johnson, and J. A. Carr, "Advancements of the lightweight integrated solar array and transceiver (LISA-T) small spacecraft system," in *IEEE 42nd Photovoltaic Specialist Conference (PVSC)*, IEEE, 2015, pp. 1–6.

[63] D. Steitz, F. O'Donnell, D. Ainsworth, and G. Diller, "QuikSCAT scatterometer press kit," *National Aeronautics and Space Administration*, 1999.

[64] J. A. King, *AMSAT / IARU annotated link model system*, version 2.5.5, Amateur Radio Satellite Corporation. [Online]. Available: `http://www.amsatuk.me.uk/iaru/AMSAT-IARU_Link_Model_Rev2.5.5.xls` (visited on 07/18/2021).

[65] P. Corke, *Robotics, vision and control: fundamental algorithms in MATLAB® second, completely revised*. Springer, 2017, vol. 118.

[66] D. G. Long, C. Y. Chi, and F. Li, "The design of an onboard digital Doppler processor for a spaceborne scatterometer," *IEEE Transactions on Geoscience and Remote Sensing*, vol. 26, no. 6, pp. 869–878, 1988.

[67] J. Graf, C. Sasaki, C. Winn, W. T. Liu, W. Tsai, M. Freilich, and D. Long, "Nasa scatterometer experiment," *Acta Astronautica*, vol. 43, no. 7-8, pp. 397–407, 1998.

[68] C. Reimer, T. Melzer, and W. Wagner, "Long-term soil moisture data records derived from a series of European scatterometers," in *Comprehensive Remote Sensing*, S. Liang, Ed., Oxford: Elsevier, 2018, pp. 51–84, ISBN: 978-0-12-803221-3. DOI: `https://doi.org/10.1016/B978-0-12-409548-9.10354-9`. [Online]. Available: `http://www.sciencedirect.com/science/article/pii/B9780124095489103549`.

[69] A. Elyouncha and X. Neyt, "Comparison of the spatial and radiometric resolution of ERS and Metop C-band radars," vol. 9240, Sep. 2014. DOI: `10.1117/12.2068190`.

[70] M. W. Spencer, C. Wu, and D. G. Long, "Improved resolution backscatter measurements with the SeaWinds pencil-beam scatterometer," *IEEE Transactions on Geoscience and Remote Sensing*, vol. 38, no. 1, pp. 89–104, 2000.

Appendix A

Expanded Equations

Several of the equations in Chapter 5 use functional parameters to simplify derivations. It is easier to program these equations in a spreadsheet if the functional parameters are replaced with the design and intermediate parameters of which they are function. Expanded equations with these substitutions follow.

Substituting Eq. 5.26, Eq. 5.13, and Eq. 5.10, the expanded form of Eq. 5.24 becomes

$$\begin{aligned} a_r(\theta_3) &= \alpha_r(\theta_3) R_E \\ &= \left[\alpha\Big(\phi + \frac{\theta_3}{2}, h\Big) - \alpha\Big(\phi - \frac{\theta_3}{2}, h\Big)\right] R_E \\ &= \left[\theta\Big(\phi + \frac{\theta_3}{2}\Big) - \Big(\phi + \frac{\theta_3}{2}\Big) - \theta\Big(\phi - \frac{\theta_3}{2}\Big) + \Big(\phi - \frac{\theta_3}{2}\Big)\right] R_E \\ &= \left[\theta\Big(\phi + \frac{\theta_3}{2}\Big) - \theta\Big(\phi - \frac{\theta_3}{2}\Big) - \theta_3\right] R_E \\ &= \left[\sin^{-1}\left[\sin\left(\phi + \frac{\theta_3}{2}\right)\frac{R_E + h}{R_E}\right] - \sin^{-1}\left[\sin\left(\phi - \frac{\theta_3}{2}\right)\frac{R_E + h}{R_E}\right] - \theta_3\right] R_E \ , \end{aligned} \tag{A.1}$$

where symbols are given in Section 5.11.

Substituting Eq. 5.13 and Eq. 5.10, the expanded form of Eq. 5.25 becomes

$$\begin{aligned} a_\gamma(\theta_3) &= \alpha_\gamma(\theta_3) R_E \\ &\approx 2\alpha\left(\frac{\theta_3}{2}, R_s\right) R_E \\ &= 2\left(\theta\left(\frac{\theta_3}{2}, R_s\right) - \frac{\theta_3}{2}\right) R_E \\ &= 2\left[\sin^{-1}\left(\sin\left(\frac{\theta_3}{2}\right)\frac{R_E + R_s}{R_E}\right) - \frac{\theta_3}{2}\right] R_E \ , \end{aligned} \tag{A.2}$$

where symbols are given in Section 5.11.

Substituting Eq. 5.10 for θ, the expanded form of Eq. 5.13 becomes

$$\begin{aligned} \alpha &= \theta(\phi, h) - \phi \\ &= \sin^{-1}\left(\sin(\phi)\frac{R_E + h}{R_E}\right) - \phi \ , \end{aligned} \tag{A.3}$$

where symbols are given in Section 5.11.

Appendix B

Taylor Series Approximation of the Maximum Doppler-derived Spatial Resolution

For the equation

$$\frac{y+x}{\sqrt{(y+x)^2+a^2}}\ , \tag{B.1}$$

using Wolfram Alpha Computational Engine, the Taylor series expansion at $x=0$ is

$$\begin{aligned}&\frac{y}{\sqrt{a^2+y^2}}+\frac{a^2x}{(a^2+y^2)^{\frac{3}{2}}}-\frac{3x^2(a^2y)}{2(a^2+y^2)^{\frac{5}{2}}}+\frac{x^3(4a^2y^2-a^4)}{2(a^2+y^2)^{\frac{7}{2}}}\\&+\frac{5a^2x^4y(3a^2-4y^2)}{8(a^2+y^2)^{\frac{9}{2}}}+\frac{3x^5(a^6-12a^4y^2+8a^2y^4)}{8(a^2+y^2)^{\frac{11}{2}}}+O(x^6)...\end{aligned} \tag{B.2}$$

For $y \approx a$, the 2^{nd}-order term becomes

$$\frac{3x^2(a^2y)}{2(a^2+y^2)^{\frac{5}{2}}} \approx \frac{3x^2a^3}{64(a^5)} \approx \frac{x^2}{20a^3}\ , \tag{B.3}$$

which is negligible for $x << a$. Therefore, for $x << y \approx a$, terms on the order of $O(x^2)$ and higher are negligible. Thus for $x << y \approx a$,

$$\frac{y+x}{\sqrt{(y+x)^2+a^2}} \approx \frac{x^2}{20a^3} \ . \tag{B.4}$$

Appendix C

Orbital Average of Illumination Efficiency

The illumination efficiency of the i$^{\text{th}}$ face averaged across satellite rotation and across the course of the orbit is

$$\eta_i = \frac{\int_{-\frac{\pi}{2}}^{\frac{\pi}{2}} \int_{\psi_u^-}^{\psi_u^+} \max\left[0, \left(\underline{\mathrm{R}}_o(\alpha_o, \beta)\underline{\mathrm{R}}_u(\psi_u)\underline{\mathrm{n}}_i\right) \cdot \hat{x}\right] d\psi_u d\alpha_o}{\int_{-\frac{\pi}{2}}^{\frac{\pi}{2}} \int_{\psi_u^-}^{\psi_u^+} d\psi_u d\alpha_o} \ , \tag{C.1}$$

where the bounds of the first integral represent the range of orbit positions in which the satellite is lit for an orbit with half eclipse and half sun, ψ_u is the angle of rotation of the satellite about its axis of rotation, β is the angle between the orbital plane and the sun direction, α_o is the point of the satellite in its orbit, R_o is the rotation matrix of the satellite with respect to the sun due to the orbital position, and R_u is the rotation matrix of the satellite due to its rotation pattern. $\alpha_o = 0$ occurs when the satellite is between the Earth and the sun. The dot product gives the projection of the normal vector of the i$^{\text{th}}$ face, $\underline{\mathrm{n}}_i$, in the direction of the sun, taken to be the $\hat{x}$ direction. The max function accounts for occlusion of back faces when they're turned away from the sun. Unfortunately, no closed-form solution exists for this integral, so Chapter 5 develops an approximate average instead.

The rotation of the satellite due to its orbital position can be expressed as an axis-angle rotation matrix, where the axis is the axis of the orbit. This rotation matrix can be found using Rodrigues' rotation formula, given in Eq. 2.18 of Corke [65] as

$$\underline{\mathrm{R}}_{\alpha}(\alpha_o, \beta) = R_y(\beta)(\underline{\mathrm{I}}_{3x3} + \sin(\alpha_o)[\underline{\mathrm{v}}]_x + (1 - \cos(\alpha_o))[\underline{\mathrm{v}}]_x^2 \ , \tag{C.2}$$

where $R_y\beta$ is the rotation matrix about the y axis, I_{3x3} is the 3x3 identity matrix, $\underline{\mathrm{v}}$ is the vector about which the satellite orbits, and $[\underline{\mathrm{x}}]_x$ is skew symmetric matrix notation.

The vector about which the satellite orbits is

$$\underline{\mathrm{v}} = \underline{\mathrm{R}}_y(\beta)\hat{z} = [\sin(\beta) \quad 0 \quad \cos(\beta)]^T \ . \tag{C.3}$$

Appendix D

Values Used in Parametric Full-system Modeling

D.1 Design Parameters Used in Model Validation

Heritage point designs were used to validate the parametric extrema model for satellite wind scatterometry. Chapter 6 describes this approach. Table 6.1 compares performance estimates for these designs obtained using the model of Chapter 5 to those obtained from the literature. Tables D.1-D.4 detail the input values used to develop the performance estimates given in Table 6.1. The design parameters listed in this appendix are introduced in Chapter 5 and summarized in Table 5.5.

D.2 Design Parameters Used for the New Scatterometer Concepts

In Chapter 7, two designs for constellations of cooperative scatterometers were presented. Table 7.1 presents their initial performance estimates. Table D.5 gives the design parameters used with the model to obtain these performance estimates. Key elements of the reasoning behind these design parameters are given in the narrative of Chapter 7.

Table D.1: NSCAT Design Parameters

Parameter	**Value**
Transmit Power	110 W [48]
Frequency	14.0 GHz [48]
Doppler Compensation	Cell [66]
Polarization	H/V [48]
Receive Bandwidth	40.0 kHz to 10.0 kHz
Dwell Time	405 ms
Pulse Compression Mode	LFM [66]
Pulse Length	5.0 ms [2]
Pulse Repetition Interval	16.1 ms [2]
Burst Pulse Count	1 [2]
Burst Repetition Interval	16.1 ms [2]
Resolution Mode	Doppler [67]
Coherent Integration	FALSE [2]
Number of RF Chains	8
Noise Factor	2.1 dB
Transmit Loss	3. dB
Receive Loss	3. dB
Signal Processing Loss	.5 dB
Atmospheric Loss	.5 dB
Doppler Binning	1X to 4000X
Spatial Downsampling Factor	(4X, 1X)
Supplementary Frontends	4 [48]
Complementary Frontends	2 [48]
Half-duplex Frontends	1 [48]
Full-duplex Frontends	1 [48]
First Antenna Length	8.1 cm

Table D.1 NSCAT Design Parameters – (continued)

Parameter	**Value**
Second Antenna Length	3.1 m [67]
Transmit Antenna Efficiency	75% [48]
Receive Antenna Efficiency	75% [48]
First Beamwidth Factor	1.58 [67]
Second Beamwidth Factor	1.19 [67]
Transmit Aperture Efficiency	0.71 to 0.90 [67]
Receive Aperture Efficiency	0.71 to 0.90 [67]
Antenna Shape Factor	1
Elevation Look Angle	30° to 35° [47]
Azimuth Look Angle	25° to 45° [67]
Scan Rate	0 [67]
Dedicated Charging Consecutivity	0
Dedicated Charging Consecutivity	100%
Scatterometer Operational Duty Cycle	100%
Focus Factor	100%
Precession	FALSE
Supplementary Satellites	1 [67]
Complementary Satellites	1 [67]
Half-duplex Satellites	1 [67]
Full-duplex Satellites	1 [67]
Number of Orbital Planes	1 [67]
Orbit Altitude	797 km [48]
Orbit Inclination	98.6° [48]

Table D.2: ASCAT Design Parameters

Parameter	**Value**
Transmit Power	120 W [68]
Frequency	5.255 GHz [68]
Doppler Compensation	TRUE [68]
Polarization	VV [68]
Receive Bandwidth	228.3 kHz to 456.6 kHz [69]
Dwell Time	424 ms
Pulse Compression Mode	LFM [69]
Pulse Length	8.5 ms to 10.8 ms [69]
Pulse Repetition Interval	35.4 ms [69]
Burst Pulse Count	8
Burst Repetition Interval	180 ms to 228 ms [69]
Resolution Mode	Range/Doppler [68]
Coherent Integration	FALSE
Number of RF Chains	6
Noise Factor	2.1 dB
Transmit Loss	.4 dB to .8 dB
Receive Loss	.4 dB to .8 dB
Signal Processing Loss	.1 dB to .5 dB
Atmospheric Loss	.5 dB
Doppler Binning	1X
Spatial Downsampling Factor	(46.6X, 3.77X)
Supplementary Frontends	3 [68]
Complementary Frontends	2 [68]
Half-duplex Frontends	1 [68]
Full-duplex Frontends	1 [68]
First Antenna Length	0.25 m x 3 m [69]

Table D.2 ASCAT Design Parameters – (continued)

Parameter	**Value**
Second Antenna Length	0.34 m x 2.25 m [69]
Transmit Antenna Efficiency	90%
Receive Antenna Efficiency	90%
First Beamwidth Factor	0.44 to 0.94 [68]
Second Beamwidth Factor	0.44 to 0.94 [68]
Transmit Aperture Efficiency	1
Receive Aperture Efficiency	1
Antenna Shape Factor	1
Elevation Look Angle	26° to 49° [68]
Azimuth Look Angle	0° to 45° [68]
Scan Rate	0 [68]
Dedicated Charging Duty Cycle	0
Dedicated Charging Consecutivity	1
Scatterometer Operational Duty Cycle	100%
Focus Factor	100%
Precession	FALSE
Supplementary Satellites	1 [68]
Complementary Satellites	1 [68]
Half-duplex Satellites	1 [68]
Full-duplex Satellites	1 [68]
Number of Orbital Planes	3 [68]
Orbit Altitude	820 km [68]
Orbit Inclination	98.7° [68]

Table D.3: QuikSCAT Design Parameters

Parameter	**Value**
Transmit Power	110 W [70]
Frequency	13.402 GHz [70]
Doppler Compensation	TRUE
Polarization	H/V [70]
Receive Bandwidth	40.0 kHz [70]
Dwell Time	10.7 ms [70]
Pulse Compression Mode	LFM [70]
Pulse Length	1.5 ms [70]
Pulse Repetition Interval	5.4 ms [70]
Burst Pulse Count	1 [70]
Burst Repetition Interval	5.4 ms [70]
Resolution Mode	Range/Doppler [70]
Coherent Integration	FALSE
Number of RF Chains	2 [70]
Noise Factor	2.1 dB
Transmit Loss	.4 dB to .8 dB
Receive Loss	.4 dB to .8 dB
Signal Processing Loss	.1 dB to .5 dB
Atmospheric Loss	.5 dB
Doppler Binning	1X
Spatial Downsampling Factor	(59X, 28.5X)
Supplementary Frontends	1 to 2
Complementary Frontends	1
Half-duplex Frontends	1
Full-duplex Frontends	1
First Antenna Length	90.0 cm

Table D.3 QuikSCAT Design Parameters – (continued)

Parameter	**Value**
Second Antenna Length	90.0 cm
Transmit Antenna Efficiency	70%
Receive Antenna Efficiency	70%
First Beamwidth Factor	1.11 to 1.28
Second Beamwidth Factor	0.97 to 1.21
Transmit Aperture Efficiency	0.76 to 0.90
Receive Aperture Efficiency	0.76 to 0.90
Antenna Shape Factor	0.79
Elevation Look Angle	40° to 46°
Azimuth Look Angle	0
Scan Rate	18 rpm
Dedicated Charging Duty Cycle	0
Dedicated Charging Consecutivity	1
Scatterometer Operational Duty Cycle	100%
Focus Factor	100%
Precession	FALSE
Supplementary Satellites	1
Complementary Satellites	1
Half-duplex Satellites	1
Full-duplex Satellites	1
Number of Orbital Planes	1
Orbit Altitude	803 km
Orbit Inclination	99°

Table D.4: RFSCAT Design Parameters

Parameter	**Value**
Transmit Power	120 W
Frequency	13.3 GHz
Doppler Compensation	Cell
Polarization	H/V
Receive Bandwidth	100.0 kHz
Dwell Time	25.0 ms
Pulse Compression Mode	LFM
Pulse Length	1.4 ms
Pulse Repetition Interval	6.8 ms
Burst Pulse Count	1
Burst Repetition Interval	6.8 ms
Resolution Mode	Range/Doppler
Coherent Integration	FALSE
Number of RF Chains	1
Noise Factor	3. dB
Transmit Loss	3. dB
Recieve Loss	3. dB
Signal Processing Loss	.5 dB
Atmospheric Loss	.5 dB
Doppler Binning	1X
Spatial Downsampling Factor	(120X, 90X)
Supplementary Frontends	1
Complementary Frontends	2
Half-duplex Frontends	1
Full-duplex Frontends	1
First Antenna Length	40.0 cm

Table D.4 RFSCAT Design Parameters – (continued)

Parameter	**Value**
Second Antenna Length	1.2 m
Transmit Antenna Efficiency	90%
Receive Antenna Efficiency	90%
First Beamwidth Factor	0.73
Second Beamwidth Factor	0.88
Transmit Aperture Efficiency	1
Receive Aperture Efficiency	1
Antenna Shape Factor	1
Elevation Look Angle	25° to 46°
Azimuth Look Angle	0
Scan Rate	20 deg/s
Dedicated Charging Duty Cycle	0.0%
Dedicated Charging Consecutivity	100%
Scatterometer Operational Duty Cycle	100%
Focus Factor	100%
Precession	FALSE
Supplementary Satellites	1
Complementary Satellites	1
Half-duplex Satellites	1
Full-duplex Satellites	1
Number of Orbital Planes	1
Orbit Altitude	519 km
Orbit Inclination	97°

Table D.5: New Concepts Design Parameters

Parameter	**Value** Half-duplex | Full-duplex
Transmit Power	30 W
Frequency	14 GHz (1 Mhz Tx Bandwidth)
Doppler Compensation	Cell
Polarization	H/V
Receive Bandwidth	1.1 MHz
Dwell Time	405 ms
Pulse Compression Mode	LFM
Pulse Length	2.7 ms
Pulse Repetition Interval	4.8 ms
Burst Pulse Count	1
Burst Repetition Interval	4.8 ms
Resolution Mode	Doppler
Coherent Integration	FALSE
Number of RF Chains	1
Noise Factor	2.1 dB
Transmit Loss	(0.4, 0.8) dB
Recieve Loss	(0.4, 0.8) dB
Signal Processing Loss	(0.1, 0.5) dB
Atmospheric Loss	.5 dB
Doppler Binning	(1X, 10,000X)
Spatial Downsampling Factor	(16.3X, 1.41X) | (21.7X, 1.89X)
Supplementary Frontends	1
Complementary Frontends	1
Half-duplex Frontends	1
Full-duplex Frontends	1

Table D.5 New Concepts Design Parameters – (continued)

Parameter	**Value** Half-duplex | Full-duplex
First Antenna Length	2.0 cm
Second Antenna Length	1 m | 2 m
Transmit Antenna Efficiency	90%
Receive Antenna Efficiency	90%
First Beamwidth Factor	0.88
Second Beamwidth Factor	0.88
Transmit Aperture Efficiency	1
Receive Aperture Efficiency	1
Antenna Shape Factor	1
Elevation Look Angle	36°
Azimuth Look Angle	45°
Scan Rate	0 deg/s
Dedicated Charging Duty Cycle	(15%, 35%)
Dedicated Charging Consecutivity	100%
Scatterometer Operational Duty Cycle	66%
Focus Factor	100%
Precession	FALSE
Supplementary Satellites	1
Complementary Satellites	1
Simplex Satellites	3 | 1
Half-duplex Satellites	1
Full-duplex Satellites	1 | 3
Number of Orbital Planes	(8, 200)
Orbit Altitude	400 km
Orbit Inclination	96°
Solar Cell Efficiency	28%

Table D.5 New Concepts Design Parameters – (continued)

Parameter	**Value** Half-duplex | Full-duplex
DC-DC Converter Efficiency	(0.90, 0.95)
Scatterometer Amplifier Efficiency	(0.30, 0.58)
Radio Max Power	2.0 W
Computer Max Power	(2.0 W, 3.0 W)
Magnetorquer Max Power	(1.0 W, 2.0 W)
Star Tracker Max Power	(500.0 mW, 1.3 W)
Heater Max Power	4.0 W
Computer Duty Cycle	100%
Magnetorquer Duty Cycle	(10.0%, 20%)
Star Tracker Duty Cycle	100%
Heater Duty Cycle	10.0%
Beacon Size	1.0 kB
Telemetry Sampling Period	5 mins s
Beacon Repeat Period	60.0 s
Ground Station Session Duration	(5 mins s, 10 mins s)
Ground Station Quantity	11
Measurement and Calibration Data Size	32.0 B
Transmitter Speed	400.0 kbps
Transmitter Bandwidth	250.0 kHz
Data Storage Capacity	16.0 GB
Battery Capacity	50.0 A $\cdot$ hr
Battery Average Voltage	4.0 V
Battery Load Factor	(2.0, 3.0)
Satellite Size	2U
Silk Screen Emissivity	0.8
Solar Cell Emissivity	(0.85, 0.87)

Table D.5 New Concepts Design Parameters – (continued)

Parameter	**Value** Half-duplex | Full-duplex
Silk Screen Absorptivity	0.4
Solar Cell Absorptivity	(0.88, 0.92)
X+ Face Solar Cell Coverage	90%
X+ Face Area	0.4 m^2
Y+ Face Solar Cell Coverage	90%
Y+ Face Area	100.0 cm^2
Z+ Face Solar Cell Coverage	90%
Z+ Face Area	300.0 cm^2
X- Face Solar Cell Coverage	90%
X- Face Area	300.0 cm^2
Y- Face Solar Cell Coverage	90%
Y- Face Area	100.0 cm^2
Z- Face Solar Cell Coverage	90%
Z- Face Area	300.0 cm^2
Dedicated Solar Power Generation Area	0.4 m^2
X-axis Satellite Rotation	11°
Y-axis Satellite Rotation	36°
Z-axis Satellite Rotation	11°